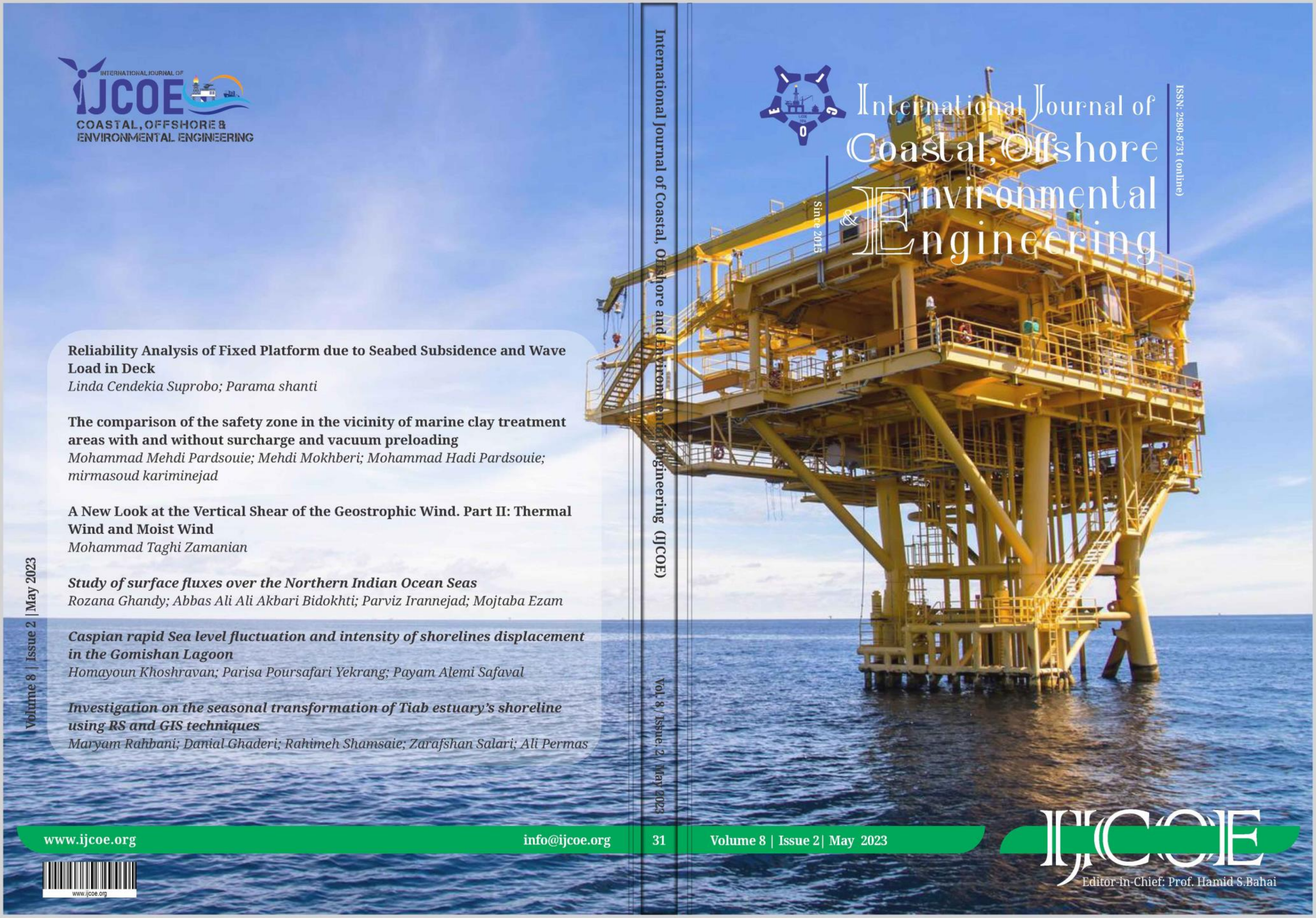

INTERNATIONAL JOURNAL OF
IJCOE
COASTAL, OFFSHORE &
ENVIRONMENTAL ENGINEERING

Volume 8 | Issue 2 |May 2023

www.ijcoe.org
info@ijcoe.org

www.ijcoe.org

International Journal of Coastal, Offshore and Environmental Engineering (IJCOE)

Vol. 8 / Issue. 2/ May 2023
31

International Journal of Coastal, Offshore & Environmental Engineering

Since 2015
ISSN: 2980-8731 (online)

Volume 8 | Issue 2| May 2023

IJCOE

Editor-in-Chief: Prof. Hamid S.Bahai

International Journal of
Coastal, Offshore
& Environmental
Engineering
Since 2015
ISSN: 2980-8731 (online)

In The Name of God

Message from the Editor-in-Chief

The IJCOE journal office was established in 2015,and its first issue was published in 2016. TheIJCOE covers a wide range of research in thefields of oceanography & ocean technology, aswell as marine industries & marine engineering.The editorial board of IJCOE consists of nearly130 of the greatest scientists and researchersfrom over 30 countries worldwide, and thejournal's review board comprises 1,000 membersfrom all five continents. The membership andapplication process for joining the editorial andreview boards of this journal is ongoing. IJCOE isa research-academic quarterly journal that haspublication and distribution permissions fromthe Press Organization and permission topublish scientific-research articles from theMinistry of Science, Research, and Technology(MSRT) with an "A" rating. It also holds a "Q1"rating from the ISC institute with an impactfactor (IF) of approximately 0.43 and isconsidered a "core journal" (prestigious andoutstanding journal). IJCOE is an open-accessjournal and allows the download and receipt ofaccepted articles in full text for free. It respectsand adheres to copyright and COPE regulations.The journal's office operates 24/7, providingservices to researchers. In addition to publishinga regular quarterly journal, IJCOE has 16 specialissues on specific topics in preparation. It alsoprovides conditions for publishing specializedbooks, references, and handbooks. Moreover, itis ready to cooperate with the secretariats ofreputable international conferences to publishtheir selected and outstanding articles. IJCOEevaluates, appraises, and publishes books,articles, and the scientific achievements andfindings of esteemed researchers and scientistsworldwide who are innovating and conductingin-depth research in the "important and strategicfield of the maritime technology & Oceanengineering." It welcomes any form of jointcooperation with universities, research institutes,and related research centers at the national,regional, and international levels, and extends ahand for collaboration.

Classification of Editorial Board in IJCOE

- Editor-in-Chief
- Director-in-Chief
- Deputy Editor
- Executive Managers
- English Text Editor
- Technical Editor
- International Editorial Board
- National Editorial Board
- Editorial Board Associate
- Editorial Board Assistant
- Guest Editorial Board
- Advisory Board
- Administrative Coordinator
- Honorary Board Member
- Methodology Advisor

Author Benefits

- Open Access
- Rapid Publication
- Thorough Peer-Review
- No Copyright Constraints
- Coverage by Leading Indexing Services
- Discounts On Article Processing Charges (APC)
- No Space Constraints, No restriction on the maximum length of the papers, number of figures or colors

INTERNATIONAL JOURNAL OF
IJCOE
COASTAL, OFFSHORE &
ENVIRONMENTAL ENGINEERING

Aims of IJCOE

Hydrodynamics

Marine equipment

Structural mechanics

Ocean environmental predictions

Stochastic calculations Experimental

Automatic Control of Marine Systems

Scope of IJCOE

Marine Hazards

Ocean Acoustics

Naval Architecture

Ocean Engineering

Coastal Engineering

Marine Meteorology

Marine Earth Sciences

Underwater Technology

Marine Renewable Energy

Polar & Arctic Engineering

Marine Renewable Energy

Marine Geography & Geodesy

Marine Environmental Engineering

Automatic Control of Marine Systems

Hydro Physics & Physical Oceanography

Type of papers

- Case Studies
- Book Reviews
- Review Article
- Letters to the Editor
- Methodology Papers
- Editorials and Commentaries
- Response or Rejoinder Papers
- Perspective or Opinion Papers
- Conceptual or Theoretical Papers
- Meta-Analysis and Systematic Reviews
- Short Communications or Brief Reports
- Research Articles (Original Research Papers)

Scientific Research Journal

Ministry of Science, Research And Technology (MSRT)

Jurnal Ranking 2023: A

Ministry Of Science, Research And Technology (ISC)

Citation Impact 2022: 0.429

Quartile 2022 : Q1

Core Collection

INTERNATIONAL JOURNAL OF IJCOE COASTAL, OFFSHORE & ENVIRONMENTAL ENGINEERING

IJCOE is a Member of

We Respect the Science CIVILICA
Google Scholar
Jouroscope
COPE 20TH ANNIVERSARY 1997-2017 CC BY NC SA
ISC
JREF.IR Journals Reference
DOAJ DIRECTORY OF OPEN ACCESS JOURNALS
ISSN INTERNATIONAL STANDARD SERIAL NUMBER INTERNATIONAL CENTRE
Researcher.Life
doi Crossref mEDRA
iThenticate
magiran
OPEN ACCESS
pistotn
ResearchGate
Regional Information Center for Science and Technology RICEST
ScienceGate
Scilit
SID
website.informer.com
WEBrate

Cantact Us

Office 1 | Research Institute of Meteorology and Atmospheric Science
Address | Tehran, Shahid Kharrazi Highway, Pajoohesh Blvd, Research Institute of Meteorology and Atmospheric Science, Sand and Dust Storm International Research Center (SDS-IRC), No. 13, 1st floor.
Phone | +982144787652
Postal code | 13611-14977
website | www.rimac.ac.ir

Office 2 | Iranian National Institute for Oceanography and Atmospheric Science
Address | Tehran, Dr. Fatemi Gharbi St., Shahid Etemadzade St., No. 3, third floor.
Phone | +982166944873
Postal code | 13389 – 14118
website | www.inio.ac.ir

Email | Info@ijcoe.org
Website | www.ijcoe.org

Follow Us

www.ijcoe.org

INTERNATIONAL JOURNAL OF
IJCOE
COASTAL, OFFSHORE & ENVIRONMENTAL ENGINEERING

Volume & Issue:

Volume 8, Issue 2, May 2023

Number of Articles: 6

Content

INTERNATIONAL JOURNAL OF
COASTAL, OFFSHORE & ENVIRONMENTAL ENGINEERING
IJCOE Vol.8/No. 2/Spring 2023 (1-12)

Available online at: www. Ijcoe.org

Reliability Analysis of Fixed Platform due to Seabed Subsidence and Wave Load in Deck

Linda Cendekia Suprobo[1], **Parama shanti**[2*]

[1]*MSc Student, Department of Ocean Engineering, Bandung Institute of Technology, Indonesia;*
[2*]*Assistant Professor, Department of Ocean Engineering, Bandung Institute of Technology, Indonesia; parama@office.itb.ac.id*

ARTICLE INFO

Article History:
Received: 16 Jan. 2023
Accepted: 01 Mar. 2023

Keywords:
Fixed Platform
Probability of Failure
Reliability Index
Reserve Strengh Ratio
Wave in Deck

ABSTRACT

The structural integrity of fixed platform may be affected from excessive load on the structure and insufficient strength of the structure. Another factor which affects the structural integrity is seabed subsidence. Seabed subsidence occurs due to vertical movement of soil layers and soil consolidation. The impact of seabed subsidence will lead to decreased of deck clearance or air gap and cause wave hits the deck. The aim of the study is to determine the effect of wave load in deck using pushover and reliability analysis. The wave height at collapse is calculated based on the reserve strength ratio generated from pushover analysis. The wave load in deck calculation is referred to American Petroleum Institute (API). The pushover with inclusion wave load in deck is necessary to be carried out to gain the updated reserve strength ratio. The reliability analysis is computed by involving base shear of fixed platform at collapse from pushover analysis with wave load in deck. Monte Carlo simulation technique method is adopted in the analysis which generating one million data of wave height and wave period as random variables. This study also performs the probability of failure and reliability index due to wave load in deck. As expected, the updated reserve strength ratio with wave load in deck is lower than the reserve strength ratio without wave load in deck. Then, the probability of failure increases with the increase of the depth of subsidence. Therefore, the reliability index decreases with the increase of the depth of subsidence.

1.Introduction

Fixed platform is an offshore structure that is widely applied in Indonesian waters. In the design process of fixed platform structure, it is necessary to ensure the structural integrity to avoid structural failure [1]. Some factors that may affect the structural integrity of fixed platform. They are excessive load on the structure and insufficient structural strength in receiving loads [2]. Excessive load comes from environmental and accidental loads. While insufficient structural strength is happened due to design, fabrication and installation error.

As time passed, fixed platform experienced structural strength may decrease which caused by some factors such as corrosion, weld crack, scour and seabed subsidence [3], [4]. This research focuses on fixed platform that is degraded due to seabed subsidence. Seabed subsidence may occur due to vertical movement of sedimentary layers and sediment consolidation. In addition, massive exploration of petroleum and natural gas can lead to depletion of reservoirs which causing the soil compaction. The soil compaction will increase with the increase of reservoir depletion. Hence, these things lead to seabed subsidence from time to time [5].

Generally, seabed subsidence may affect the decreasing of air gap and getting worse during the extreme conditions. Seabed subsidence needs to be considered during the design process of fixed platform to avoid catastrophic incidents due to conditions where the mean sea level (MSL) becomes closer to the deck. Therefore, there is wave load scenario in deck [6].

Jafari et al. [7] studied the static and dynamic analysis due to wave in deck which considered the effect of regular and irregular wave. The study concluded that the dynamic amplification factor (DAF) tends to decrease as the significant wave crest height increase. Based on this study, the structural integrity and reliability were not the focus in the analysis.

Study performed by Nazokkar et al. [8] conducted the effect of damper on controlling the vibrations of the floating offshore under different loads with wind and wave. The wave load was calculated using modified Morison formulation with the parameter of 100-year significant wave height (H_s) and peak period (T_p). The study assumed that the wave load acted together with the wind load. However, the study did not consider the wave load in deck.

The effect of wave in deck issue on the fixed platform was performed by Yee et al. [9] using pushover analysis. The study concluded that the reserve strength ratio (RSR) and base shear were affected by some contributing factors from wave in deck. They were wave height, wave period and water depth. The wind load in deck was also considered in the pushover analysis. On top of that, the wind load was also found on contributing to the wave load in deck event. None of explanation regarding the reliability analysis of fixed platform due to wave in deck event was included in this study.

Based on the study performed by Azman et al. [10], wave load in deck was considered if the wave crest height at collapse is higher than the bottom steel elevation of the fixed platform. The study considered wave crest height at collapse by incorporating wave load in deck and investigated the impact of wave load in deck for fixed platform. The pushover analysis was utilized to determine the structural integrity of the structure. Then, the reliability-based design and assessment (RBDA) was adopted to determine the probability of failure of the structure. However, the reliability index calculation was excluded in the study.

Pushover and reliability analysis due to seabed subsidence need to be performed to determine the feasibility of structure during operation. Pushover analysis is carried out to determine the behaviour of structural collapse and reserve strength ratio (RSR). This analysis will consider the 100-year environmental load on extreme conditions. In this research, wave load in deck will be considered in pushover analysis if the wave crest height at collapse is higher than bottom of steel elevation of the lowest deck structure.

Then, reliability analysis is performed to calculate the probability of failure (P_f) and reliability index (β). Monte Carlo simulation technique method is adopted in the reliability analysis of fixed platform. In the reliability analysis, it is necessary to determine performance function / limit state to describe random variable. Environmental load on the structure is limited to wave load only which wave height and wave period are considered as random variables. These random variables have one million data that is generated by Matlab software respectively. From the calculation of the probability of failure (P_f) and reliability index (β) of fixed platform, then it can be used as a determination of the feasibility of the structure due to seabed subsidence and wave load in deck during operation.

2.Wave Load in Deck and Reserve Strength Ratio

According to the literature review, there are three methods to calculate wave load in deck. They are silhouette metthod, component method and computational fluid dynamics (CFD) method. Silhouette method is a simple method which based on projected area of wave in deck and does not require the detailed deck model. This method is referred to American Petroleum Institute Recommended Practice – Working Stress Design (API RP-2A WSD) [11]. In the other hand, component method needs detailed deck model to calculate wave load in deck [12],[13]. Then, CFD method simulates the fluid flows of wave load in deck by numerical analysis and compare the results with the laboratory experiment [14],[15].

In this study, the silhouette method is adopted to calculate wave load in deck without considering dynamic effect in the structure. Wave load in deck (F_{Deck}) is determined by formulation from API RP-2A WSD that be written in Eq. (1).

$$F_{Deck} = \frac{1}{2}\rho C_D(\alpha_{wk}V + \alpha_{cb}U)^2 A_{deck} \qquad (1)$$

Where F_{Deck} is wave load in deck, ρ is density of seawater, C_D is drag coefficient, α_{wk} is wave kinematic factor (0.88 for hurricane condition and 1.0 for winter storm condition), α_{cb} is current blockage factor, V is fluid horizontal velocity, U is current velocity in line with wave and A_{deck} is projected area of wave in deck.

According to API RP-2A WSD [11], projected area of wave load in deck (A_{deck}) is calculated from bottom steel of lowest deck elevation (EL_{LD}) up to collapse wave crest elevation (EL_{WID}). Projected area of wave in deck (A_{deck}) is determined with formulation in Eq. (2) [11].

$$A_{deck} = A_{deckx}\cos\theta_w + A_{decky}\sin\theta_w \qquad (2)$$

Where A_{deckx} is projected area of wave in deck in X-axis direction, A_{decky} is projected area of wave in deck in Y-axis direction and θ_w is wave direction.

Wave load in deck occurs when waves strike a platform's deck and equipment because there is no deck clearance or air gap. To avoid wave in deck, the bottom steel of the lowest deck elevation should be located at an elevation which will clear the calculated design wave crest with adequate allowance for safety. Hence, the lowest deck elevation should be designed in higher elevation [11],[16]. In order to calculate the effects of wave load in deck, the maximum wave height of fixed platform at collapse ($H_{Collapse}$) is determined using equation referred to Azman et al. [10] which is shown in Eq. (3).

$$H_{Collapse} = RSR^{\frac{1}{\alpha}}.H_{100} \qquad (3)$$

Where $H_{Collapse}$ is maximum wave height of fixed platform at collapse, H_{100} is 100-year maximum wave height and α is the metaocean constant, typically 1.7 to 2.0. The $H_{Collapse}$ is used to calculate projected area of wave in deck. Then, the wave load in deck is considered in pushover analysis.

In pushover analysis, the structure is subjected to permanent load and functional load first, then followed by environmental load that want to be obtained at ultimate resistance / capacity. The environmental load is incremented until the structure is globally collapsed and generate the ultimate capacity of the structure. Thus, the determination of the ultimate capacity of the structure against load scenario is obtained. This determination system is referred to reserve strength ratio (RSR). Reserve strength ratio is defined as ratio between collapse load of fixed platform and 100-year environmental load of fixed platform, in terms of base shear [2],[17]. Therefore, the formulation of reserve strength ratio is shown in Eq. (4).

$$RSR = \frac{E_{collapse}}{E_{100}} \tag{4}$$

Where RSR is reserve strength ratio, $E_{collapse}$ is base shear of fixed platform at collapse and E_{100} is base shear of 100-year environmetal load.

3.Performance Function, Probability of Failure and Reliability Index

In reliability analysis, it is necessary to determine performance function / limit state [18]. Generally, the performance function can be written in Eq. (5).

$$Z = R - S \tag{5}$$

Where Z is performance function / limit state, which is stochastic variable, R is resistance / capacity of the structure and S is load on the structure. The failure is defined through the performance function which is negative or zero at failure [19].

In this research, R is variable describing the ultimate resistance / capacity of the structure which obtained from base shear of fixed platform at collapse ($E_{collapse}$). Meanwhile, S is variable describing the base shear of structure (E_i) in terms of random wave height (H_i) and wave period (T_i) where these random variables are generated by Matlab software. Therefore, the performance function is given in Eq. (6).

$$Z = E_{collapse} - E_i \tag{6}$$

The regression analysis is employed for formulating base shear structure (E_i). Thus, the general formulation of performance function from regression analysis is given by Eq. (7).

$$Z = E_{collapse} - (AH_i^2 + BT_i^2 + CH_i + DT_i + E) \tag{7}$$

Where A and C are coefficient of random wave height, B and D are coefficient of random wave period and E is constant. The failure occurs when base shear of fixed platform at collapse ($E_{collapse}$) is smaller than base shear of structure (E_i) in terms of random wave height (H_i) and wave period (T_i) as random variables.

The probability of failure (P_f) is computed using Monte Carlo simulation technique. According to Taheri et al. [20], this method requires thousands, millions or even more to obtain the better result. Then the probability of failure (P_f) is given in Eq. (8).

$$P_f = P\ (failure) = P\ (Z < 0) = P(R < S) \tag{8}$$

The formulation above Eq. (8) can be spelled out in the form of derivation from Eq. (7) that given by Eq. (9).

$$P_f = P\left(E_{collapse} < AH_i^2 + BT_i^2 + CH_i + DT_i + E\right) \tag{9}$$

Thus, the reliability index is obtained by Eq. (10).

$$\beta = \Phi^{-1}(1 - P_f) \tag{10}$$

Where Φ^{-1} is standard normal variate at the probability level $(1 - P_f)$.

4.Model Description

The fixed platform that be investigated in this study is 8-leg jacket type processing platform. The water depth of this fixed platform is 33.83 m. The design of this fixed platform is equipped with the facility of living quarter. The general outline of the fixed platform is shown in Figure 1. Then the overview of fixed platform specification is summarized in Table 1.

The selected fixed platform is verified against the latest basis design report, weight control report, inspection report and drawings to represent the actual condition during analysis.

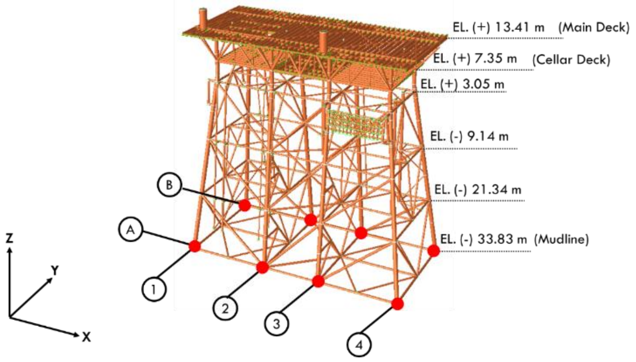

Figure 1. Structure specifications of Fixed Platform

Table 1. Fixed platform specification

Features	Description
Field Location	Java Sea (Indonesia)
Design Service Category	Processing
Design Safety Category	Manned
Installed	2004
Water Depth	33.83 m

Number of Leg	8
Number of Pile	8
Number of Riser	5
Number of Boatlanding	1

5. Research Methodology

The research methodology that be employed in this study and presented here is breaking down into the following eight steps.

i. Identification and Modelling of Fixed Platform
The latest data of fixed platform report and drawings are collected. Latest metaocean data of 100-year maximum wave height (H_{100}), associated wave period (T_{100}) and current velocity are utilized in pushover analysis. In this fixed platform, research is carried out on seabed subsidence with depth of 0 until 7 m.

ii. Pushover Analysis with Depth Variations of Seabed Subsidence
The pushover analysis is performed using SACS software by incrementing the 100-year environmental loads until the fixed platform is globally collapsed. This analysis considers the dead load, live load, and 100-year environmental load in eight directions, which are 0°, 65°, 90°, 115°, 180°, 245°, 270° and 295°. The base shear of fixed platform at collapse is obtained from this analysis. Then the reserve strength ratio can be determined based on the base shear of fixed platform at collapse ($E_{collapse}$) divided by base shear of 100-year environmental load (E_{100}) referred to Eq. (4).

iii. Air Gap Analysis
The maximum wave height of fixed platform at collapse ($H_{Collapse}$) is calculated using Eq. (3) where the reserve strength ratio is acquired in step ii. Then the maximum wave crest height of fixed platform at collapse is compared against the bottom of steel elevation of the lowest deck structure (LD_{EL}).

iv. Pushover Analysis with Depth Variations of Seabed Subsidence and Wave Load in Deck
The pushover analysis is performed again in this step if the maximum wave crest height of fixed platform at collapse is higher than bottom of steel elevation of the lowest deck structure (LD_{EL}). Next, the distance between maximum wave crest height which hitting the deck and bottom of steel elavation of the lowest deck structure (LD_{EL}) is utilized to calculate projected area of wave in deck (A_{deck}) as determined in Eq. (2). Therefore, wave load in deck for fixed platform can be calculated as per Eq. (1). In this pushover analysis, the updated base shear of fixed platform at collapse ($E_{collapse}$) and reserve strength ratio are obtained by incorporating wave load in deck.

v. Kolmogorov-Smirnov Test
The wave data which consist of wave height and wave period are taken from ERA5. Kolmogorov-Smirnov test is carried out to determine which the theoritical distributions can be accepted. Those theoritical distributions are normal, lognormal, Rayleigh and gumbel. From this test, the parameter of mean and standard deviation of accepted theoritical distributions is calculated.

vi. Generation of Random Variables
The generation of random variables which consists of wave height (H_i) and wave period (T_i) is performed using Matlab software. The parameter of mean and standard deviation is required to perform this generation. One million data of wave height (H_i) and wave period (T_i) are generated respectively by this process from Matlab software.

vii. Regression Analysis
The regression analysis is acquired to detemine the relationship between base shear of the structure (E_i) with wave height (H_i) and wave period (T_i). Then, the base shear of the structure (E_i) is defined as load on the structure variable in the performance function.

viii. Reliability Analysis
The performance function is determined by Eq. (7). From this performance function, the probability of failure (P_f) is calculated using Monte Carlo simulation technique method which is stated in Eq. (9). It can be simplified to the number of simulation cycles when Z is zero or negative divided by total number of simulation cycles. Then the reliability index (β) is computed using Eq. (10).
Next, the calculated reliability index (β) is compared with recommended target safety level which referred to Bai [21]. This recommended target safety level is shown in Table 2. The safety class is divided into three level which are low, normal, and high.

- Low safety class: where failure of component or tubular joint implies no risk to human safety and environmental damage. When a certain damage is found in this class, its condition can be monitored and no other necessary measures needs to be applied.
- Normal safety class: where failure implies negligible risk to human safety, minor danger to the main part of the platform, minor damages to the environment, certain economic loss.
- High safety class: where failure implies risk to the total safety of the platform so as to human safety and environmental pollution. High economic loss cannot be avoided.

Table 2. Recommended Target Safety Level

Safety Class	Target	Safety
Low	$P_f = 10^{-2}$	$\beta = 2.32$
Normal	$P_f = 10^{-3}$	$\beta = 3.09$
High	$P_f = 10^{-4}$	$\beta = 3.72$

6. Results and Discussions

6.1. Reserve Strength Ratio

Pushover analysis without wave load in deck is carried out to determine reserve strength ratio. From this analysis, both the lowest and highest reserve strength ratio at maximum water depth is 1.69 and 3.72 respectively. Those are shown in Figure 2 and Figure 3. Meanwhile, Figure 4 and Figure 5 capture both the lowest and highest reserve strength ratio at minimum water depth are 1.68 and 3.79 respectively.

The lowest reserve strength ratio at maximum water depth which be shown in Figure 2 occurs in conditions when the fixed platform experienced subsidence of 2 m. Then, as be seen in Figure 4 and Figure 5, both the lowest and highest reserve strength ratio at minimum water depth happen in conditions when the structure faced subsidence of 4 m and 1 m respectively.

The reserve strength ratio from pushover analysis is used to calculate the maximum wave height of fixed platform at collapse ($H_{Collapse}$).

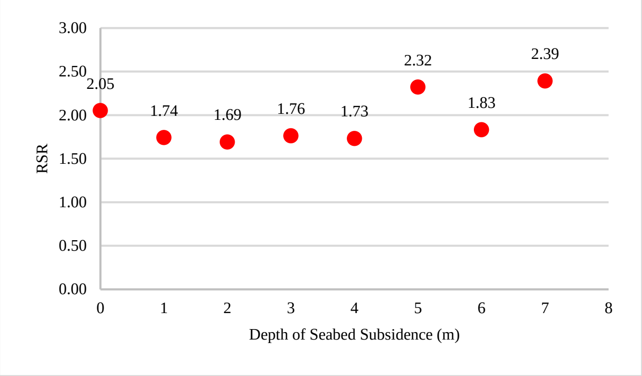

Figure 2. Reserve Strength Ratio of Fixed Platform from 90 Deg-Environmental Load at Maximum Water Depth

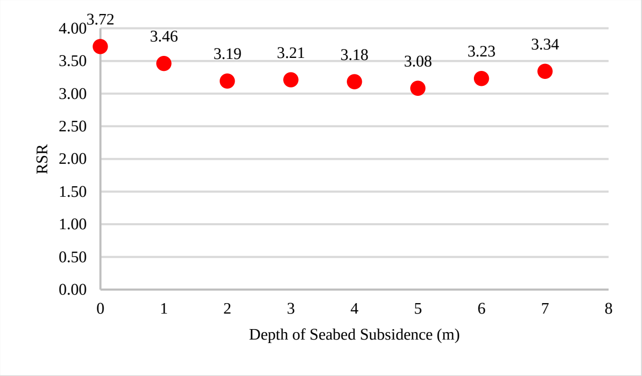

Figure 3. Reserve Strength Ratio of Fixed Platform from 180 Deg-Environmental Load at Maximum Water Depth

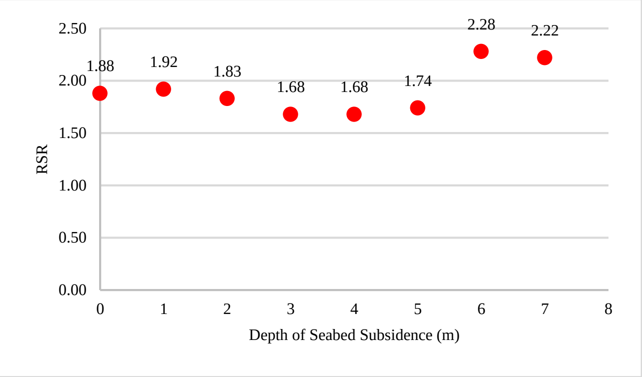

Figure 4. Reserve Strength Ratio of Fixed Platform from 90 Deg-Environmental Load at Minimum Water Depth

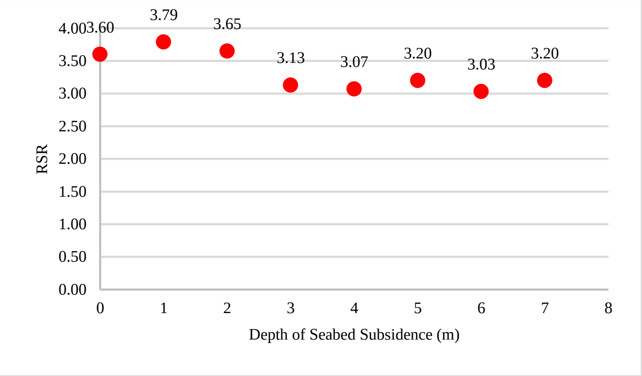

Figure 5. Reserve Strength Ratio of Fixed Platform from 180 Deg-Environmental Load at Minimum Water Depth

6.2. Maximum Wave Height at Collapse

Air gap analysis is performed to to determine whether there is wave in deck based on the reserve strength ratio from pushover analysis. The maximum wave height at collapse ($H_{Collapse}$) is calculated using Eq. (3). Next, the maximum wave crest height is compared with the bottom of steel elevation of the lowest deck structure (LD_{EL}).

Table 3 and Table 5 show that wave hitting the deck when the fixed platform is subsiding more than 0 m and 1 m by the condition of 100-year environmental load from 90º direction at both maximum and minimum water depth. Table 3 indicates that the maximum wave crest height at collapse above bottom of steel elevation is 0.71 m at the depth of subsidence of 2 m. Meanwhile, it is found in Table 5 that the maximum wave crest height at collapse above bottom of steel elevation is 0.54 m at the depth of subsidence of 1 m. Both Table 3 and Table 5 present that there are some conditions in the fixed platform that have no air gap, causing wave load in deck.

The result which are shown in

Table 4 and Table 6 describe the fixed platform is hit by wave in deck when there is no subsidence occured against the structure by 100-year enviromental load from 180º direction. Table 4 depicts that the maximum wave crest height at collapse above bottom of steel elevation is 1.51 m at no subsidence. It is also observed in Table 6 that the maximum wave crest height at collapse above bottom of steel elevation is 1.37 m at no subsidence. It can be also concluded both Table 4 and Table 6 present that all conditions in the fixed platform have no air gap and cause wave load in deck.

The condition of the maximum wave crest height which is above the bottom of steel elevation of the lowest deck indicates that there is wave in deck issue.

Table 3. Comparison Between Bottom of Steel Elevation with Maximum Wave Crest Height from 90 Deg-Environmental Load at Maximum Water Depth

Maximum Wave Height at Collapse (m)	Bottom of Steel Elevation of The Lowest Deck (m)	Maximum Wave Crest Height above BOS Elevation (m)	Depth of Seabed Subsidence (m)
12.74	7.08	-0.70	0
11.74	6.08	-0.21	1
11.57	5.08	0.71	2
11.81	4.08	1.83	3
11.71	3.08	2.78	4
13.56	2.08	4.70	5
12.04	1.08	4.94	6
13.76	0.08	6.80	7

Table 4. Comparison Between Bottom of Steel Elevation with Maximum Wave Crest Height from 180 Deg-Environmental Load at Maximum Water Depth

Maximum Wave Height at Collapse (m)	Bottom of Steel Elevation of The Lowest Deck (m)	Maximum Wave Crest Height above BOS Elevation (m)	Depth of Seabed Subsidence (m)
17.17	7.08	1.51	0
16.55	6.08	2.20	1
15.90	5.08	2.87	2
15.95	4.08	3.90	3
15.87	3.08	4.86	4
15.62	2.08	5.73	5
16.00	1.08	6.92	6
16.27	0.08	8.06	7

Table 5. Comparison Between Bottom of Steel Elevation with Minimum Wave Crest Height from 90 Deg-Environmental Load at Minimum Water Depth

Maximum Wave Height at Collapse (m)	Bottom of Steel Elevation of The Lowest Deck (m)	Maximum Wave Crest Height above BOS Elevation (m)	Depth of Seabed Subsidence (m)
13.08	7.08	-0.54	0
13.23	6.08	0.54	1
12.59	5.08	1.22	2
12.90	4.08	2.37	3
12.01	3.08	2.93	4
12.20	2.08	4.03	5
12.80	1.08	5.33	6
12.46	0.08	6.15	7

Table 6. Comparison Between Bottom of Steel Elevation with Minimum Wave Crest Height from 180 Deg-Environmental Load at Minimum Water Depth

Maximum Wave Height at Collapse (m)	Bottom of Steel Elevation of The Lowest Deck (m)	Maximum Wave Crest Height above BOS Elevation (m)	Depth of Seabed Subsidence (m)
16.89	7.08	1.37	0
17.33	6.08	2.59	1
17.00	5.08	3.43	2
15.75	4.08	3.80	3
15.59	3.08	4.72	4
15.92	2.08	5.88	5
15.49	1.08	6.67	6
15.92	0.08	7.88	7

6.3. Wave Load in Deck

Wave load in deck is calculated using Eq. (1). The maximum wave height at collapse ($H_{Collapse}$) is added in calculation which taken from air gap analysis. The fixed platform condition is moderately equipped. The current velocity is taken from metaocean data. For kinematic wave factor, the condition is assumed as hurricane. Wave load in deck is computed using Stream Function's 7th wave theory. Table 7 until Table 10 present the detailed calculation by 100-year environmental load from 90^o and 180^o direction at both maximum and minimum water depth.

Both Table 7 and Table 9 present that there are wave load in deck when the fixed platform is subsiding more than 0 m and 1 m by the condition of 100-year environmental load from 90^o direction. Table 7 shows that the minimum wave load in deck is 545.60 KN at the depth of subsidence of 2 m. Whereas Table 9 depicts that the minimum wave load in deck is 82.40 KN at the depth of subsidence of 1 m.

The result which are shown in both Table 8 and Table 10 indicate that there are wave load in deck occured against the fixed platform by 100-year enviromental load from 180^o direction at no subsidence. It is found in Table 8 that the minimum wave load in deck is 843.14 KN at no subsidence. It is also observed in Table 10 that the minimum wave load in deck is 760.02 KN at no subsidence.

Table 7. Wave Load in Deck from 90 Deg-Environmental Load at Maximum Water Depth

Projected Area of Wave in Deck (m^2)	Fluid Horizontal Velocity (m/s)	Wave Load in Deck (KN)	Depth of Seabed Subsidence (m)
-	-	-	0
-	-	-	1
25.94	5.77	545.60	2
66.86	5.82	1432.74	3
102.59	5.73	2097.17	4
172.99	6.45	4624.65	5
180.84	5.77	3793.12	6
248.86	6.42	6638.15	7

Table 8. Wave Load in Deck from 180 Deg-Environmental Load at Maximum Water Depth

Projected Area of Wave in Deck (m^2)	Fluid Horizontal Velocity (m/s)	Wave Load in Deck (KN)	Depth of Seabed Subsidence (m)
18.38	8.15	843.14	0
26.84	7.86	1138.86	1
35.02	7.55	1360.90	2
47.51	7.50	1824.78	3
59.25	7.42	2218.74	4
69.91	7.26	2502.08	5
84.39	7.35	3099.11	6
98.23	7.40	3657.01	7

Table 9. Wave Load in Deck from 90 Deg-Environmental Load at Minimum Water Depth

Projected Area of Wave in Deck (m^2)	Fluid Horizontal Velocity (m/s)	Wave Load in Deck (KN)	Depth of Seabed Subsidence (m)
-	-	-	0
3.31	6.23	82.40	1
34.53	6.04	804.67	2
61.89	5.77	1299.56	3
98.47	5.72	2024.31	4
138.78	5.75	2893.34	5
206.42	6.41	5479.80	6
239.74	6.28	6090.88	7

Table 10. Wave Load in Deck from 180 Deg-Environmental Load at Minimum Water Depth

Projected Area of Wave in Deck (m^2)	Fluid Horizontal Velocity (m/s)	Wave Load in Deck (KN)	Depth of Seabed Subsidence (m)
16.67	8.13	760.02	0
31.55	8.22	1475.39	1
41.77	8.04	1860.78	2
46.30	7.50	1775.81	3
57.56	7.38	2133.18	4
71.75	7.45	2710.92	5
81.33	7.23	2878.06	6
96.13	7.33	3512.66	7

6.4. Reserve Strength Ratio with Wave Load in Deck

Pushover analysis is performed again by including wave load in deck to dertermine the updated reserve strength ratio. Figure 6 and Figure 8 capture the lowest updated reserve strength ratio which resulted by 100-year environmental load from 90° direction at both maximum and minimum water depth are 0.85 and 0.86 respectively. These occur in conditions when the fixed platform experienced seabed subsidence of 7 m.

Meanwhile, the highest updated reserve strength ratio which resulted from the current pushover analysis at both maximum and minimum water depth are 2.82 and 2.80 respectively. It is observed from Figure 7 and Figure 9 that these highest updated reserve strength ratio is resulted by 100-year environmental load from 180° direction.

It is also found that some updated reserve strength ratio does not meet the requirement criteria from API RP-2A WSD [6], which the minimum reserve strength ratio for manned evacuated of fixed platform is 1.60.

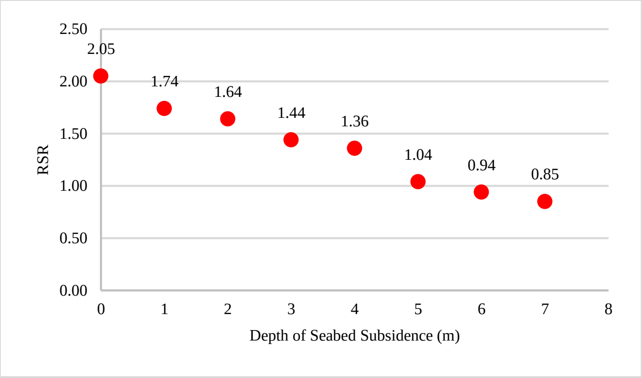

Figure 6. Reserve Strength Ratio of Fixed Platform with Wave Load in Deck from 90 Deg-Environmental Load at Maximum Water Depth

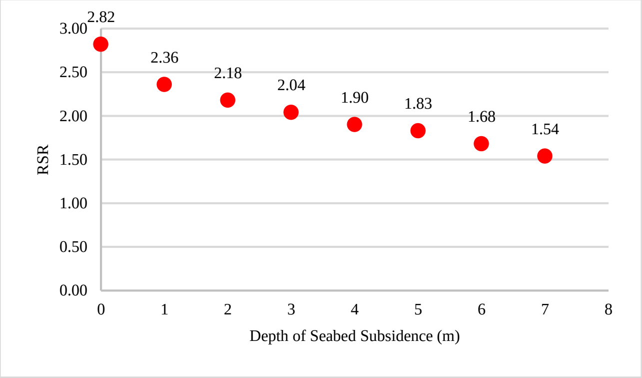

Figure 7. Reserve Strength Ratio of Fixed Platform with Wave Load in Deck from 180 Deg-Environmental Load at Maximum Water Depth

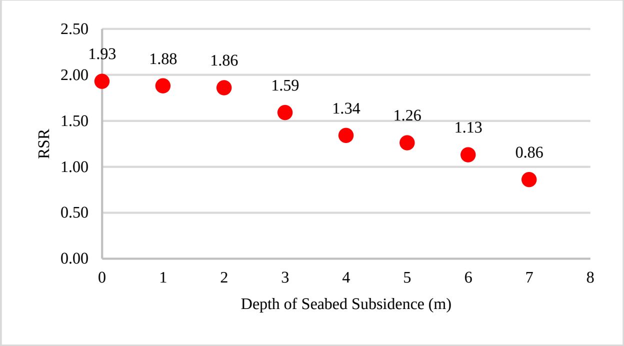

Figure 8. Reserve Strength Ratio of Fixed Platform with Wave Load in Deck from 90 Deg-Environmental Load at Minimum Water Depth

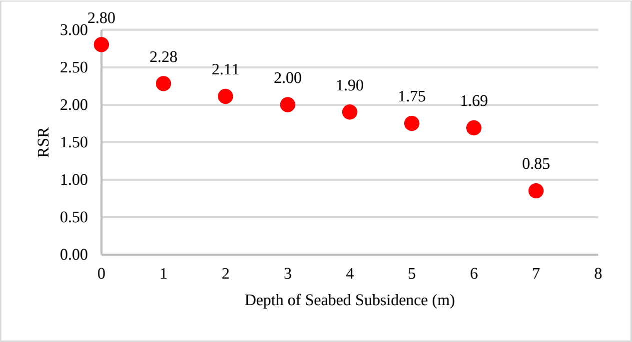

Figure 9. Reserve Strength Ratio of Fixed Platform with Wave Load in Deck from 180 Deg-Environmental Load at Minimum Water Depth

6.5. Probability of Failure

The probability of failure (P_f) is calculated using Monte Carlo simulation technique method which carried out by Matlab software. In this section, the probability of failure (P_f) results is presented in Figure 10 until Figure 13. These figures show that the probability of failure (P_f) increases with the increase of the depth of seabed subsidence.

If compared with the requirement of Marine Structural Design [14], Figure 10 indicates the probability of failure (P_f) does not meet requirement criteria when the fixed platform is subsiding more than 4 m at maximum water depth. Meanwhile, at minimum water depth, the fixed platform does not meet requirement criteria when it is subsiding more than 5 m. It is indicated in Figure 12.

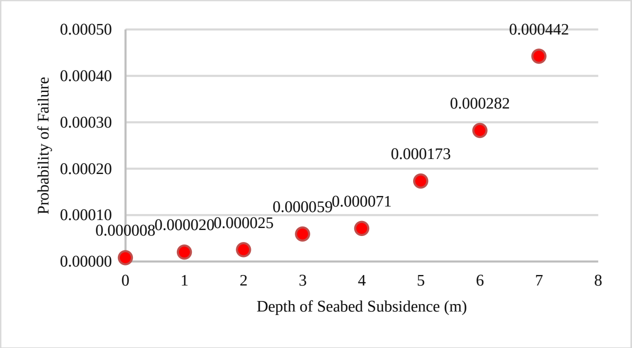

Figure 10. Probability of Failure of Fixed Platform from 90 Deg-Environmental Load at Maximum Water Depth

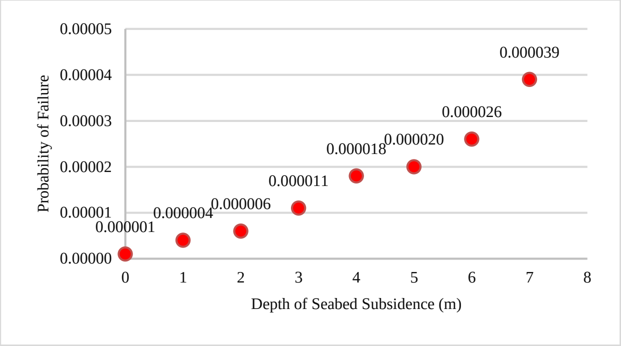

Figure 11. Probability of Failure of Fixed Platform from 180 Deg-Environmental Load at Maximum Water Depth

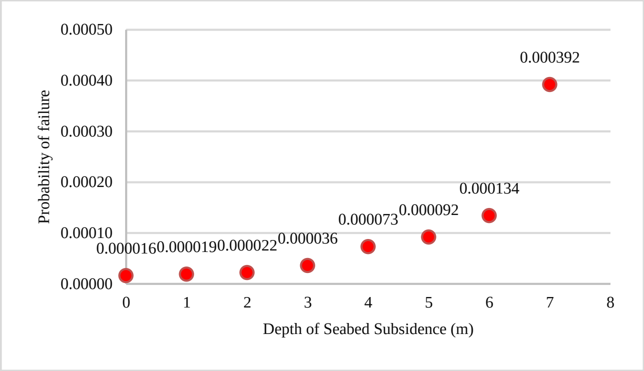

Figure 12. Probability of Failure of Fixed Platform from 90 Deg-Environmental Load at Minimum Water Depth

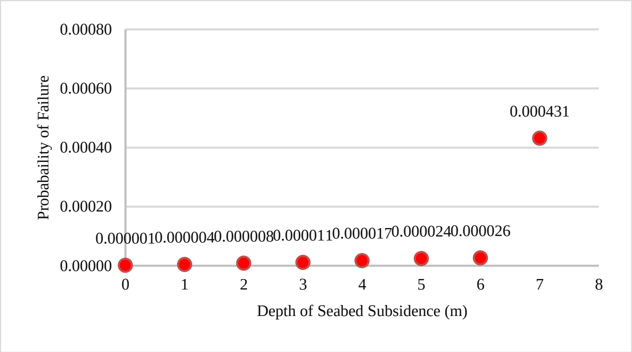

Figure 13. Probability of Failure of Fixed Platform from 180 Deg-Environmental Load at Minimum Water Depth

6.6. Reliability Index

The reliability index (β) is obtained by the probability of failure results which determined in Eq. (10). This process is performed in Matlab software. The reliability index (β) results are indicated in Figure 14 until Figure 17. As seen in these figures, the reliability index (β) decreases with the increase of the depth of seabed subsidence.

Both at maximum and minimum water depth, the highest reliability index which are resulted by 100-year environmental load from 180^o direction are 4.75. Those are shown in Figure 15 and Figure 17. Whereas Figure 14 and Figure 16 indicate that the lowest reliability index at both maximum and minimum water depth are 3.33 and 3.36 respectively. These occur when the fixed platform is subsiding about 7 m.

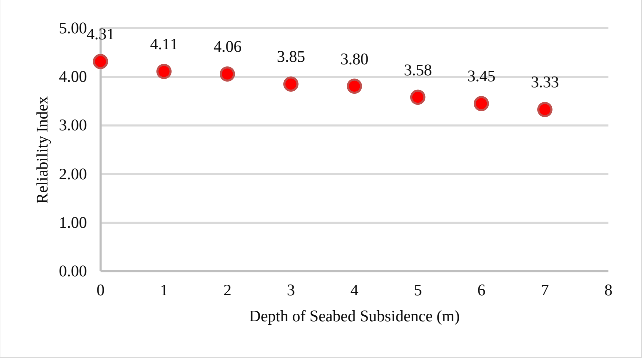

Figure 14. Reliability Index of Fixed Platform from 90 Deg-Environmental Load at Maximum Water Depth

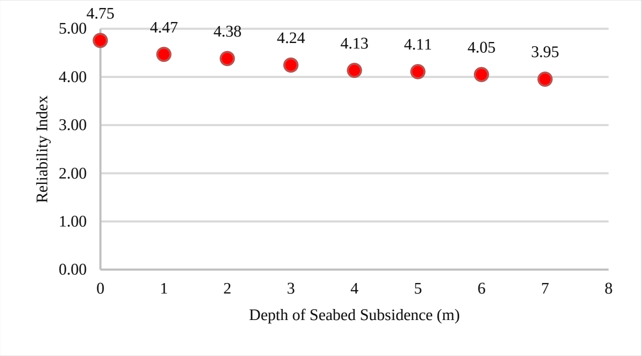

Figure 15. Reliability Index of Fixed Platform from 180 Deg-Environmental Load at Maximum Water Depth

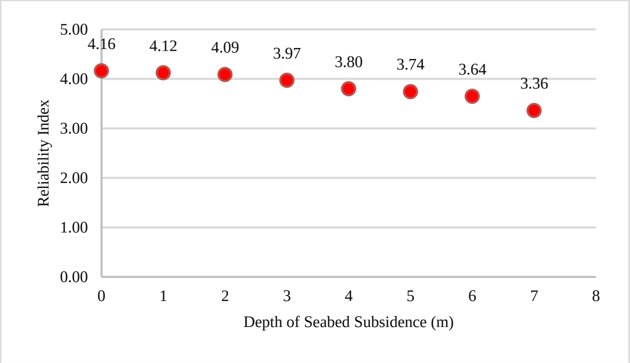

Figure 16. Reliability Index of Fixed Platform from 90 Deg-Environmental Load at Minimum Water Depth

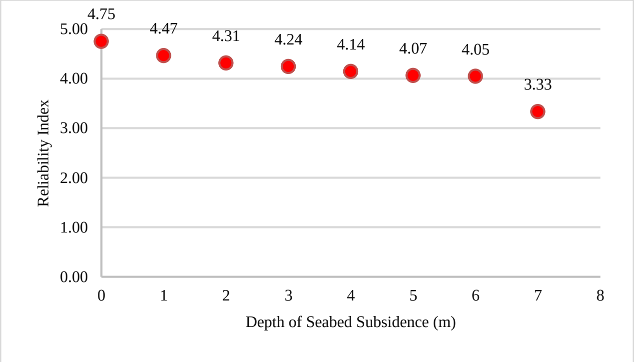

Figure 17. Reliability Index of Fixed Platform from 180 Deg-Environmental Load at Minimum Water Depth

6.7. Recommended Target Safety Level

In this study, the reliability index target is taken from Bai [21] which the target from high safety class is used as a reference. This reliability index target is 3.72.

If compared with the reliability index (β) that calculated in Section 6.6, the reliability index (β) of fixed platform is lower than the reliability index target when the structure is subsiding more than 4 m by 100-year environmental load from 90⁰ and 270⁰ at maximum water depth. Those are presented in Figure 19 and Figure 21. Whereas Figure 18 and Figure 20 indicate that the reliability index (β) of fixed platform is lower than the reliability index target when the structure is subsiding more than 5 m by 100-year environmental load from 65⁰ and 245⁰ direction at maximum water depth.

As can be seen in Figure 22 and Figure 25, the fixed platform has reliability index (β) which is lower than the reliability index target when the structure is subsiding more than 4 m at minimum water depth. These conditions occur when the structure is subjected to 100-year environmental load from 65⁰ and 270⁰ direction. Meanwhile, it is observed in Figure 23 that the reliability index (β) is lower than the reliability index target when the fixed platform is subsiding more than 5 m due to 100-year environmental load from 90⁰ direction at minimum water depth.

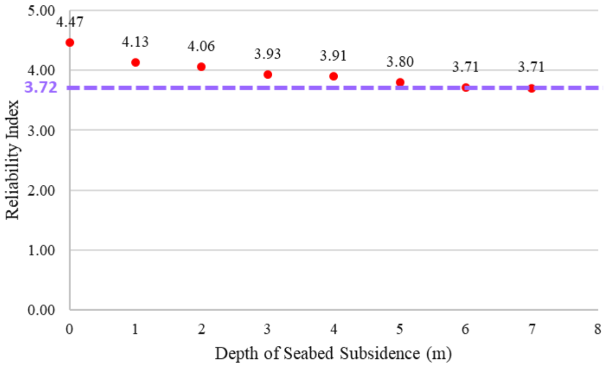

Figure 18. Recommended Target Safety of Fixed Platform from 65 Deg-Environmental Load at Maximum Water Depth

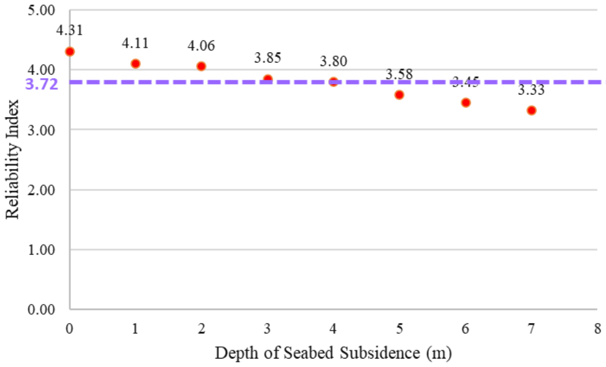

Figure 19. Recommended Target Safety of Fixed Platform from 90 Deg-Environmental Load at Maximum Water Depth

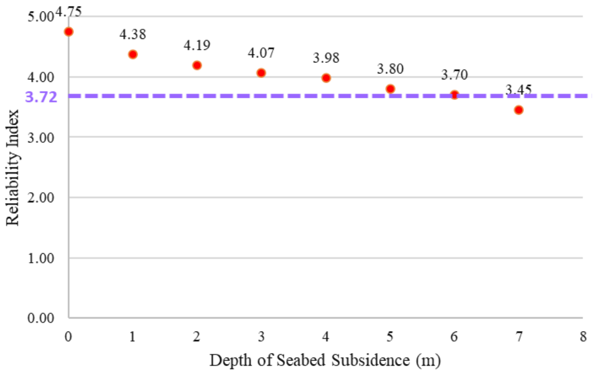

Figure 20. Recommended Target Safety of Fixed Platform from 245 Deg-Environmental Load at Maximum Water Depth

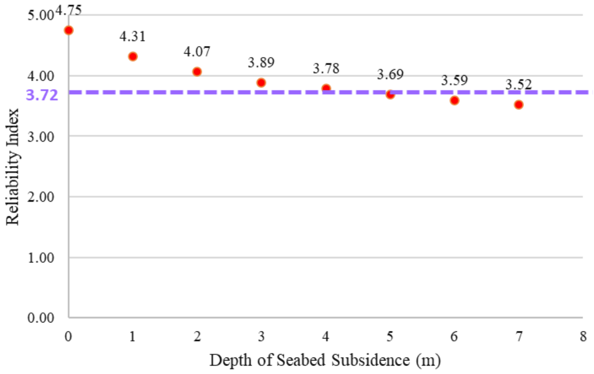

Figure 21. Recommended Target Safety of Fixed Platform from 270 Deg-Environmental Load at Maximum Water Depth

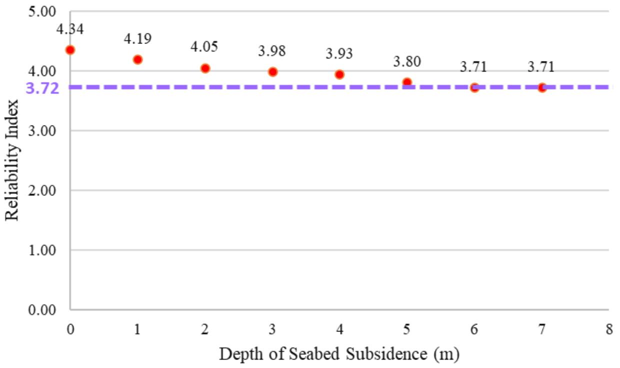

Figure 22. Recommended Target Safety of Fixed Platform from 65 Deg-Environmental Load at Minimum Water Depth

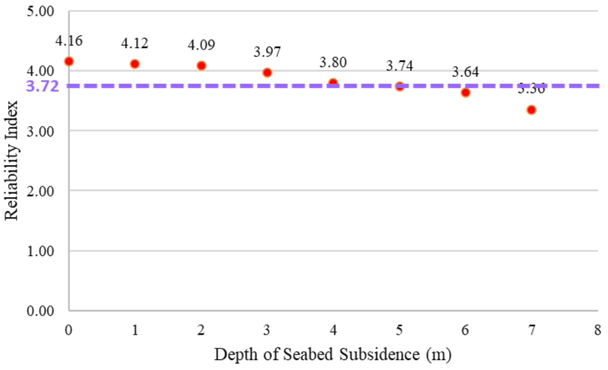

Figure 23. Recommended Target Safety of Fixed Platform from 90 Deg-Environmental Load at Minimum Water Depth

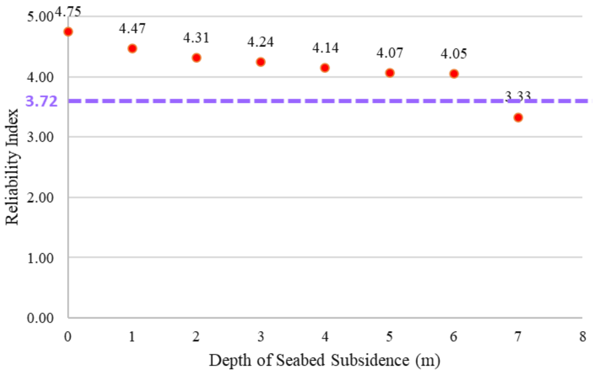

Figure 24. Recommended Target Safety of Fixed Platform from 180 Deg-Environmental Load at Minimum Water Depth

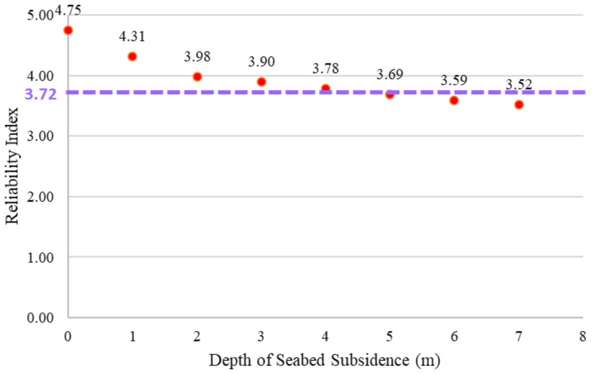

Figure 25. Recommended Target Safety of Fixed Platform from 270 Deg-Environmental Load at Minimum Water Depth

7. Conclusions and Recommendations

The following conclusions can be drawn from the results of the study.

- Pushover analysis is widely performed to calculate the reserve strength ratio of the fixed platform. The result of the reserve strength ratio without wave load in deck is detailed in Section 6.1. It is indicated that the lowest reserve strength ratio is 1.68, which means still meet requirement criteria of the minimum reserve strength ratio for manned evacuated of fixed platform from API RP-2A WSD [11].
- Air gap analysis is carried out based on the reserve strength ratio which resulted from pushover analysis. The analysis is required to determine whether the fixed platform is hit by wave in deck. By the results in Section 6.2, almost all conditions present that there is wave in deck. Therefore, it is necessary to rerun the pushover analysis with wave load in deck.
- Pushover analysis with wave load in deck is conducted to obtain the updated reserve strength ratio when the wave hit the deck. It is found from the results in Section 6.4 that the updated reserve strength ratio with wave load in deck is lower than the updated reserve strength ratio without wave load in deck. Higher reserve strength ratio due to the wave in deck can cause the bigger chance for the fixed platform will collapse. It is

crucial to include the wave load in deck analysis due to seabed subsidence in pushover analysis. Moreover, there are some conditions which present the updated reserve strength ratio are less than 1.0. These mean the structure may globally collapsed by wave height which is lower than 100-year maximum wave height (H_{100}) due to seabed subsidence and wave load in deck.

- Monte carlo simulation techniques method is adopted in reliability analysis. The results are presented in Section 6.6. Both the highest and lowest reliability index (β) which resulted from calculation are 4.75 and 3.33 respectively. However, some reliability indexes are lower than the target of high safety class which referred to Bai [21].
- The pushover and reliability analysis are carried out by including environmental load in eight directions. The analysis results which are shown in this paper are only the highest and lowest results obtained from the different directions of environmental load on the total load combinations. The highest result comes from the 180^{o} environmental load. Whereas the lowest result comes from the 90^{o} environmental load. The total load of the fixed platform is gained from the dead load, live load and environmental load in each direction. The uncertainties of environmental conditions which are represented by wave height and wave period indicate the contributions of environmental load directions both in the jacket and deck to the whole fixed platform's strength and reliability.

By the results which given in this study, the following recommendations can be further conducted in the future.

- The method which is used to calculate wave load in deck may be further studied by considering the type and geometry of the fixed platform. There are other methods to calculate wave load in deck such as component method, CFD method, morison equation method and diffraction method.
- In this study, the wave load in deck is focused on horizontal wave load in deck. It would be better if the vertical wave load in deck is also considered in pushover analysis.
- The structural analysis which carried out in current study is static non-linier pushover. It is recommended to perform dynamic analysis by including wave load in deck.
- Reliability analysis is performed by Monte Carlo simulation technique method. There are other methods to calculate probability of failure (P_f) and reliability index (β). The reliability analysis can be performed in some methods which those results then compared each other.

List of Symbols

LD_{EL}	Bottom of steel of lowest deck
A_{deck}	Projected area of wave in deck
A_{deckx}	Projected area of wave in deck in X-axis
A_{decky}	Projected area of wave in deck in Y-axis
C_D	Drag coefficient
E_{100}	Base shear of 100-year environmetal load
$E_{collapse}$	Base shear of fixed platform at collapse
E_i	Base shear of fixed platform
F_{Deck}	Wave load in deck
H_{100}	100-year maximum wave height
$H_{Collapse}$	Wave height of fixed platform at collapse
H_s	100-year significant wave height
H_i	Random wave height
P_f	Probability of failure
R	Resistance / capacity of the structure
S	Load on the structure
T_i	Random wave period
T_p	100-year peak period
U	Current velocity in line with wave
V	Fluid horizontal velocity
Z	Performance function
α	Metaocean constant
α_{cb}	Current blockage factor
α_{wk}	Wave kinematic factor
β	Reliability index
θ_w	Wave direction
ρ	Seawater density

References

[1] Zaki, N.M., Abu Husain, M., Najafian, G. (2014), *Extreme Structural Response Values from Various Methods of Simulating Wave Kinematics*, Ships Offshore Struct. 2014, Vol.11, p.1-16,

[2] Ayob, M.S., Kajuputra, A.E., Wong, B.S., (2014), *Global Ultimate Strength Assessment for Existing Offshore Jacket Structures*, In Proceedings of the Offsshore Technology Conference Asia, Kuala Lumpur, Malaysia, 25-28 March 2014.

[3] Kang, B.J., Kim, J.H., Kim, Y, (2016), *Engineering Criticality Analysis on an Offshore Structure using the First and Second-Order Reliability Method*, International Journal Naval Architecture Ocean, Vol.8, p.577-588.

[4] Ng, S.M., Khan, R., Isnadi, B., Lee, L.A., Saminal, S.N., (2019), *A Holistic Approach to Life Extension of Fixed Offshore Platforms in Malaysian Waters*, In Proceedings of the International Petroleum Technology Conference, Beijing, China, 26-28 March 2019.

[5] Nagel, N., (2001), *Compaction and Subsidence Issues within The Petroleum Industry: From Wilmington to Ekofisk and Beyond*, Physics and Chemistry of the Earth, Part A: Solid Earth and Geodesy, Vol.26, p.3-14.

[6] Amdahl, J., Holmas, T., (2016) *ISUM for Offshore Frame Structures*, Proceedings of the International

Conference on Offshore Mechanic and Arctic Engineering, Busan, South Korea, 19-24 June 2016.

[7] Jafari, A., Dezvareh, R., (2021), *Evaluation of Dynamic Effects in Tthe Response of Offshore Wind Turbines Using Incremental Wind-Wave Analysis*, Research in Marine Sciences, Vol.265, p.860-868.

[8] Nazokkar, A., Dezvareh, R., (2022), *Vibration Control of Floating Offshore Wind Turbine Using Semi-Active Liquid Column Gas Damper*, Ocean Engineering, Vol.265.

[9] Yee, N.C., Johan, A., Kajuputra, A.E., Pangestu, L.A., (2020), *Evaluation of Factors Contributing to Wave-in-deck Using Pushover Analysis for Fixed Jacket Structures*, IOP Conference Series: Earth and Environmental Science, Vol. 419.

[10] Azman, N.U., Abu Husain, M.K., Mohd Zaki, N.I., Mat Soom, E., Mukhlas, N.A., Ahmad, Sayyid Zainal Abidin Syed., (2021). *Structural Integrity of Fixed Offshore Platform by Incorporating Wave in Deck*, In Proceedings of the 35th International Conference on Ocean, Offshore and Arctic Engineering, Busan, Korea, 19-24 June 2021.

[11] American Petroleum Institute, (2014), *Recommended Practice for Planning, Designing, and Constructing Fixed Offshore Platforms—Working Stress Design*, American Petroleum Institute: Washington DC, USA.

[12] Finnigan, T.D., Petrauskas, C., (1997). *Wave-in-deck Forces*, In Proceedings of the 7th International Offshore and Polar Engineering Conference, Honolulu, Hawai, USA, Vol.3, p.19-24.

[13] Kaplan, P., Murray, J.J., Yu, W.C., (1995), *Theoretical Analysis of Wave Impact Forces on Platform Deck Structures*, In Proceedings of the 14th International Conference on Offshore Mechanics and Arctic Engineering (OMAE), Copenhagen, Denmark.

[14] Chen, Y., Wu, Y., Bahuguni, A., Gullman-Strand, J., Zhang, Y., Stewart, G., Lv, X., (2016), *Advances in Computational Hydrodynamics Applied to Wave-in-Deck*, In Proceedings of the Offshore Technology Conference Asia, Kuala Lumpur, Malaysia, 22-25 March 2016.

[15] Iwanowski, B., Grigorian, H., Scherf, I., (2002), *Subsidence of the Ekofisk Platforms: Wave in Deck Impact Study-Various Wave Models and Computational Method*, In Proceedings of the 21st International Conference on Offshore Mechanics and Artic Engineering, Oslo, Norway, 23-28 June 2002.

[16] Ma, L., (2018), *The Effective Modelling of Wave-In-Deck Loads*, Ph.D. Thesis, Department of Civil and Environmental Engineering, Imperial College London, London, UK.

[17] Singh, D., Panneerselvam, N., Kumar, D., (2015), *Reliability Analysis of Strength of Offshore Jackets in Indian Western Offshore*, In Proceedings of the SPE Oil and Gas India Conference and Exhibition, Mumbai, India, 24-26 November 2015.

[18] Haldar, A., Mahadevan, S., (2000), *Probability, Reliability, and Statistical Methods in Engineering*, New York: John Wiley & Sons, Inc.

[19] Tabeshpour, M.R., Mahmoudi, M.R., (2021), *Reliability analysis of Tension-Leg Platform Tendon with Respect to Fatigue Failure under Environmental Condition of Caspian Sea*, International Journal of Coastal, Offshore and Environmental Engineering, Vol.6, p.1-6.

[20] Taheri, A., Tasdighi, M., Faraji, M.B., (2019), *Reliability Analysis of Subsea Pipeline against Upheaval Buckling*, International Journal of Coastal, Offshore and Environmental Engineering, Vol.4, p.17-23.

[21] Bai, Y., (2003), *Marine Structural Design*, Houston, USA: Elsevier Ltd.

INTERNATIONAL JOURNAL OF
COASTAL, OFFSHORE & ENVIRONMENTAL ENGINEERING
IJCOE Vol.8/No. 2/Spring 2023 (13-20)

The comparison of the safety zone in the vicinity of marine clay treatment areas with and without surcharge and vacuum preloading

Mohammad Mehdi Pardsouie[1*], Mehdi Mokhberi[2], Mohammad Hadi Pardsouie[3], Mir Masoud Kariminejad[4]

[1*] *PhD candidate, Department of geotechnical engineering, Estahban Branch, Islamic Azad University, Estahban, Iran, m.m.pardsouie@gmail.com*
[2] *Associate professor, Department of geotechnical engineering, Estahban Branch, Islamic Azad University, Estahban, Iran*
[3] *M.Sc. student, Department of civil engineering, Estahban Branch, Islamic Azad University, Estahban, Iran*
[4] *M.Sc. student, Department of civil engineering, Yasouj Branch, Islamic Azad University, Yasouj, Iran*

ARTICLE INFO

Article History:
Received: 11 Oct. 2022
Accepted: 24 Apr. 2023

Keywords:
Vacuum preloading
Influence zone
Surcharge preloading
PVD
clay

ABSTRACT

One of the important parameters that should be considered in designation of weak clay and peats treatment systems is the influence zone wherever there are infrastructures or sensitive buildings in the vicinity of the treatment area. Since large vertical and horizontal displacements occur in these treatment systems, the soil around the project undergoes large strains that should be accounted for in project planning prior to finalization of the treatment system. The treatment systems for weak clays and peats are often a combination of prefabricated vertical drains plus vacuum and/or surcharge preloading. For investigation of the impact of preloading agents, and FEM simulation of two case histories were performed. One the project incorporates the combination of surcharge and vacuum preloading while the other one consisted of only vacuum preloading without surcharge embankment. Based on the verified models, different scenarios were introduced for comparison of impact of the vacuum and preloading agents on the magnitude of the influence zone. Regarding the impact of surcharge embankment, it was shown that reducing the height of surcharge can drastically reduce the influence zone in both numerical simulations. The application of vacuum preloading as the only preloading agent has decreased the influence zone drastically and for urban areas or places that sensitive infrastructures exist might be an ideal option for similar cases. Regarding the impact of magnitude of vacuum pressure on the influence zone it was shown that application of a stable high vacuum pressure can significantly reduce the diameter of the influence zone. For every project that includes the treatment of weak clay or peat stratums, based on the material and sensitivity of nearby structures and infrastructures, the maximum allowable strains should be determined prior to designation of the treatment system to avoid unpredicted damage by qualified consultants.

1. Introduction

Due to the rapid propagation of urban areas and industrial facilities especially in coastal regions and places that were considered unsuitable before for any kind of construction, the treatment and reinforcement of weak soil stratums becomes an evitable part of the development plans[2, 3]. Marine weak clays and loose peats are two common types of soils that are mostly encountered. One of the popular methods for treatment of such soils is the application of PVDs and vacuum and surcharge preloading. The systems are a combination of all these methods and sometimes each one of them individually. As a result of huge vertical and lateral displacements that occur in such treatment systems, one of the important issues that should be considered along with the efficiency of such systems is the existence of sensitive infrastructures and structures, especially in urban areas where there is a condensed volume of pipelines and cables. Based on the material and tolerance of such pipelines or trenches, the maximum allowable shear strains should be determined prior to the designation of the treatment system. Based on the allowable strains, the influence zone can be determined by FEM or analytical approach.

Nguyen et al [4] performed a finite element analysis for analysis of a treatment system that incorporates vacuum and surcharge preloading as the remediation agent, for determination of the influence zone for a project where cracks were observed in the vicinity of the treatment area. Tashiro et al [5] constructed a test embankment for the investigation of large deformation that could have occurred in construction of the main embankment and ran a coupled soil-water analysis for prediction of deformations. The field data and simulations were used for planning counter-measures in the designation of the main embankment. Liu et al [6] proposed a direct relationship between maximum value of the lateral displacement (ELD) and the distance from the treated area boundary, considering the length of the prefabricated vertical drain for estimation of influence zone in treatment incorporating vacuum preloading for a case study. Since every project has its own unique specifications, the proposed relation by [6] can only give a firsthand estimation as they themselves announced and more precise calculation should be done prior to the finalization of the design process.

In this paper a FEM approach is applied for the investigation of the impact of surcharge embankment and vacuum preloading on the diameter of the influence zone for soil treatment systems. Two case studies were modeled and verified and based on these models various scenarios were introduced for comparison of various combinations of incorporating parameters on the influence zone.

2.Material and Methods

Two case histories are introduced and verified in order to investigate the effect of the surcharge and vacuum preloading on the diameter of the safe zone in the premier of treatment area. The first case history is the TV2 test embankment that was built in international Bangkok airport for the investigation of vacuum preloading along with PVDs and surcharge. The second one is the soil treatment project that was accomplished for the construction of a residential complex that was situated beside the coastal area using PVDs and vacuum preloading. Both case histories were constructed on weak stratums of weak Bangkok clay that is very unsuitable for infrastructure construction issues as a result of low shear strength[1, 7]. In both mentioned case histories, the soil treatment was inevitable. For Bangkok airport the combination of vacuum and surcharge preloading was used, while in the residential complex project only vacuum preloading was used and there was no surcharge embankment[8]. Since the surcharge preloading was absent in one the case histories, it was used as a measure to investigate the effect of surcharge preloading on safe zone perimeter. The procedure of finite element (FE) modelling is complex and was done by the authors in Pardsouie et al [9, 10] that can be accessed by readers for detailed information. More details and specifications regarding TV2 test embankment and the residential complex construction and instrumentation can be accessed in Bergado et al [11, 12] and in chaiyaput et al [7]. Fig 1a and 1b shows the application of surcharge and vacuum preloading in TV2 and fig 1c shows the application of vacuum preloading in residential complex vs time.

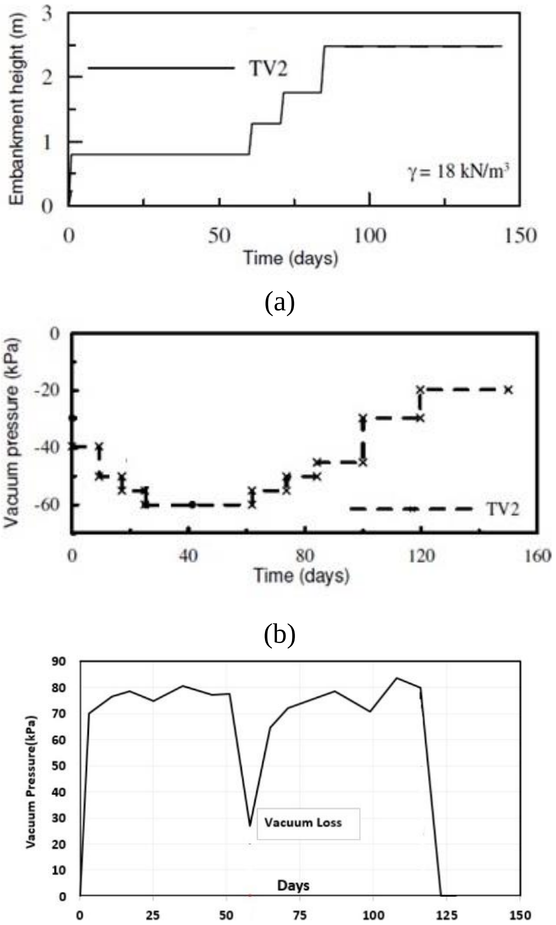

(a)

(b)

(c)

Figure 1. (a) the sequence of the construction of TV2 embankment vs time (b) the application of vacuum preloading in TV2 vs time (modified after [13]) (c) the application of vacuum preloading in residential complex vs time (modified after [8])

Fig 2 shows the soil profile section of the TV2 embankment.

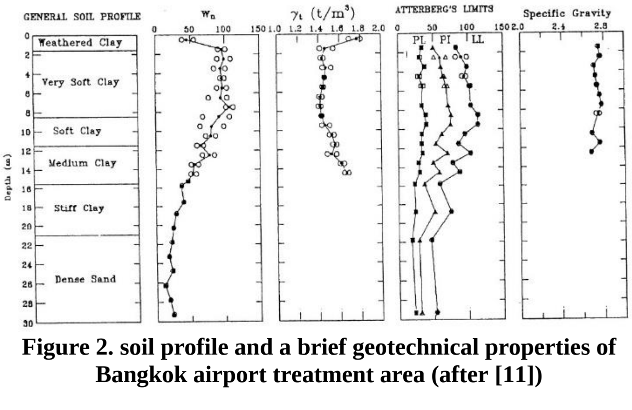

Figure 2. soil profile and a brief geotechnical properties of Bangkok airport treatment area (after [11])

Figure 3 shows the verifications of the FEM models vs measured data of the settlements in the field for both case histories (measured data from [8, 13]. As it can be seen for the residential complex the FEM model over predicts the settlement quantities where the final settlement was estimated correctly. This might be attributed to the delay stress transferred for fine grained soil that were reported by [14-16]. Since the mechanism of the transference of vacuum preloading to the soil structure is completely different from surcharge embankment, the inaccuracy of the hydraulic modifier function as stated by [10] might also be the reason for overestimation of the settlement curve.

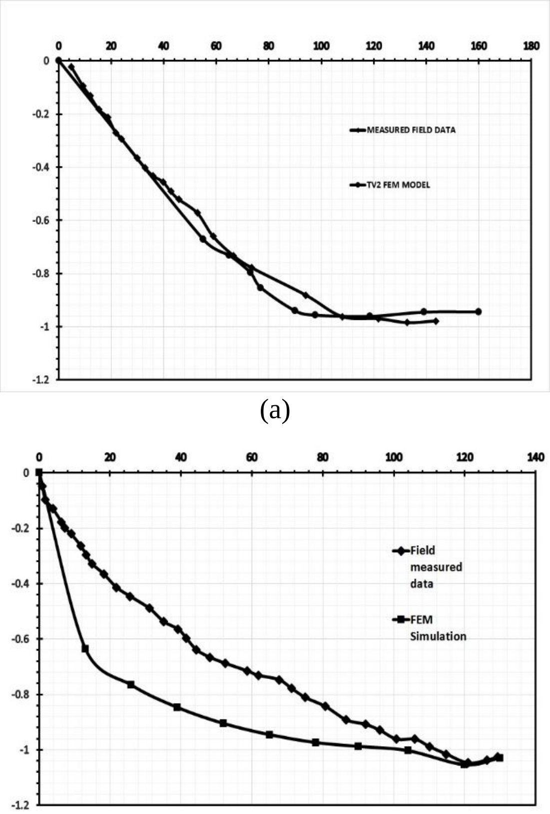

(a)

(b)

Figure 3. the verification of the two case histories FEM models for settlement vs time (a) TV2 after 160 days (b) residential complex after 130 days

Based on the verified TV2 FEM, simulations were carried out for different situations as the cases with surcharge and PVDs, vacuum preloading and PVDs, and the case with the application of an ideal constant 60 kPa vacuum preloading for comparison of the different scenarios. Fig 4 shows the schematic view of the TV2 model used in the analysis.

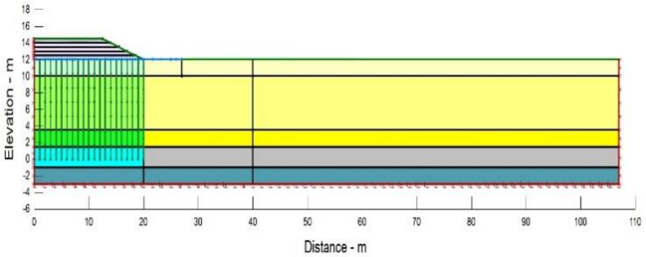

Figure 4. The schematic view of the TV2 model

3. Results and discussions

3.1. The impact of the surcharge embankment

3.1.1. Residential complex

As it can be seen in figure 5, the influence zone for the verified model is only 9.2 m, which is a very low value in comparison to other cases while for the case with equivalent surcharge it has increased to 55.8 m. Based on the figure 6, the equivalent surcharge for the residential case history is an embankment that is 5 m height which has been built in 130 days and remained for another 370 days without PVDs. The assumed case with equivalent surcharge demonstrates the high efficiency of the vacuum preloading even in the absence of surcharge embankment. The application of vacuum preloading as the only preloading agent has decreased the influence zone drastically and for urban areas or places that sensitive infrastructures exist might be an ideal option for similar cases.

It should be mentioned that for surcharge preloading the displacement is 0.05 cm outward while for the case that includes only vacuum preloading the displacement is -0.02 inward. This issue was also reported by chai et al [17, 18]. The vacuum pressure unlike surcharge preloading causes an inward movement toward the center of treatment area and as a result, a balanced combination of surcharge and vacuum preloading might be a good option for designers where there is a great concern regarding lateral movement and the diameter of the influence zone.

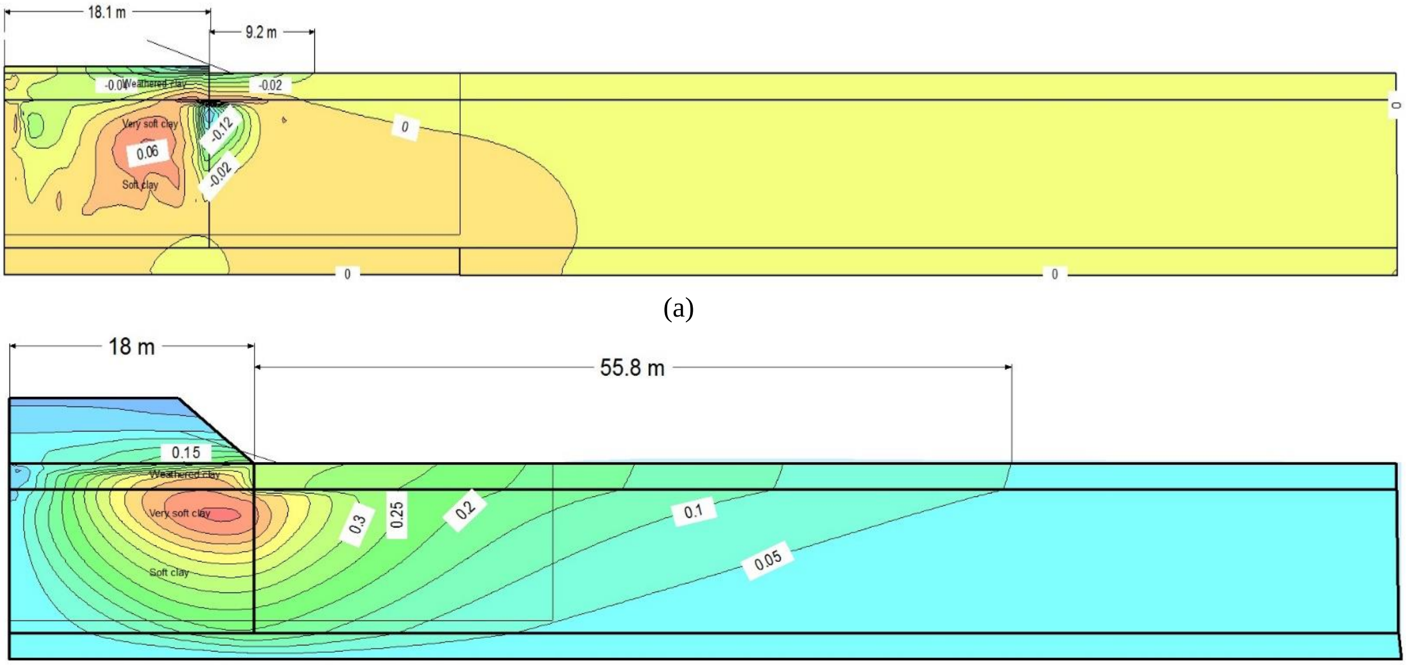

(a)

Figure 5. The contour diagram of the x-displacement of the perimeter of the residential complex treatment area (a) verified case study after 130 days (b) the equivalent surcharge embankments after 500 days

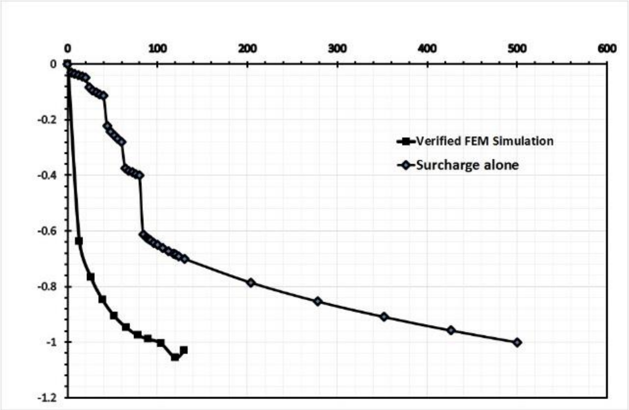

Figure 6. the comparison of the settlement curves of verified FEM model vs time with equivalent surcharge load

3.1.2. TV2 test embankment

In order to compare the impact of surcharge preloading a case has been defined based on the TV2 verified model that lacks the surcharge embankment. The settlement curve and influence zone for the defined case are shown in figure 8 and 7b. For the case of TV2 with 2.4 m surcharge and variable vacuum pressure vs time as it was shown in figure 1a and 1b, the influence zone is equal to 49.6 m while for this case in the absence of surcharge preloading, the influence zone is equal to 20.5 m (figure 7a and 7b). In figure 8 it can be seen that by omission of the surcharge embankment the final settlement has reduced from 1.27 to 0.73 m. The applied vacuum pressure in the case of TV2 was not a constant and stable pressure unlike the residential complex and for TV2 case the lateral displacements have positive values. Although the settlement is lesser in comparison to the TV2 verified FEM simulation in figure 7b, the magnitude of final settlement is 42 percent smaller.

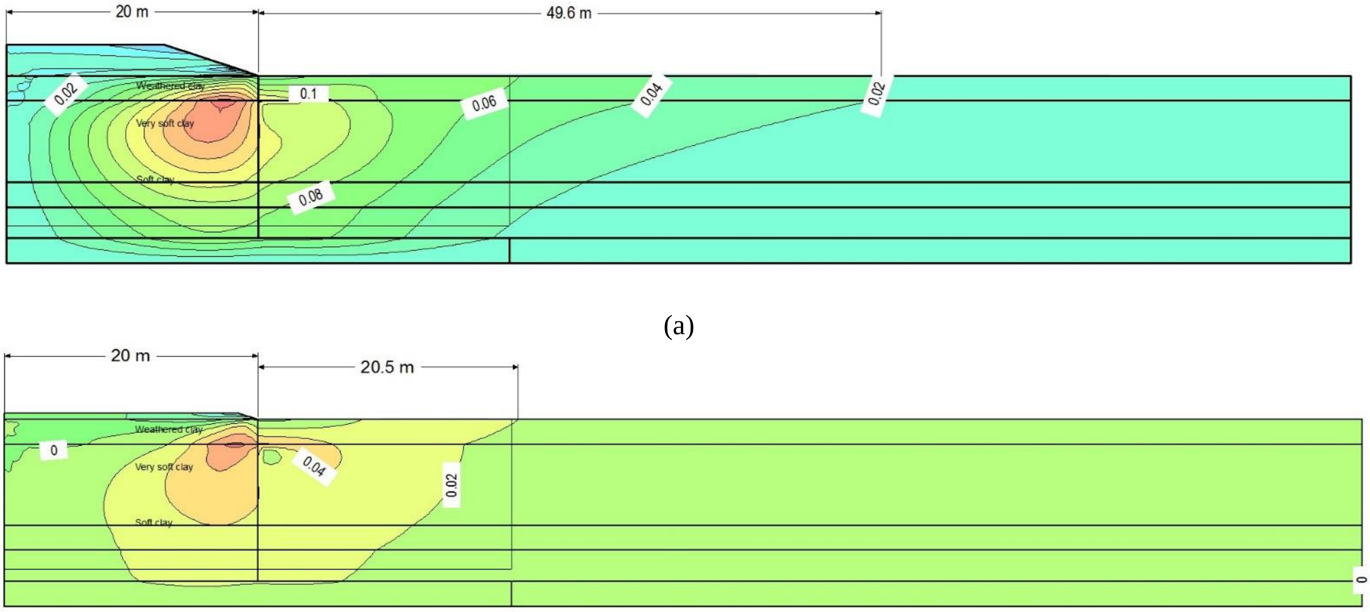

(a)

(b)

Figure 7. The contour diagram of the x-displacement of the perimeter of the TV2 treatment area (a) FEM verified model (b) The case without surcharge preloading

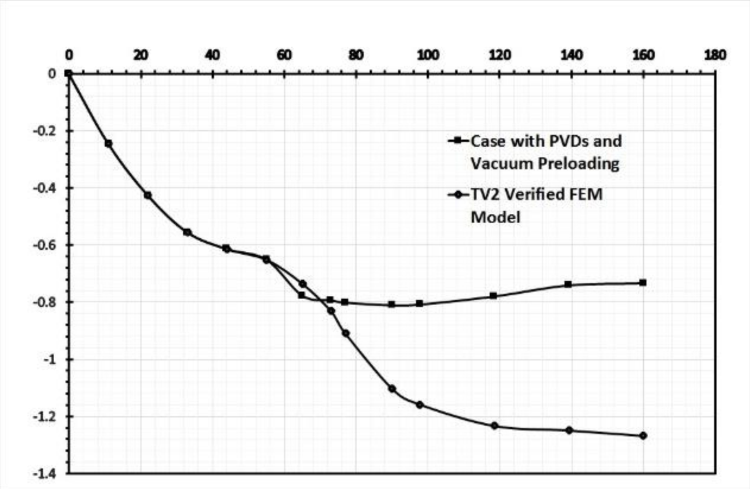

Figure 8. the comparison of the settlement curves of verified FEM model vs time with the case on the absence of surcharge preloading

3.2. The impact of the magnitude of vacuum preloading

3.2.1. TV2 test embankment

Figure 9a illustrates the TV2 case with a constant ideal 60 kPa vacuum pressure in combination with 2.4 m surcharge preloading. The influence zone for this case is 14.1 m that is drastically reduced in comparison to the verified TV2 case that had a 49.6 m influence zone (figure 7a). It is clear that a stable vacuum preloading can significantly reduce the diameter of the influence zone. For the case of constant 60 kPa pressure in the absence of surcharge preloading for TV2, the influence zone is 12.7 m and the displacement is towards the center of the embankment as it is shown in figure 9b. The exclusion of the surcharge embankment has reduced the influence zone by 1.4 m while the final settlement has reduced from 1.92 to 1.44 m. The final settlement with stable vacuum pressure in the absence of surcharge embankment is still higher than the verified TV2 model (1.44 in comparison to 1.26). This case shows the great impact of a stable vacuum preloading in overall system efficiency and reduction of the influence zone for such treatment systems.

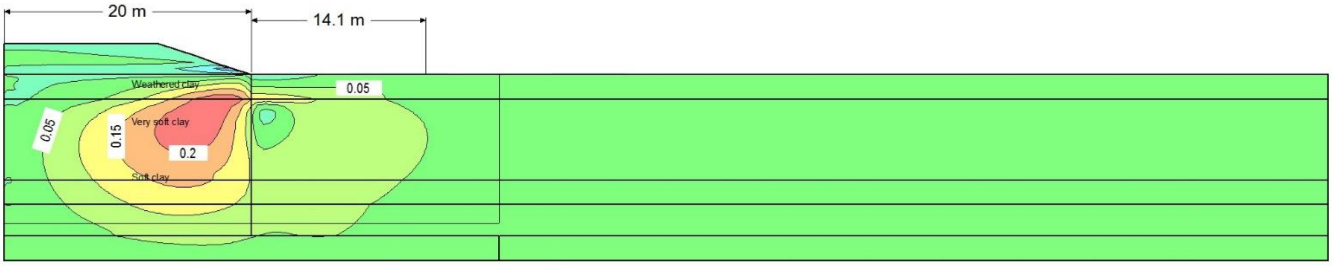

(a)

(b)

Figure 9. The contour diagram of the x-displacement of the perimeter of the TV2 treatment area (a) TV2 FEM model with constant 60 kPa vacuum preloading (b) The case with constant 60 kPa vacuum preloading in the absence of surcharge preloading

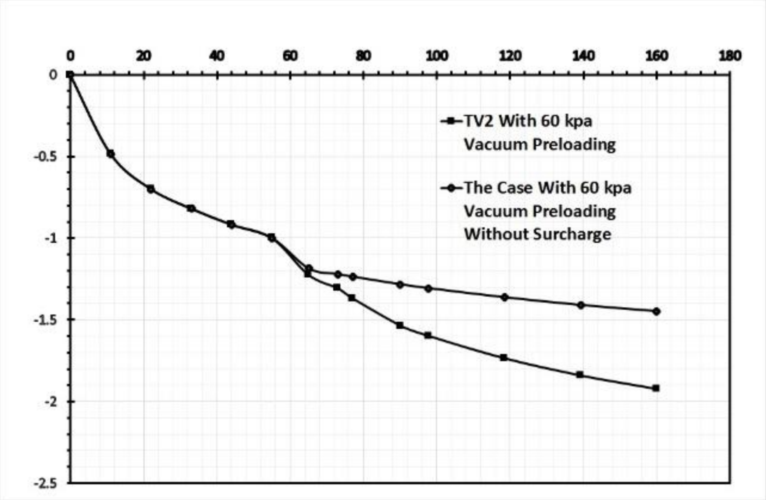

Figure 10. the comparison of the settlement curves of TV2 FEM model with 60 kPa vacuum preloading vs the case with 60 kPa vacuum preloading in the absence of surcharge preloading

3.2.2. Residential complex

Although it might be assumed that only outward lateral displacement can cause the damage to structures and infrastructures in the vicinity of treatment areas, a stable high pressure vacuum has the potential for the similar impact like surcharge embankment as it is shown in figure 11. Figure 11 shows the influence zone in a case that a constant 80 kPa vacuum pressure was applied to the verified complex case where as it is shown in figure 1c, there were malfunctions and leakages in the air pressure system that was also reported by [8]. The influence zone has increased from 9.2 m in the verified FEM case to 18.5 m in the case with constant 80 kPa vacuum pressure. The final settlement for ideal constant pressure has increased from 1.05 to 1.15 m that is shown in figure 12. This case again shows the benefits of designation of a system that a balanced combination of surcharge and vacuum pressure be applied.

Figure 11. The contour diagram of the x-displacement of the perimeter of the residential complex treatment area with constant 80 kPa vacuum preloading

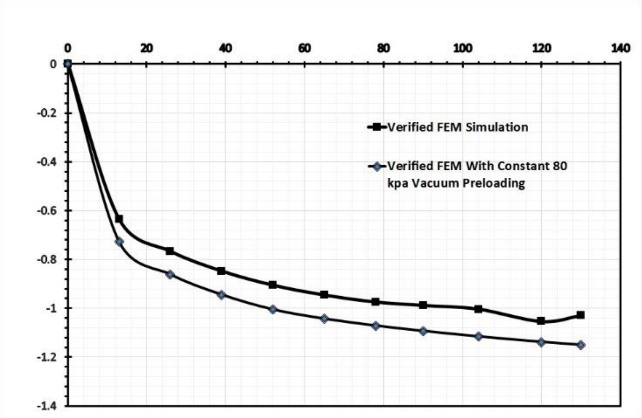

Figure 12. The comparison of the settlement curves of residential verified FEM model vs the verified case including constant 80 kPa vacuum preloading

4. conclusion

Two case histories were introduced and verified for investigation of the impact of surcharge embankment and vacuum preloading on the diameter of the influence zone; both were located on Bangkok marine clay. The first case history was TV2 that was a combination of vacuum pressure and surcharge embankment. The second case history was the application of vacuum preloading excluding the surcharge embankment. Based on the verified FEM simulation other cases were introduced as the equivalent surcharge embankment for residential complex and the application of ideal stable vacuum pressure for both residential and TV2 embankment.

Regarding the impact of surcharge embankment, it was shown that reducing the height of surcharge can drastically reduce the influence zone in both numerical simulations. For residential complex the assumed case with equivalent surcharge embankment demonstrates the high efficiency of the vacuum preloading even in the absence of surcharge embankment. The application of vacuum preloading as the only preloading agent has decreased the influence zone drastically and for urban areas or places that sensitive infrastructures exist might be an ideal option for similar cases. For the case of verified TV2 with 2.4 m surcharge and vacuum pressure vs time the influence zone is equal to 49.6 m while for the case in the absence of surcharge preloading, the influence zone decreased to 20.5 m.

Regarding the impact of magnitude of vacuum pressure on the influence zone it was shown that application of a stable high vacuum pressure can significantly reduce the diameter of the influence zone. It should be noted that like surcharge embankment, in the case of application of a constant 80 kPa vacuum pressure in residential complex the area of the influence zone propagates in the vicinity of the treatment area toward the center of the embankment and it is also creating danger for adjacent structures or infrastructures. Since vacuum pressure creates an inward displacement toward the center of embankment in contrast to surcharge embankment, a wise combination of surcharge and vacuum preloading might be a good option where there are sensitive infrastructures or structures if it be practically possible.

For every project that includes the treatment of weak clay or peat stratums, based on the material and sensitivity of nearby structures and infrastructures, the maximum allowable strains should be determined prior to designation of the treatment system to avoid unpredicted damage by qualified consultants. Finite element method is a powerful tool as shown in this article that can be utilized for modelling different and sophisticated scenarios.

5. References

[1] S. Horpibulsuk, N. Yangsukkaseam, A. Chinkulkijniwat, Y.J.J.A.C.S. Du, Compressibility and permeability of Bangkok clay compared with kaolinite and bentonite, 52(1-2) (2011) 150-159.

[2] S. Babaei, R. Amirabadi, M. Sharifi, Probabilistic Seismic Assessment and Fragility Curves for Fixed Pile-Founded Offshore Platforms %J International Journal Of Coastal, Offshore And Environmental Engineering, 7(1) (2022) 50-62.

[3] z. omrani, R. Amirabadi, M. Sharifi, Pile Length Optimization in Fixed Template Offshore Platform Using Risk Reduction Approach %J International Journal Of Coastal, Offshore And Environmental Engineering, 6(4) (2021) 33-43.

[4] D.C. Nguyen, N.M. Vu, H.J.J.o.M. Van Pham, E.S. Vol, Determination of the affected area of vacuum consolidation method for roadbed ground improvement to adjacent works, 61(6) (2020) 33-39.

[5] M. Tashiro, S.H. Nguyen, M. Inagaki, S. Yamada, T.J.S. Noda, Foundations, Simulation of large-scale deformation of ultra-soft peaty ground under test embankment loading and investigation of effective countermeasures against residual settlement and failure, 55(2) (2015) 343-358.

[6] J. Liu, H. Fu, J. Wang, Y. Cai, X.J.A.i.C.E. Hu, Estimation of influence scope of lateral displacement of soft ground under vacuum pressure with PVD, 2018 (2018).

[7] S. Chaiyaput, N. Sutti, T. Suksawat, J.J.B.o.E.G. Ayawanna, t. Environment, Electrical resistivity survey for evaluating the undrained shear strength of soft Bangkok clay at some of the canal-side road investigation sites, 81(1) (2022) 1-17.

[8] N. Koirala, S. Soralump, S.J.C.E. Phakdimek, Architecture, Observations from Ground Improvement Using Vacuum Consolidation Method, (2022) 771-783.

[9] M.M. Pardsouie, M.H. Pardsouie, S.M.A. Zomorodian, M.J.J.o.C.E. Mokhberi, M. Application, Numerical Study of efficiency of the Vacuum Preloading in Weak Clay Treatment (a case study), 6(2) (2022) 50-65.

[10] M.M. Pardsouie, M. Mokhberi, M.H.J.A.R.i.C.E. Pardsouie, The Importance of Incorporating Hydraulic Modifier Function versus Step Loading in Ground Improvements Including Vacuum Preloading, 4(2) (2022) 54-60.

[11] D. Bergado, A. Balasubramaniam, P. Long, Strength, compressibility and flow parameters for PVD improvement of soft Bangkok clay at SBIA project, in: Proceedings of the International Symposium on Geotechnical Aspects of the Second Bangkok International (Suvarnabhumi) Airport in Thailand. Southeast Asian Geotechnical Society (SEAGS), Bangkok, Thailand, 2006, pp. 43-66.

[12] C. Rujikiatkamjorn, B. Indraratna, Soft ground improvement by vacuum-assisted preloading, (2007).

[13] B. Indraratna, C. Rujikiatkamjorn, Predictions and Performances of Prefabricated Vertical Drain Stabilised Soft Clay Foundations, in, 2006.

[14] A. Asaoka, M. Nakano, T. Noda, K.J.S. Kaneda, Foundations, Delayed compression/consolidation of natural clay due to degradation of soil structure, 40(3) (2000) 75-85.

[15] T. Noda, A. Asaoka, M. Nakano, E. Yamada, M.J.S. Tashiro, Foundations, Progressive consolidation settlement of naturally deposited clayey soil under embankment loading, 45(5) (2005) 39-51.

[16] M.M. Fernandes, Consolidation theories and delayed settlements in clay, in: Analysis and design of geotechnical structures, CRC Press, 2020, pp. 167-228.

[17] J. Chai, C. Ong, J.P. Carter, D.T.J.G. Bergado, Lateral displacement under combined vacuum pressure and embankment loading, 63(10) (2013) 842-856.

[18] J. Chai, S.G.J.G. Rondonuwu, Geomembranes, Surcharge loading rate for minimizing lateral displacement of PVD improved deposit with vacuum pressure, 43(6) (2015) 558-566.

INTERNATIONAL JOURNAL OF
COASTAL, OFFSHORE & ENVIRONMENTAL ENGINEERING
IJCOE Vol.8/No. 2/Spring 2023 (21-39)

Available online at: www. Ijcoe.org

A New Look at the Vertical Shear of the Geostrophic Wind
Part II: Thermal Wind and Moist Wind

Mohammad Taghi Zamanian

Member of Iranian Society of Marine Science and Technology (ISMST); zamanianmohammadtaghi@gmail.com

ARTICLE INFO

Article History:
Received: 23 Oct. 2022
Accepted: 21 May. 2023

Keywords:
Baroclinic medium
Geostrophic wind
Dense wind
Thermal wind
Moist wind

ABSTRACT

We can divide atmosphere into two mediums, barotropic and baroclinic. Due to horizontal gradient of density, baroclinic medium causes to produce various horizontal gradient of pressure with respect to height and implies various horizontal velocities at different layers of the atmosphere. Therefore; geostrophic wind varies with respect to height in this medium.

The horizontal gradient of density not only would produce by horizontal gradient of temperature, but also by horizontal gradient of humidity or combination of both.

If horizontal gradient of density would be by both horizontal gradient of temperature and horizontal gradient of humidity – as they are existing in natural air – in the case; vectorial difference of geostrophic wind with respect to height is; *dense wind*.

If horizontal gradient of density is related to gradient of temperature solely; vectorial difference between geostrophic wind from top level and bottom level of the layer is; *thermal wind*.

And if horizontal gradient of density is solely related to gradient of specific humidity; vectorial difference between geostrophic wind from top level and bottom level of the layer is; *moist wind*.

The purpose of this paper is confirmation of three versions of dense wind, introduction five particular types of thermal wind and present two prominent types of moist wind in natural medium of air. Formulae related to each type are derived and every one of them, represents effects of one type of variation of geostrophic wind with respect to height.

1. Introduction

In part I of “*A New Look at the Vertical Shear of the Geostrophic Wind: Dense Wind*” we referred to some historical experiments about vertical shear of the geostrophic wind and number of basic ideas in connection with definition and deriving formulae to describe “*Dense Wind*”. [1]

We pointed out that various heat flux or humidity flux can lead to produce baroclinic atmosphere and in turn; variation of geostrophic wind in vertical direction. Furthermore, there is direct interaction between heat or humidity flux with wind shear.

In connection with the subject and as one feature of the role of heat flux to wind shear; Kim et. al. in their study through large-eddy simulation found out, that constant kinematic heat flux of 0.05 $\mathrm{Jm^{-2}s^{-1}}$causes for varying geostrophic wind speeds from 5 to $15\mathrm{ms^{-1}}$. Heat flux profiles show that the maximum entrainment heat flux as a fraction of the surface heat flux, increases from 0.13 to 0.30 in magnitude with increasing wind shear. The thickness of the entrainment layer, relative to the depth of the well-mixed layer, increases substantially from 0.36 to 0.73 with increasing wind shear. [2]

Now, some important points of part I are as follows:

1 – 1 – Vertical shear of the wind was research work of meteorologists in previous century. Among of them, we referred to works of Charnock et al. [3], Carlstead [4], Estoque [5] and Foster and Levy [6].

1 – 2 – Also we mentioned that all researchers those have been worked on the variation of geostrophic wind with respect to height, had two common ideas. They have been called difference between two geostrophic wind vectors at two pressure levels; the *thermal wind* as the first idea. In addition, they have been assumed the atmosphere is dry air, as a second idea.

Especially, this subject with same hypotheses, has been used in dynamic meteorology's text books, that is to say, in introducing of thermal wind, they assumed atmosphere is dry and derived formulae related to the subject in this case; although this assumption used for simplicity of the work. For instance, the subject is written in Hess's text book [7], Gill's text book [8], Dutton's text book [9], Holton and Hakim's text book [10] and in other dynamic meteorology text books. In addition; thermal wind has an entrée in *Glossary of Meteorology* [11] with the same descriptions. [1]

1 – 3 – Moreover, after some description of geostrophic wind in pressure coordinates system[1]; reason of variation of geostrophic wind with respect to height showed by logical argument and figure 1.

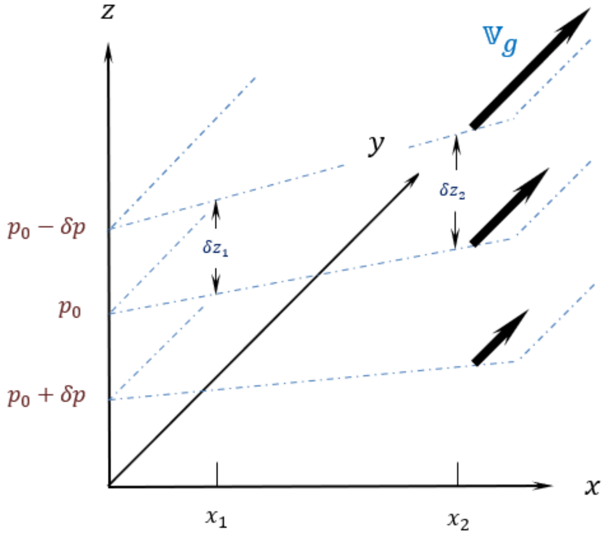

Figure 1. Relationship between vertical shear of the geostrophic wind and horizontal height gradients. (Note that $0 < \delta p$) [10]

Afterward; we defined "*Dense Wind*" as "*vectorial difference of geostrophic wind vector at upper level and geostrophic wind vector at lower level*" (of the atmospheric layer), that is:

$$\mathbb{v}_{\mathrm{D}} \equiv \mathbb{v}_{g(p_2)} - \mathbb{v}_{g(p_1)} \tag{1-D}$$

where in Equation (1) $\mathbb{v}_{\mathrm{D}}$ stands for dense wind vector, $\mathbb{v}_g$ is geostrophic wind, and subscripts p_1 and p_2 refer to pressure levels in the manner that level p_2 has more height than level p_1, i.e., $p_2 < p_1$.

According to definition (1); eastward and northward components of dense wind can be shown as following:

$$u_{\mathrm{D}} = u_{g(p_2)} - u_{g(p_1)} \tag{2-D-a}$$

and

$$v_{\mathrm{D}} = v_{g(p_2)} - v_{g(p_1)} \tag{2-D-b}$$

where u_{D} is eastward component of dense wind, u_g is eastward component of geostrophic wind, v_{D} is northward component of dense wind, v_g is northward component of geostrophic wind and subscripts p_1 and p_2 refer to pressure levels in the manner that level p_2 has more height than level p_1, i.e., $p_2 < p_1$.

Typical layer of atmospheric system is shown in figure 2.

Despite its name, dense wind, while a vector, is not a true wind. Instead, it is a geostrophic wind shear, representing the change of wind with respect to height, causing some advections. [1]

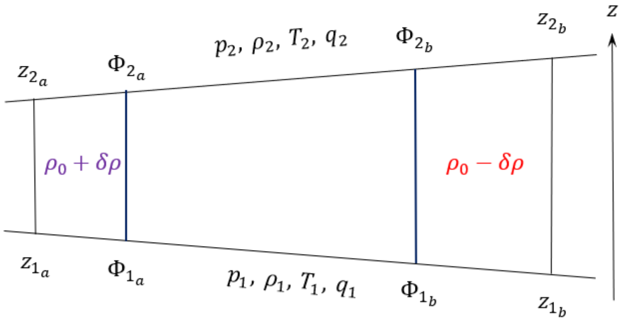

Figure 2. Typical layer of atmospheric system.

1 – 4 – Furthermore, with using a number of formulae from a few text books same as Curry and Webster [12], Iribarne and Godson [13] and Haltiner and Williams [14]; we derived three versions of dense wind's equations, vectors and components. [1]

1 – 5 – For the first version of dense wind; dense wind equation is:

$$\frac{\partial \mathbb{v}_g}{\partial p} = \frac{1}{f(\rho_{\mathrm{M}})^2}\left(\mathbb{k}_p \times \nabla_p \rho_{\mathrm{M}}\right) \tag{3-D-I}$$

and first version of dense wind vector is:

$$\mathbb{v}_{\mathrm{D_I}} = \frac{1}{f}\int_{p_1}^{p_2}\left[\frac{1}{(\rho_{\mathrm{M}})^2}\left(\mathbb{k}_p \times \nabla_p \rho_{\mathrm{M}}\right)\right] dp \tag{4-D-I}$$

where in equations (3-D-I) and (4-D-I), $\mathbb{v}_g$ is geostrophic wind, p is pressure, f is Coriolis parameter, ρ_{M} stands for density of humid air, $\mathbb{k}_p$ is vertical unit vector in pressure coordinates system, ∇_p is gradient operator in pressure coordinates system, $\mathbb{v}_{\mathrm{D_I}}$ stands for first version of dense wind vector, p_1 is atmospheric pressure at lower level of the atmospheric layer and p_2 is atmospheric pressure at upper level of the atmospheric layer.

Eastward and northward components of first version of dense wind can be derived from equation (4-D-I) directly:

$$u_{\mathrm{D_I}} = -\frac{1}{f}\int_{p_1}^{p_2}\left(\frac{1}{(\rho_{\mathrm{M}})^2}\frac{\partial \rho_{\mathrm{M}}}{\partial y}\right) dp \tag{5-D-I-a}$$

---

[1] In the part I and in this paper (part II); whenever we refer to *"pressure coordinates system"* our purpose is "*Cartesian coordinates system with pressure as vertical coordinate".* Note this coordinates system is "*Left-handed system*".

and

$$v_{\mathrm{D_I}} = \frac{1}{f}\int_{p_1}^{p_2}\left(\frac{1}{(\rho_{\mathrm{M}})^2}\frac{\partial \rho_{\mathrm{M}}}{\partial x}\right)dp \qquad \text{(5-D-I-b)}$$

where in equation (5-D-I-a) $u_{\mathrm{D_I}}$ is eastward component of first version of dense wind and y is northward axis of pressure coordinates system. In addition; in equation (5-D-I-b) $v_{\mathrm{D_I}}$ stands for northward component of first version of dense wind and x is eastward axis of pressure coordinates system.

In this case; clockwise rotation of geostrophic wind with respect to height, associated with light air advection and counterclockwise turning of geostrophic wind with respect to height connected with dense air advection. [1]

1 – 6 – For the second version of dense wind; dense wind equation is:

$$\frac{\partial \mathbb{v}_g}{\partial \ln p} = -\frac{R_d}{f}\left(\mathbb{k}_p \times \nabla_p T_v\right) \qquad \text{(3-D-II)}$$

and second version of dense wind vector is:

$$\mathbb{v}_{\mathrm{D_{II}}} = -\frac{R_d}{f}\int_{p_1}^{p_2}\left(\mathbb{k}_p \times \nabla_p T_v\right)d\ln p \qquad \text{(4-D-II)}$$

where in equations (3-D-II) and (4-D-II); R_d is gas constant for dry air, T_v stand for virtual temperature, $\mathbb{v}_{\mathrm{D_{II}}}$ is second version of dense wind vector and other symbols are defined under 1 – 5.

Eastward and northward components of second version of dense wind can be derived from equation (4-D-II) directly as follows:

$$u_{\mathrm{D_{II}}} = \frac{R_d}{f}\int_{p_1}^{p_2}\frac{\partial T_{\mathrm{v}}}{\partial y}d\ln p \qquad \text{(5-D-II-a)}$$

and

$$v_{\mathrm{D_{II}}} = -\frac{R_d}{f}\int_{p_1}^{p_2}\frac{\partial T_{\mathrm{v}}}{\partial x}d\ln p \qquad \text{(5-D-II-b)}$$

where in equation (5-D-II-a), $u_{\mathrm{D_{II}}}$ is eastward component of second version of dense wind, y is northward axis in pressure coordinates system and in equation (5-D-II-b), $v_{\mathrm{D_{II}}}$ is northward component of second version of dense wind and x is eastward axis of pressure coordinates system. In the case of second version of dense wind; clockwise rotation of geostrophic wind with respect to height, associated with warmer or more humid air advection and counterclockwise turning of geostrophic wind with respect to height connected with colder or less humid air advection. [1]

1 – 7 – For the third version of dense wind; dense wind equation is:

$$\frac{\partial \mathbb{v}_g}{\partial p} = \frac{1}{f}\mathbb{k}_p \times \nabla_p\left(\frac{\partial \Phi}{\partial p}\right) \qquad \text{(3-D-III)}$$

and third version of dense wind vector is:

$$\mathbb{v}_{\mathrm{D_{III}}} = \frac{1}{f}\mathbb{k}_p \times \nabla_p(\Phi_2 - \Phi_1) \qquad \text{(4-D-III)}$$

where in equation (3-D-III) Φ is geopotential and in equation (4-D-III) $\mathbb{v}_{\mathrm{D_{III}}}$ stands for third version of dense wind vector, Φ_2 refers to geopotential of upper level and Φ_1 points to geopotential of lower level of the atmospheric layer and other symbols are defined under 1 – 5.

Eastward and northward components of third version of dense wind can be derived from equation (4-D-III) directly as follows:

$$u_{\mathrm{D_{III}}} = -\frac{1}{f}\frac{\partial}{\partial y}(\Phi_2 - \Phi_1) \qquad \text{(5-D-III-a)}$$

and

$$v_{\mathrm{D_{III}}} = \frac{1}{f}\frac{\partial}{\partial x}(\Phi_2 - \Phi_1) \qquad \text{(5-D-III-a)}$$

where in equation (5-D-III-a), $u_{\mathrm{D_{III}}}$ is eastward component of third version of dense wind, y is northward axis in pressure coordinates system and in equation (5-D-III-b), $v_{\mathrm{D_{III}}}$ is northward component of third version of dense wind and x is eastward axis of pressure coordinates system. Finally, in the case of third version of dense wind; clockwise rotation of geostrophic wind with respect to height, associated with advection of atmospheric thicker layer and counterclockwise turning of geostrophic wind with respect to height connected with advection of less thickness layer of atmosphere. [1]

Following part I; in this part; we focus on special cases of dense wind.

2. Special cases of Dense Wind

In part I of "*A New Look at the Vertical Shear of Geostrophic Wind: Dense Wind*" we referred to virtual temperature as follows:

$$T_v = (1 + 0.608q)T \qquad \text{(6)}$$

where in equation (6) q is specific humidity and T stands for temperature. [12]

Choosing equivalent of T_v from equation (6) and substituting into equation (4-D-II) yields:

$$\mathbb{v}_{\mathrm{D_{II}}} = -\frac{R_d}{f}\int_{p_1}^{p_2}\left[\mathbb{k}_p \times \nabla_p(1 + 0.608q)T\right]d\ln p \qquad \text{(7-D-II)}$$

Equation (7-D-II) is dense wind vector in terms of gas constant for dry air, Coriolis parameter, pressures of below and upper levels of atmospheric layer, unit vector of vertical axis of pressure coordinates system, specific humidity of air, air temperature and logarithm of air pressure.

Now, we consider equation (5-D-II-a), i.e.:

$$u_{\mathrm{D_{II}}} = \frac{R_d}{f}\int_{p_1}^{p_2}\frac{\partial T_{\mathrm{v}}}{\partial y}d\ln p \qquad \text{(5-D-II-a)}$$

First of all, we do integration on equation (5-D-II-a):

$$u_{\mathrm{D_{II}}} = \frac{R_d}{f}\frac{\partial\langle T_{\mathrm{v}}\rangle}{\partial y}\ln\left(\frac{p_2}{p_1}\right) \tag{8}$$

where in equation (8), $\langle ... \rangle$ refers to vertical average of phrase or parameter in the layer enclosed by p_1 and p_2 pressure levels.[2]

If we select equivalent of T_v from equation (6), insert into equation (8) and applying derivation, yields:

$$u_{\mathrm{D_{II}}} = \frac{R_d}{f}\left[\left(\begin{array}{c} 0.608\,\frac{\partial\langle q\rangle}{\partial y}\langle T\rangle + \\ (1+0.608\langle q\rangle)\,\frac{\partial\langle T\rangle}{\partial y}\end{array}\right)\right]\ln\left(\frac{p_2}{p_1}\right) \tag{9-D-II-a}$$

And with the same manner, one can find out from equation (5-D-II-b):

$$v_{\mathrm{D_{II}}} = -\frac{R_d}{f}\left[\left(\begin{array}{c} 0.608\,\frac{\partial\langle q\rangle}{\partial x}\langle T\rangle + \\ (1+0.608\langle q\rangle)\,\frac{\partial\langle T\rangle}{\partial x}\end{array}\right)\right]\ln\left(\frac{p_2}{p_1}\right) \tag{9-D-II-b}$$

Equations (9-D-II-a) and (9-D-II-b) show component equations of second version of dense wind, in terms of gas constant for dry air, Coriolis parameter, specific humidity, temperature and pressure. In addition; symbol $\langle ... \rangle$ refers to vertical average of phrase or parameter in the layer enclosed by p_1 and p_2 pressure levels.

And, as we noticed in part I; our aim in this research is, looking for geostrophic wind shear in the condition of real atmosphere.

However, a question that arises from the above-mentioned paragraph is; if we consider atmosphere as natural atmosphere including humidity; then how the looking to variation of the wind in vertical direction should be modify? In this research, the variation of the geostrophic wind with respect to height will be considered in the natural atmosphere, as well as dry air.

2.1. First special case of dense wind: Thermal wind

If the air would be assumed dry[3], i.e.:

$$q = 0 \tag{10}$$

or air is humid but specific humidity is constant[4] that is:

$$q = constant \tag{11}$$

or horizontal gradient of vertical mean for specific humidity in the atmospheric layer may be zero[5], so that:

$$\left[\frac{\partial\langle q\rangle}{\partial x} = 0 \text{ and } \frac{\partial\langle q\rangle}{\partial y} = 0\right] \text{ but } \frac{\partial q}{\partial p} \neq 0 \tag{12}$$

In these conditions; the variation of density in the horizontal direction is merely related to variation of temperature in horizontal direction causing baroclinity[6] of the atmosphere. In these circumstances; we define the vectorial difference of geostrophic wind vector at upper level and geostrophic wind vector at lower level of the atmospheric layer as, *thermal wind*, i.e.:

$$\mathbb{v}_{\mathrm{T}} \equiv \mathbb{v}_{g(p_2)} - \mathbb{v}_{g(p_1)} \tag{1-T}$$

where in Equation (1-T) $\mathbb{v}_{\mathrm{T}}$ stands for thermal wind vector, $\mathbb{v}_g$ is geostrophic wind and subscripts p_1 and p_2 refer to pressure levels in the manner that level p_2 has more height than level p_1, i.e., $p_2 < p_1$.

According to definition (1-T); eastward and northward components of thermal wind can be shown as following:

$$u_{\mathrm{T}} = u_{g(p_2)} - u_{g(p_1)} \tag{2-T-a}$$

and

$$v_{\mathrm{T}} = v_{g(p_2)} - v_{g(p_1)} \tag{2-T-b}$$

where in equations (2-T-a) and (2-T-b) u_{T} is eastward component of thermal wind, v_{T} is northward component of thermal wind, u_g is eastward component of geostrophic wind, v_g is northward component of geostrophic wind and subscripts p_1 and p_2 refer to pressure levels in the manner that level p_2 has more height than level p_1, i.e., $p_2 < p_1$.

Approaching to derive thermal wind has two branches. 1 – Temperature branch and 2 – Geopotential branch.

2.1.1 Thermal wind; Approach by Temperature

Approaching thermal wind by temperature has three particular types those will describe in following parts.

2.1.1.1 First particular type of the thermal wind

Now, we assume that air is dry by taking $q = 0$. Geostrophic wind can be introduced by:

$$\mathbb{v}_g = f^{-1}\mathbb{k}_p \times \nabla_p\Phi \tag{13}$$

---

[2] For more details of "*Vertical averaging*" see [1]

[3] This case is not real, and assumption is for simplicity of deriving formulae of special cases of dense wind.

[4] Existence of this condition is possible for air over ocean especially at nights.

[5] This case can be occurred in tropic regions in the dry season. Also; it is possible to be the case at the surface of oceans in mid-latitude in days, upon conditions that: a) low difference between two latitudes and b) no existence of atmospheric system. However, this idea should be tested with observations.

[6] Baroclinity is the state of baroclinic atmosphere or baroclinic ocean. That state is existence of horizontal variation of density and is described in part I of "*A New Look at the Vertical Shear of the Geostrophic Wind*"

where in equation (13) $\mathbb{v}_g$ is geostrophic wind vector, f is Coriolis parameter, $\mathbb{k}$ is vertical unit vector, subscript p shows that equation (13) is written in pressure coordinates system, ∇ is operator for gradient, Φ is geopotential and again, subscript p shows that coordinates system is pressure coordinates system.

Furthermore, equation (13) shows the magnitude of geostrophic wind is proportional to the horizontal gradient of geopotential and is parallel to equipotential lines on isobaric surface. [10]

Writing eastward and northward components of geostrophic wind yields following equations:

$$u_g = -\frac{1}{f}\frac{\partial \Phi}{\partial y} \qquad (14\text{-a})$$

and

$$v_g = \frac{1}{f}\frac{\partial \Phi}{\partial x} \qquad (14\text{-b})$$

where in equation (14-a) u_g is eastward component of geostrophic wind or eastward component of geostrophic current in ocean, and in equation (14-b) v_g is northward component of geostrophic wind or northward component of geostrophic current in ocean.

Now, if we differentiate equations (14-a) and (14-b) with respect to p, we get:

$$\frac{\partial u_g}{\partial p} = -\frac{1}{f}\frac{\partial}{\partial p}\left(\frac{\partial \Phi}{\partial y}\right) = -\frac{1}{f}\frac{\partial}{\partial y}\left(\frac{\partial \Phi}{\partial p}\right) \qquad (15\text{-a})$$

and

$$\frac{\partial v_g}{\partial p} = \frac{1}{f}\frac{\partial}{\partial p}\left(\frac{\partial \Phi}{\partial x}\right) = \frac{1}{f}\frac{\partial}{\partial x}\left(\frac{\partial \Phi}{\partial p}\right) \qquad (15\text{-b})$$

The equation of state for dry air is: [10]

$$p = \rho R_d T \qquad (16)$$

where in equation (16), p is pressure, ρ is dry air density, R_d is gas constant for dry air and T is its temperature. In pressure coordinates system; hydrostatic equation, applying for dry air and considering the equation of state for dry air, i.e., equation (16); is [13]:

$$\frac{\partial \Phi}{\partial p} = -\alpha = -\frac{1}{\rho} = -\frac{R_d T}{p} \qquad (17)$$

where α is specific volume of dry air.

If we select equivalent of $\frac{\partial \Phi}{\partial p}$ from equation (17) that is $-\frac{R_d T}{p}$ and substitute in equations (15-a) and (15-b), we get:

$$\frac{\partial u_g}{\partial p} = -\frac{1}{f}\frac{\partial}{\partial y}\left(-\frac{R_d T}{p}\right) \qquad (18\text{-a})$$

and

$$\frac{\partial v_g}{\partial p} = \frac{1}{f}\frac{\partial}{\partial x}\left(-\frac{R_d T}{p}\right) \qquad (18\text{-b})$$

Rearranging equations (18-a) and (18-b) will be:

$$p\frac{\partial u_g}{\partial p} \equiv \frac{\partial u_g}{\partial \ln p} = \frac{R_d}{f}\left(\frac{\partial T}{\partial y}\right)_p \qquad (19\text{-T-I-a})$$

and

$$p\frac{\partial v_g}{\partial p} \equiv \frac{\partial v_g}{\partial \ln p} = -\frac{R_d}{f}\left(\frac{\partial T}{\partial x}\right)_p \qquad (19\text{-T-I-b})$$

where in equations (19-T-I-a) and (19-T-I-b) subscript p points that derivative is down with constant p. If we compound equations (19-T-I-a) and (19-T-I-b), we get "*Thermal wind equation by first particular type*" that is:

$$\frac{\partial \mathbb{v}_g}{\partial \ln p} = -\frac{R_d}{f}\left(\mathbb{k}_p \times \nabla_p T\right) \qquad (3\text{-T-I})$$

By integrating of equation (3-T-I) from lower pressure level p_1 to upper pressure level p_2 $(p_2 < p_1)$ of the atmospheric layer; one can derive "*First particular type of thermal wind vector*":

$$\mathbb{v}_{g(p_2)} - \mathbb{v}_{g(p_1)} \equiv \mathbb{v}_{\mathrm{T_I}} = -\frac{R_d}{f}\int_{p_1}^{p_2}\left(\mathbb{k}_p \times \nabla_p T\right) d\ln p \qquad (4\text{-T-I})$$

where in equation (4-T-I); $\mathbb{v}_{g(p_2)}$ is geostrophic wind vector at upper level of the atmospheric layer, $\mathbb{v}_{g(p_1)}$ is geostrophic wind vector at lower level of the atmospheric layer, $\mathbb{v}_{\mathrm{T_I}}$ stands for first particular type of thermal wind vector, R_d is gas constant for dry air, f is Coriolis parameter, p_1 is atmospheric pressure at lower level of the atmospheric layer, p_2 is atmospheric pressure at upper level of the atmospheric layer, $\mathbb{k}_p$ is vertical unit vector in pressure coordinates system, ∇_p stands for gradient operator in pressure coordinates system, T is dry air temperature and p is atmospheric pressure and vertical axis of pressure coordinates system.

Eastward and northward components of the first particular type of thermal wind can be derived by vertical integration of equations (19-T-I-a) and (19-T-I-b) in vertical coordinate same as integration of equation (3-T-I), or determine the eastward and northward components of the first particular type of thermal wind from equation (4-T-I) directly:

$$u_{\mathrm{T_I}} = \frac{R_d}{f}\int_{p_1}^{p_2}\frac{\partial T}{\partial y}\, d\ln p \qquad (5\text{-T-I-a})$$

and

$$v_{\mathrm{T_I}} = -\frac{R_d}{f}\int_{p_1}^{p_2}\frac{\partial T}{\partial x}\, d\ln p \qquad (5\text{-T-I-b})$$

where in equation (5-T-I-a), $u_{\mathrm{T_I}}$ is eastward component of first particular type of thermal wind and in equation (5-T-I-b), $v_{\mathrm{T_I}}$ is northward component of first particular type of thermal wind.

From first particular type of thermal wind vector or its components; one can find out that:

A: If we go from pole to equator, thermal wind becomes stronger[7];
B: If the horizontal gradient of temperature would be greater, thermal wind becomes stronger, because thermal wind is proportional to the horizontal gradient of temperature, and finally;
C: If the pressure difference will be higher in the layer, thermal wind becomes more powerful.
In this manner; representative of thermal wind vector, i.e., equation (4-T-I) shows that: "*thermal wind blows parallel to isotherms, so that, warm dry air is located at the right side of downwind and cold dry air is located at the left side of downwind.*" (In the northern hemisphere) This fact is illustrated in figures 3 and 4.

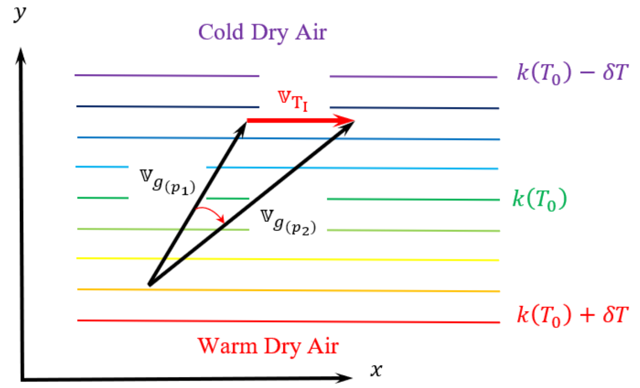

Figure 3. Relationship between clockwise turning of the geostrophic wind with respect to height (veering) and warm dry air advection. In the case; T_0 is mean temperature of the layer and proportion coefficient k is: $k = -\frac{R_d}{f}\ln\left(\frac{p_2}{p_1}\right)$

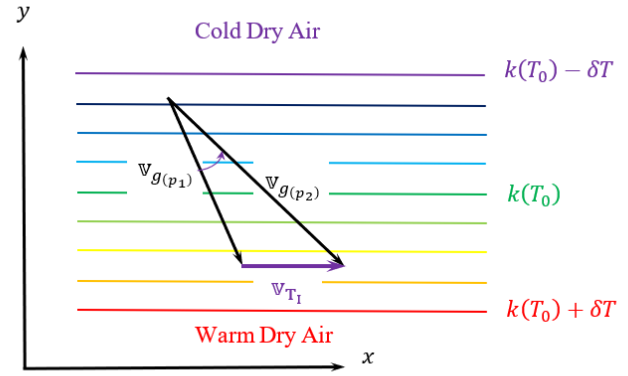

Figure 4. Relationship between counterclockwise turning of the geostrophic wind with respect to height (backing) and cold dry air advection. In the case; T_0 is mean temperature of the layer and proportion coefficient k is: $k = -\frac{R_d}{f}\ln\left(\frac{p_2}{p_1}\right)$

As it is shown in figure 3; in the dry atmosphere, in which specific humidity is zero; a geostrophic wind that turns clockwise with respect to height (veering) is associated with warm dry air advection. Conversely, as shown in figure 4; in the above-mentioned air, counterclockwise turning (backing) of the geostrophic wind with respect to height, implies cold dry air advection by the geostrophic wind in the layer.
It is therefore possible to obtain a reasonable estimate of the horizontal temperature advection and its vertical dependence at a given location solely from data on the vertical profile of the wind given by a single sounding. Alternatively, the geostrophic wind at any level can be estimated from the mean temperature field provided that the geostrophic velocity is known at a single level. Thus, for example, if the geostrophic wind at 850 hPa is known and the mean horizontal temperature gradient in the layer 850 – 500 hPa is also known, the first particular type of thermal wind equation can be applied to obtain the geostrophic wind at 500 hPa [10]
First particular type of thermal wind vector, i.e., equation (4-T-I) has a simple form by integration with respect to vertical axis, as following:

$$\mathbb{v}_{T_I} = -\frac{R_d}{f}\langle \mathbb{k}_p \times \nabla_p T\rangle \ln\left(\frac{p_2}{p_1}\right) \qquad \text{(20-T-I)}$$

Also, equation (20-T-I) can be written in simpler form as:

$$\mathbb{v}_{T_I} = -\frac{R_d}{f}\left(\mathbb{k}_p \times \nabla_p \langle T\rangle\right) \ln\left(\frac{p_2}{p_1}\right) \qquad \text{(21-T-I)}$$

In equations (20-T-I) and (21-T-I), $\langle\ldots\rangle$ is vertical average of phrase or parameter.
Analogous to integration of equation (4-T-I); we can obtain simple form of equations (5-T-I-a) and (5-T-I-b) those show simple forms for components of first particular type of thermal wind vector for dry air; those are:

$$u_{T_I} = \frac{R_d}{f}\frac{\partial\langle T\rangle}{\partial y}\ln\left(\frac{p_2}{p_1}\right) \qquad \text{(22-T-I-a)}$$

and

$$v_{T_I} = -\frac{R_d}{f}\frac{\partial\langle T\rangle}{\partial x}\ln\left(\frac{p_2}{p_1}\right) \qquad \text{(22-T-I-b)}$$

Again, in equations (22-T-I-a) and (22-T-I-b), $\langle\ldots\rangle$ is vertical averaging of phrase or parameter and furthermore, in equation (22-T-I-a) u_{T_I} is eastward component of thermal wind by first particular type and in equation (22-T-I-b) v_{T_I} is northward component of first particular type of thermal wind.
There is another method to derive first particular type of thermal wind; that at the moment, we don't refer to it.

2.1.1.2 Second particular type of the thermal wind

In this condition that air is humid but humidity of atmosphere is constant, i.e., $q = constant$; and of course, the variation of density in the horizontal direction is merely related to variation of temperature

---

[7] Use of geostrophic wind in tropical regions must be with careful deliberation because geostrophic wind in these regions is magnified and especially on equator is meaningless.

in horizontal direction and causes to produce baroclinic atmosphere. In the case, we define the vectorial difference of geostrophic wind vector at upper level and geostrophic wind vector at lower level of the atmospheric layer as, *thermal wind* again, i.e.:

$$\mathbb{v}_{\mathrm{T}} \equiv \mathbb{v}_{g(p_2)} - \mathbb{v}_{g(p_1)} \tag{1-T}$$

And according to definition (1-T); eastward and northward components of thermal wind can be shown as following:

$$u_{\mathrm{T}} = u_{g(p_2)} - u_{g(p_1)} \tag{2-T-a}$$

and

$$v_{\mathrm{T}} = v_{g(p_2)} - v_{g(p_1)} \tag{2-T-b}$$

The equation of state for humid or moist air can be written as: [1]

$$p = \rho_{\mathrm{M}} R_d T_v \tag{23}$$

Where p is pressure, ρ_{M} is density of humid air, R_d is gas constant for dry air and T_v is virtual temperature.

In pressure coordinates system, hydrostatic equation, applying for humid air and considering the equation of state; is [13]:

$$\frac{\partial\Phi}{\partial p} = -\alpha_{\mathrm{M}} = -\frac{R_d T_v}{p} \tag{24}$$

where in equation (24), Φ is geopotential, p is pressure as vertical coordinate, α_{M} is specific volume of humid air, R_d is constant gas for dry air and T_v is virtual temperature.

If we select equivalent of $\frac{\partial\Phi}{\partial p}$ from equation (24) that is $-\frac{R_d T_v}{p}$ and substitute in equations (15-a) and (15-b), we get:

$$\frac{\partial u_g}{\partial p} = -\frac{1}{f}\frac{\partial}{\partial y}\left(-\frac{R_d T_v}{p}\right) \tag{25-a}$$

and

$$\frac{\partial v_g}{\partial p} = \frac{1}{f}\frac{\partial}{\partial x}\left(-\frac{R_d T_v}{p}\right) \tag{25-b}$$

or

$$p\frac{\partial u_g}{\partial p} = \frac{R_d}{f}\left(\frac{\partial T_v}{\partial y}\right)_p \tag{26-a}$$

and

$$p\frac{\partial v_g}{\partial p} = -\frac{R_d}{f}\left(\frac{\partial T_v}{\partial x}\right)_p \tag{26-b}$$

where in equations (26-a) and (26-b) subscript p points that derivative is down with constant p.

Considering equations (26-a) and (26-b) and substitute equivalent of T_v form equation (6) into these equations yields:

$$p\frac{\partial u_g}{\partial p} = \frac{R_d}{f}\left[\frac{\partial(1+0.608q)T}{\partial y}\right]_p \tag{27-a}$$

and

$$p\frac{\partial v_g}{\partial p} = -\frac{R_d}{f}\left[\frac{\partial(1+0.608q)T}{\partial x}\right]_p \tag{27-b}$$

or

$$\frac{\partial u_g}{\partial \ln p} = \frac{R_d}{f}\left[\frac{\partial(1+0.608q)T}{\partial y}\right]_p \tag{28-a}$$

and

$$\frac{\partial v_g}{\partial \ln p} = -\frac{R_d}{f}\left[\frac{\partial(1+0.608q)T}{\partial x}\right]_p \tag{28-b}$$

By considering condition (11), i.e., $q = constant$, we can rewrite equations (28-a) and (28-b) as following:

$$\frac{\partial u_g}{\partial \ln p} = (1+0.608q)\frac{R_d}{f}\left(\frac{\partial T}{\partial y}\right)_p \tag{19-T-II-a}$$

and

$$\frac{\partial v_g}{\partial \ln p} = -(1+0.608q)\frac{R_d}{f}\left(\frac{\partial T}{\partial x}\right)_p \tag{19-T-II-b}$$

Equations (19-T-II-a) and (19-T-II-b) can be combined as vector form:

$$\frac{\partial \mathbb{v}_g}{\partial \ln p} = -(1+0.608q)\frac{R_d}{f}\left(\mathbb{k}_p \times \nabla_p T\right) \tag{3-T-II}$$

Equation (3-T-II) is "*Second particular type of thermal wind equation*".

By integration of equation (3-T-II) from lower pressure level p_1 to upper pressure level p_2, $(p_2 < p_1)$ of the atmospheric layer; one can derive "*Second particular type of thermal wind vector*" that is:

$$\mathbb{v}_{g(p_2)} - \mathbb{v}_{g(p_1)} \equiv \mathbb{v}_{\mathrm{T_{II}}} = -(1+0.608q)\frac{R_d}{f}\int_{p_1}^{p_2}\left(\mathbb{k}_p \times \nabla_p T\right) d\ln p \tag{4-T-II}$$

where in equation (4-T-II); $\mathbb{v}_{g(p_2)}$ is geostrophic wind vector at upper level of the atmospheric layer, $\mathbb{v}_{g(p_1)}$ is geostrophic wind vector at lower level of the atmospheric layer with constant specific humidity, $\mathbb{v}_{\mathrm{T_{II}}}$ stands for second particular type of thermal wind vector, q is specific humidity, R_d is gas constant for dry air, f is Coriolis parameter, p_1 is atmospheric pressure at lower level of the atmospheric layer, p_2 is atmospheric pressure at upper level of the atmospheric layer, $\mathbb{k}_p$ is vertical unit vector in pressure coordinates system, ∇_p stands for gradient operator in pressure coordinates system, T is air temperature and p is atmospheric pressure and vertical axis of pressure coordinates system.

Eastward and northward components of second particular type of thermal wind can be derived by vertical integration of equations (30-T-II-a) and (30-T-II-b) same as integration of equation (3-T-II), or determine the eastward and northward components of second particular type of thermal wind from equation (4-T-II) directly:

$$\int_{p_1}^{p_2} du_g = (1+0.608q)\frac{R_d}{f}\int_{p_1}^{p_2}\left(\frac{\partial T}{\partial y}\right) d\ln p \qquad \text{(29-a)}$$

and

$$\int_{p_1}^{p_2} dv_g = -(1+0.608q)\frac{R_d}{f}\int_{p_1}^{p_2}\frac{\partial T}{\partial x}\, d\ln p \qquad \text{(29-b)}$$

And after doing integration to left hand on both above mentioned equations, we get:

$$u_{g(p_2)} - u_{g(p_1)} \equiv$$
$$u_{\mathrm{T_{II}}} = (1+0.608q)\frac{R_d}{f}\int_{p_1}^{p_2}\left(\frac{\partial T}{\partial y}\right) d\ln p \qquad \text{(5-T-II-a)}$$

and

$$v_{g(p_2)} - v_{g(p_1)} \equiv$$
$$v_{\mathrm{T_{II}}} = -(1+0.608q)\frac{R_d}{f}\int_{p_1}^{p_2}\left(\frac{\partial T}{\partial x}\right) d\ln p \qquad \text{(5-T-II-b)}$$

where in equation (5-T-II-a), $u_{\mathrm{T_{II}}}$ is eastward component of the second particular type of thermal wind, and in equation (5-T-II-b), $v_{\mathrm{T_{II}}}$ is northward component of the second particular type of thermal wind.

From second particular type of thermal wind vector or its components; one can find out that:

A: If we go from pole to equator, thermal wind becomes stronger (with pay attention to footnote No. 7);

B: If the horizontal gradient of temperature would be greater, thermal wind becomes stronger, because thermal wind is proportional to the horizontal gradient of temperature;

C: If the pressure difference will be higher in the layer, thermal wind becomes more powerful, and finally;

D: If humid air has more specific humidity, then thermal wind will be stronger.

In this manner; representative of second particular type of thermal wind vector, i.e., equation (4-T-II) shows that: "*thermal wind blows parallel to isotherms, so that, warm humid air is located at the right side of downwind and cold humid air is located at the left side of downwind.*" (In the northern hemisphere) This fact is illustrated in figures 5 and 6.

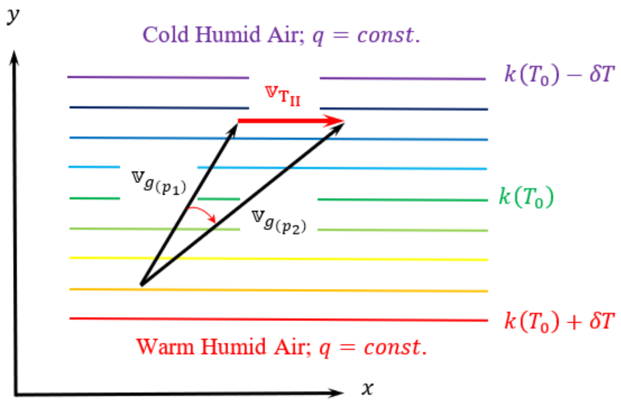

Figure 5. Relationship between clockwise turning of the geostrophic wind with respect to height (veering) and warm humid air advection. In the case; T_0 is mean temperature of the layer and proportion coefficient k is:

$$\boldsymbol{k = -(1+0.608q)\frac{R_d}{f}\ln\left(\frac{p_2}{p_1}\right)}$$

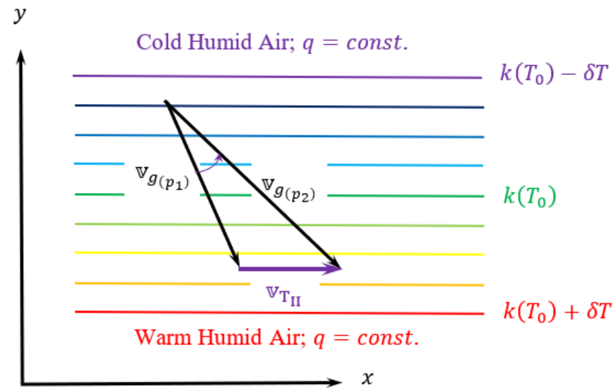

Figure 6. Relationship between counterclockwise turning of the geostrophic wind with respect to height (backing) and cold humid air advection. In the case; T_0 is mean temperature of the layer and proportion coefficient k is:

$$\boldsymbol{k = -(1+0.608q)\frac{R_d}{f}\ln\left(\frac{p_2}{p_1}\right)}$$

As it is shown in figure 5; in the humid atmosphere with constant specific humidity; a geostrophic wind that turns clockwise with respect to height (veering) is associated with warm humid air advection. Conversely, as shown in figure 6; in the above-mentioned air, counterclockwise turning (backing) of the geostrophic wind with respect to height, implies cold humid air advection by the geostrophic wind in the atmospheric layer.

Moreover, for second particular type of thermal wind; conditions those were mentioned under first particular type of thermal wind for obtaining horizontal warm humid air advection, cold humid air advection, mean temperature field or geostrophic wind at one level of the atmospheric layer with humid air, by knowing other parameters are true.

Second particular type of thermal wind vector, i.e., equation (4-T-II) has a simple form by integration with respect to vertical axis, as following:

$$\mathbb{v}_{\mathrm{T}_{\mathrm{II}}} = -(1+0.608q)\frac{R_d}{f}\langle \mathbb{k}_p \times \nabla_p T\rangle \ln\left(\frac{p_2}{p_1}\right) \tag{20-T-II}$$

Also, equation (20--T-II) can be written in simpler form as:

$$\mathbb{v}_{\mathrm{T}_{\mathrm{II}}} = -(1+0.608q)\frac{R_d}{f}\left(\mathbb{k}_p \times \nabla_p \langle T\rangle\right) \ln\left(\frac{p_2}{p_1}\right) \tag{21-T-II}$$

where in equations (20-T-II) and (21-T-II), $\langle \dots \rangle$ is vertical averaging of phrase or parameter.

Analogous to integration of equation (4-T-II); we can obtain simple form of equations (5-T-II-a) and (5-T-II-b) those show simple forms for components of second particular type of thermal wind vector for humid air with constant specific humidity; those are:

$$u_{\mathrm{T}_{\mathrm{II}}} = (1+0.608q)\frac{R_d}{f}\frac{\partial\langle T\rangle}{\partial y}\ln\left(\frac{p_2}{p_1}\right) \tag{22-T-II-a}$$

and

$$v_{\mathrm{T}_{\mathrm{II}}} = -(1+0.608q)\frac{R_d}{f}\frac{\partial\langle T\rangle}{\partial x}\ln\left(\frac{p_2}{p_1}\right) \tag{22-T-II-b}$$

Again, in equations (22-T-II-a) and (22-T-II-b), $\langle \dots \rangle$ is vertical averaging of phrase or parameter and furthermore, in equation (22-T-II-a) $u_{\mathrm{T}_{\mathrm{II}}}$ is eastward component of thermal wind by second particular type and in equation (22-T-II-b) $v_{\mathrm{T}_{\mathrm{II}}}$ is northward component of thermal wind in second particular type.

There is another method to derive second particular type of thermal wind; that at the moment, we don’t refer to it.

2.1.1.3 Third particular type of the thermal wind

In this case; air has humidity but we assume that horizontal gradient of vertical average of specific humidity in the atmospheric layer may be zero but specific humidity varies in vertical direction, so that:

$$\left[\frac{\partial\langle q\rangle}{\partial x} = 0 \ \text{ and } \ \frac{\partial\langle q\rangle}{\partial y} = 0\right] \ \text{ but } \ \frac{\partial q}{\partial p} \neq 0 \tag{12}$$

And in this case, atmosphere medium is very similar to barotropic medium, where in barotropic medium, we have not variation of density in horizontal direction, but density can vary in vertical direction.

In this circumstance; the variation of density in the horizontal direction is only related to variation of temperature in horizontal direction and causes to produce baroclinic atmosphere. In the situation, we define the vectorial difference of geostrophic wind vector at upper level and geostrophic wind vector at lower level of the atmospheric layer as, *thermal wind* again, i.e.:

$$\mathbb{v}_{\mathrm{T}} = \mathbb{v}_{g(p_2)} - \mathbb{v}_{g(p_1)} \tag{1-T}$$

And according to definition (1-T); eastward and northward components of thermal wind can be shown as following:

$$u_{\mathrm{T}} = u_{g(p_2)} - u_{g(p_1)} \tag{2-T-a}$$

and

$$v_{\mathrm{T}} = v_{g(p_2)} - v_{g(p_1)} \tag{2-T-b}$$

For deriving all equations related to this case; firstly, we consider equations (5-D-II-a) and (5-D-II-b), i.e.:

$$u_{\mathrm{D}_{\mathrm{II}}} = \frac{R_d}{f}\int_{p_1}^{p_2}\frac{\partial T_{\mathrm{v}}}{\partial y}\, d\ln p \tag{5-D-II-a}$$

and

$$v_{\mathrm{D}_{\mathrm{II}}} = -\frac{R_d}{f}\int_{p_1}^{p_2}\frac{\partial T_{\mathrm{v}}}{\partial x}\, d\ln p \tag{5-D-II-b}$$

and by substituting equivalent of T_v form equation (6) into above-mentioned equations, we get:

$$u_{\mathrm{D}_{\mathrm{II}}} = \frac{R_d}{f}\int_{p_1}^{p_2}\frac{\partial}{\partial y}[(1+0.608q)T]\, d\ln p \tag{30-D-II-a}$$

and

$$v_{\mathrm{D}_{\mathrm{II}}} = -\frac{R_d}{f}\int_{p_1}^{p_2}\frac{\partial}{\partial x}[(1+0.608q)T]\, d\ln p \tag{30-D-II-b}$$

By applying derivation $\frac{\partial}{\partial y}$ into equation (30-D-II-a), we have:

$$u_{\mathrm{D}_{\mathrm{II}}} = \frac{R_d}{f}\left\{\begin{matrix}\int_{p_1}^{p_2}\left(0.0608\frac{\partial q}{\partial y}\right)T\, d\ln p + \\ \int_{p_1}^{p_2}(1+0.608q)\frac{\partial T}{\partial y}\, d\ln p\end{matrix}\right\} \tag{31}$$

Calculation of first integral of equation (31) yields:

$$\left(0.0608\frac{\partial\langle q\rangle}{\partial y}\langle T\rangle\right)\ln\left(\frac{p_2}{p_1}\right) \tag{32}$$

And according to conditions (12); $\frac{\partial\langle q\rangle}{\partial y}$ is equal to zero, therefore the first integral of equation (31) vanishes and equation (31) for eastward component of dense wind, reduces to eastward component of third particular type of thermal wind, that is:

$$u_{\mathrm{T}_{\mathrm{III}}} = \frac{R_d}{f}\int_{p_1}^{p_2}(1+0.608q)\frac{\partial T}{\partial y}\, d\ln p \tag{5-T-III-a}$$

where in equation (5-T-III-a), $u_{\mathrm{T}_{\mathrm{III}}}$ is eastward component of third particular type of thermal wind.

By applying derivation $\frac{\partial}{\partial x}$ into equation (30-D-II-b) and same mathematical manipulation on equation (30-D-II-a) into this equation, one can derive northward component of third particular type of thermal wind, i.e.

$$v_{\mathrm{T}_{\mathrm{III}}} = -\frac{R_d}{f}\int_{p_1}^{p_2}(1+0.608q)\frac{\partial T}{\partial x}\, d\ln p \tag{5-T-III-b}$$

where in equation (5-T-III-b), $v_{\mathrm{T_{III}}}$ is northward component of third particular type of thermal wind.

Equation (5-T-III-a) used definition of third particular type of thermal wind, i.e.:

$$u_{\mathrm{T_{III}}} \equiv u_{g(p_2)} - u_{g(p_1)} = \int_{p_1}^{p_2} du_g \qquad \text{(2-T-III-a)}$$

Substituting of equivalent $u_{\mathrm{T_{III}}}$, i.e., $\int_{p_1}^{p_2} du_g$ from equation (2-T-III-a) into equation (5-T-III-a) yields:

$$\int_{p_1}^{p_2} du_g = \frac{R_d}{f}\int_{p_1}^{p_2}(1+0.608q)\frac{\partial T}{\partial y}\,d\ln p \qquad (33)$$

Derivation and rearranging equation (33) have following result:

$$\frac{\partial u_g}{\partial \ln p} = \frac{R_d}{f}(1+0.608q)\frac{\partial T}{\partial y} \qquad \text{(19-T-III-a)}$$

By same mathematical manipulation on equation (5-T-III-b), one can get equation (19-T-III-b) for northward component of third particular thermal wind:

$$\frac{\partial v_g}{\partial \ln p} = -\frac{R_d}{f}(1+0.608q)\frac{\partial T}{\partial x} \qquad \text{(19-T-III-b)}$$

Combining equations (19-T-III-a) and (19-T-III-b) yields:

$$\frac{\partial \mathbb{v}_g}{\partial \ln p} = -\frac{R_d}{f}(1+0.608q)\big(\mathbb{k}_p \times \nabla_p T\big) \qquad \text{(3-T-III)}$$

Equation (3-T-III) is "*Third particular type of thermal wind equation*"

Equations (19-T-III-a), (19-T-III-b) and (3-T-III) seem to be similar to equations (19-T-II-a), (19-T-II-b) and (3-T-II) exactly, but there are different between specific humidity for first three above mentioned equations with others. In equations (19-T-II-a), (19-T-II-b) and (3-T-II) specific humidity, q is constant whereas in equations (19-T-III-a), (19-T-III-b) and (3-T-III); although vertical average of specific humidity is same in horizontal direction, i.e., $\frac{\partial\langle q\rangle}{\partial x} = 0$ and $\frac{\partial\langle q\rangle}{\partial y} = 0$; but, in recent equations, $\frac{\partial q}{\partial p} \neq 0$.

By integrating of equation (3-T-III) from lower pressure level p_1 to upper pressure level p_2, $(p_2 < p_1)$ of the atmospheric layer; one can derive "*Third particular type of thermal wind vector*" that is:

$$\mathbb{v}_{\mathrm{T_{III}}} = \mathbb{v}_{g(p_2)} - \mathbb{v}_{g(p_1)} \equiv -\frac{R_d}{f}\int_{p_1}^{p_2}(1+0.608q)\big(\mathbb{k}_p \times \nabla_p T\big)\,d\ln p \qquad \text{(4-T-III)}$$

where in equation (4-T-III); $\mathbb{v}_{g(p_2)}$ is geostrophic wind vector at upper level of the humid atmospheric layer, $\mathbb{v}_{g(p_1)}$ is geostrophic wind vector at lower level of the humid atmospheric layer with following specifications:

$$\left[\frac{\partial\langle q\rangle}{\partial x} = 0 \ \text{ and } \ \frac{\partial\langle q\rangle}{\partial y} = 0\right] \ \text{ but } \ \frac{\partial q}{\partial p} \neq 0 \qquad (12)$$

and, $\mathbb{v}_{\mathrm{T_{III}}}$ stands for third particular type of thermal wind vector, R_d is gas constant for dry air, f is Coriolis parameter, p_1 is atmospheric pressure at lower level of the atmospheric layer, p_2 is atmospheric pressure at upper level of the atmospheric layer, q is specific humidity, $\mathbb{k}_p$ is vertical unit vector in pressure coordinates system, ∇_p stands for gradient operator in pressure coordinates system, T is air temperature and p is atmospheric pressure and vertical axis of pressure coordinates system.

Eastward and northward components of third particular type of thermal wind introduced in equations (5-T-III-a) and (5-T-II-b) earlier.

From third particular type of thermal wind vector or its components; one can find out that:

A: If we go from pole to equator, thermal wind becomes stronger (with pay attention to footnote No. 7);

B: If the horizontal gradient of temperature would be greater, thermal wind becomes stronger, because thermal wind is proportional to the horizontal gradient of temperature;

C: If the pressure difference will be higher in the atmospheric layer, thermal wind becomes more powerful, and finally;

D: If Atmospheric layer has more specific humidity and specific humidity difference will be higher from below level until upper level of the atmospheric layer; then thermal wind will be stronger.

In this manner; representative of third particular type of thermal wind vector, i.e., equation (4-T-III) with consideration of conditions (12) shows that: "*thermal wind blows parallel to isotherms, so that, warm humid air is located at the right side of downwind and cold humid air is located at the left side of downwind.*" (In the northern hemisphere) This fact is illustrated in figures 7 and 8.

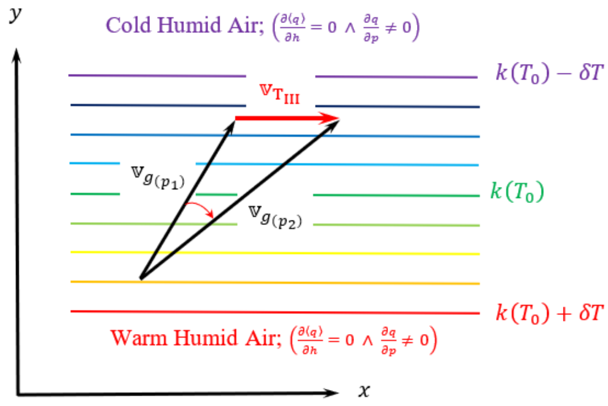

Figure 7. Relationship between clockwise turning of the geostrophic wind with respect to height (veering) and warm humid air advection. Conditions are $\left(\frac{\partial\langle q\rangle}{\partial x} = \frac{\partial\langle q\rangle}{\partial y} = 0 \equiv \frac{\partial\langle q\rangle}{\partial h} = 0 \wedge \frac{\partial q}{\partial p} \neq 0\right)$ and in the case; T_0 is mean temperature of the layer and proportion coefficient k is:

$$k = -\frac{R_d}{f}(1 + 0.608\langle q\rangle)\ln\left(\frac{p_2}{p_1}\right)$$

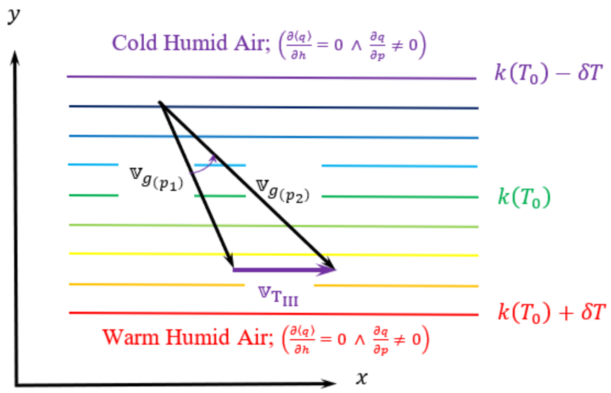

Figure 8. Relationship between counterclockwise turning of the geostrophic wind with respect to height (backing) and cold humid air advection. Conditions are $\left(\frac{\partial\langle q\rangle}{\partial x}=\frac{\partial\langle q\rangle}{\partial y}=0\equiv\frac{\partial\langle q\rangle}{\partial h}=0 \wedge \frac{\partial q}{\partial p}\neq 0\right)$ and in the case; T_0 is mean temperature of the layer and proportion coefficient k is:
$\boldsymbol{k=-\frac{R_d}{f}(1+0.608\langle q\rangle)\ln\left(\frac{p_2}{p_1}\right)}$

As it is shown in figure 7; in the humid atmosphere with consideration conditions (12); a geostrophic wind that turns clockwise with respect to height (veering) is associated with warm humid air advection. Conversely, as shown in figure 8; in the above-mentioned air, counterclockwise turning (backing) of the geostrophic wind with respect to height, implies cold humid air advection by the geostrophic wind in the layer.

Moreover, for third particular type of thermal wind; conditions those were mentioned under first particular type of thermal wind for obtaining cold humid air advection, warm humid air advection, mean temperature field or geostrophic wind at one level of the atmospheric layer with humid air considering conditions (12), by knowing other parameters are true.

Third particular type of thermal wind vector, i.e., equation (4-T-III) has a simple form when we bring out first parenthesis from integrand:

$$\mathbb{v}_{T_{III}}=-\frac{R_d}{f}(1+0.608\langle q\rangle)\int_{p_1}^{p_2}\left(\mathbb{k}_p\times\nabla_p T\right)d\ln p \tag{20-T-III}$$

and simpler form as following:

$$\mathbb{v}_{T_{III}}=-\frac{R_d}{f}(1+0.608\langle q\rangle)\left(\mathbb{k}_p\times\nabla_p\langle T\rangle\right)\ln\left(\frac{p_2}{p_1}\right) \tag{21-T-III}$$

Also, equations (5-T-III-a) and (5-T-III-b) have simple forms as follows:

$$u_{T_{III}}=\frac{R_d}{f}(1+0.608\langle q\rangle)\int_{p_1}^{p_2}\frac{\partial T}{\partial y}d\ln p \tag{34-T-III-a}$$

and

$$v_{T_{III}}=-\frac{R_d}{f}(1+0.608\langle q\rangle)\int_{p_1}^{p_2}\frac{\partial T}{\partial x}d\ln p \tag{34-T-III-b}$$

Even one can write simpler forms of equations (5-T-III-a) and (5-T-III-b) same as following equations:

$$u_{T_{III}}=\frac{R_d}{f}(1+0.608\langle q\rangle)\frac{\partial\langle T\rangle}{\partial y}\ln\left(\frac{p_2}{p_1}\right) \tag{22-T-III-a}$$

and

$$v_{T_{III}}=-\frac{R_d}{f}(1+0.608\langle q\rangle)\frac{\partial\langle T\rangle}{\partial x}\ln\left(\frac{p_2}{p_1}\right) \tag{22-T-III-b}$$

where in equations (20-T-III), (21-T-III), (34-T-III-a), (34-T-III-b), (22-T-III-a) and (22-T-III-b); $\langle\ldots\rangle$ refers to vertical average of phrase or parameter.

There is another method to derive third particular type of thermal wind; that at the moment, we don’t refer to it.

2.1.2 Thermal wind; Approach by Geopotential

Now, we may express the thermal wind for a given atmospheric layer in terms of the geopotential or derivations of it, in the layer. In this case we assume; air is dry, has constant humidity or horizontal gradient of vertical average of specific humidity is zero. i.e.:

$$q=0 \tag{10}$$

or

$$q=constant \tag{11}$$

or

$$\left[\frac{\partial\langle q\rangle}{\partial x}=0 \text{ and } \frac{\partial\langle q\rangle}{\partial y}=0\right] \text{ but } \frac{\partial q}{\partial p}\neq 0 \tag{12}$$

We know, these conditions show that the variation of density in the horizontal direction is merely related to the variation of temperature in horizontal direction causing baroclinity of atmosphere, but we don’t refer to these conditions in this section.

Also, approaching thermal wind by geopotential has two important types that we propound them.

2.1.2.1 Fourth particular type of the thermal wind

Geostrophic wind can be introduced by:

$$\mathbb{v}_g=f^{-1}\mathbb{k}_p\times\nabla_p\Phi \tag{13}$$

Writing eastward and northward components of geostrophic wind yields following equations:

$$u_g=-\frac{1}{f}\frac{\partial\Phi}{\partial y} \tag{14-a}$$

and

$$v_g=\frac{1}{f}\frac{\partial\Phi}{\partial x} \tag{14-b}$$

By vertical integrating of equation (14-a) we get:

$$\int_{p_1}^{p_2} u_g \, dp = -\frac{1}{f}\int_{p_1}^{p_2} \frac{\partial \Phi}{\partial y} dp \qquad (35)$$

And by considering figure 2 we have:

$$u_{g(p_2)} - u_{g(p_1)} \equiv$$

$$u_{\mathrm{T_{IV}}} = -\frac{1}{f}\frac{\partial}{\partial y}(\Phi_2 - \Phi_1) \qquad \text{(5-T-IV-a)}$$

where in equation (5-T-IV-a), $u_{\mathrm{T_{IV}}}$ is eastward component of fourth particular type of thermal wind.

By same mathematical manipulation related to equation (14-a) on equation (14-b), one can get:

$$v_{g(p_2)} - v_{g(p_1)} \equiv$$

$$v_{\mathrm{T_{IV}}} = \frac{1}{f}\frac{\partial}{\partial x}(\Phi_2 - \Phi_1) \qquad \text{(5-T-IV-b)}$$

where in equation (5-T-IV-b), $v_{\mathrm{T_{IV}}}$ is northward component of fourth particular type of thermal wind.

Combining equations (5-T-IV-a) and (5-T-IV-b) yields:

$$\mathbb{v}_{g(p_2)} - \mathbb{v}_{g(p_1)} \equiv$$

$$\mathbb{v}_{\mathrm{T_{IV}}} = \frac{1}{f}\left[\mathbb{k}_p \times \nabla_p(\Phi_2 - \Phi_1)\right] \qquad \text{(4-T-IV)}$$

where in equation (4-T-IV); $\mathbb{v}_{g(p_2)}$ is geostrophic wind vector at upper level of the atmospheric layer, $\mathbb{v}_{g(p_1)}$ is geostrophic wind vector at lower level of the atmospheric layer, $\mathbb{v}_{\mathrm{T_{IV}}}$ stands for *fourth particular type of thermal wind vector*, f is Coriolis parameter, $\mathbb{k}_p$ is vertical unit vector in pressure coordinates system, ∇_p stands for gradient operator in pressure coordinates system, Φ_2 is geopotential at upper level of the atmospheric layer and Φ_1 is geopotential at lower level of the atmospheric layer.

The term "geopotential height" refers to height of a given point in the atmosphere in units proportional to the potential energy of unit mass (geopotential) at this height relative to -mean- sea level. [10]

The relation, in SI units, between the geopotential height Z and geometric height z is:

$$Z = \frac{1}{g_0}\int_0^z g dz \qquad (36)$$

where g is acceleration of gravity and g_0 is the globally averaged acceleration of gravity at sea level ($g_0 = 9.80665 \ \mathrm{ms^{-2}}$) so that the two heights are numerically interchangeable for most meteorological purposes.

Therefore, for most purposes, it is sufficiently accurate to take gravitational acceleration g as a constant, given approximately by:

$$g \approx g_0 \approx 9.8 \ \mathrm{ms^{-2}} \qquad (37)$$

If the sea is at rest, its surface would coincide with the geopotential surface[8]. This geopotential surface is called -mean- sea level and is defined as $\Phi = 0$. To a good approximation, so the vertical coordinate z measures distance upward from this reference level, so

$$\Phi \approx gz \approx g_0 z \qquad (38)$$

Geopotential is sometimes given in units of the geopotential meter (gpm) defined by:

$$1 \ \mathrm{gpm} = 9.8 \ \mathrm{m^2 s^{-2}} \equiv 1 \ \mathrm{Jkg^{-1}} \qquad (39)$$

so that, the value of the geopotential in geopotential meters is close to the height in meters. Alternatively, the geopotential height Z is defined by:

$$Z = {}^{\Phi}\!/_{g_0} \qquad (40)$$

so that the geopotential height in meters is numerically the same as the geopotential in geopotential meters. [8]

Equation (38) shows geopotential is proportional to height; then:

$$(\Phi_2 - \Phi_1) \approx g(z_2 - z_1) \qquad (41)$$

where in equation (41), Φ_2 is geopotential of upper level of the atmospheric layer, Φ_1 stands for geopotential of lower level of the atmospheric layer, g is gravitational acceleration, z_2 is height of upper level of the atmospheric layer and $z_1$stands for height of lower level of the atmospheric layer. And $(z_2 - z_1)$ is the thickness of the layer. (See figure 2)

Now, from fourth particular type of thermal wind vector or its components; one can find out that:

A: If we go from pole to equator, fourth particular type of thermal wind becomes stronger (with pay attention to footnote No. 7);

B: If the horizontal gradient of thickness of the layer would be greater, fourth particular type of thermal wind becomes stronger, because the thermal wind is proportional to the horizontal gradient of thickness of the atmospheric layer and:

C: If the geopotential difference between lower level and upper level of the atmospheric layer will be higher, thermal wind becomes more powerful.

In this manner; representative of fourth particular type of thermal wind vector, i.e., equation (4-T-IV) with consideration of condition (10) shows that: "*fourth particular type of thermal wind blows parallel to isopleth of thickness, so that, more thickness of the atmospheric layer is located at the right side of downwind and less thickness of the atmospheric layer is located at the left side of downwind.*" (In the northern hemisphere) This fact is illustrated in figures 9 and 10.

---

[8] Or "*Base geopotential*"

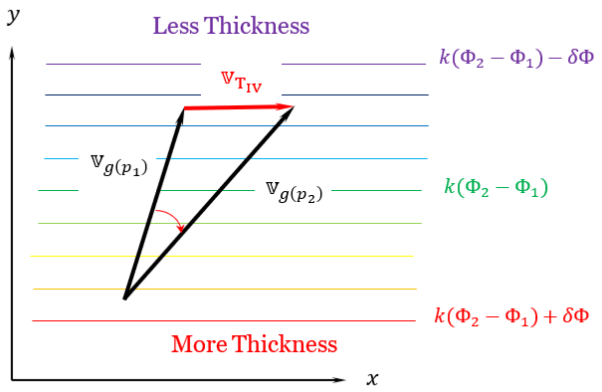

Figure 9. Relationship between clockwise turning of the geostrophic wind with respect to height (veering) and more thickness advection. In the case; proportion coefficient k is: $k=\frac{1}{f}$

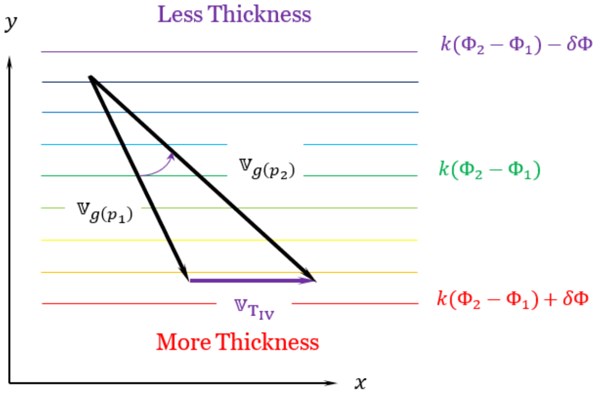

Figure 10. Relationship between counterclockwise turning of the geostrophic wind with respect to height (backing) and less thickness advection. In the case; proportion coefficient k is: $k=\frac{1}{f}$

As it is shown in figure 9; a geostrophic wind that turns clockwise with respect to height (veering) is associated with more thickness advection. Conversely, as shown in figure 10; counterclockwise turning (backing) of the geostrophic wind with respect to height, implies less thickness advection by the geostrophic wind in the layer.

It is therefore possible to obtain a reasonable estimate of the mean thickness change of the atmospheric layer between two near upper air stations from data on the vertical profile of the wind given by soundings at those upper air stations. Alternatively, the mean geostrophic wind at two points of one level of the atmospheric layer between two near upper air stations can be estimated from the mean thickness field advection of that layer provided that the mean geostrophic wind velocity is known at other level. Thus, for example, if the mean geostrophic wind velocity at 850 hPa is known from two near upper air stations and the mean gradient of the thickness in the layer 850 – 500 hPa between two near upper air stations is also known; the fourth particular type of thermal wind equation can be applied to obtain the mean geostrophic wind velocity in the layer at 500 hPa.

2.1.2.2 Fifth particular type of the thermal wind

Consider equations (5-T-IV-a) and (5-T-IV-b):

$$u_{T_{IV}} = -\frac{1}{f}\frac{\partial}{\partial y}(\Phi_2-\Phi_1) \qquad \text{(5-T-IV-a)}$$

$$v_{T_{IV}} = \frac{1}{f}\frac{\partial}{\partial x}(\Phi_2-\Phi_1) \qquad \text{(5-T-IV-b)}$$

If we replace equivalent of $(\Phi_2-\Phi_1)$ from equation (41) into above-mentioned equations, we get:

$$u_{T_V} = -\frac{g}{f}\frac{\partial}{\partial y}(z_2-z_1) \qquad \text{(5-T-V-a)}$$

$$v_{T_V} = \frac{g}{f}\frac{\partial}{\partial x}(z_2-z_1) \qquad \text{(5-T-V-b)}$$

where in equation (5-T-V-a), u_{T_V} is eastward component of fifth particular type of thermal wind and in equation (5-T-V-b), v_{T_V} is northward component of fifth particular type of thermal wind and other parameters have been introduced under equation (41). Combining equations (5-T-V-a) and (5-T-V-b) yields fifth particular type of thermal wind vector:

$$\mathbb{V}_{T_V} = \frac{g}{f}\left[\mathbb{k}_p \times \nabla_p[(z_2-z_1)]\right] \qquad \text{(4-T-V)}$$

where in equation (4-T-V), $\mathbb{V}_{T_V}$ stands for *fifth particular type of thermal wind vector*, g is acceleration of gravity, f is Coriolis parameter, $\mathbb{k}_p$ is vertical unit vector in pressure coordinates system, ∇_p stands for gradient operator in pressure coordinates system, z_2 is altitude of upper level of the atmospheric layer and z_1 is altitude of lower level of the atmospheric layer.

From fifth particular type of thermal wind vector or its components; one can find out that:

A: If we go from pole to equator, fifth particular type of thermal wind becomes stronger (with pay attention to footnote No. 7);

B: If the horizontal gradient of thickness of the layer would be greater, fifth particular type of thermal wind becomes stronger, because the thermal wind is proportional to the horizontal gradient of thickness of the atmospheric layer and:

C: If the altitude difference between lower level and upper level of the atmospheric layer will be higher, thermal wind becomes more powerful.

In this manner; representative of fifth particular type of thermal wind vector, i.e., equation (4-T-V) shows that: “*fifth particular type of thermal wind blows parallel to isopleth of thickness, so that, more thickness of the atmospheric layer is located at the right side of downwind and less thickness of the atmospheric layer is located at the left side of downwind.*” (In the northern hemisphere) This fact is illustrated in figures 11 and 12.

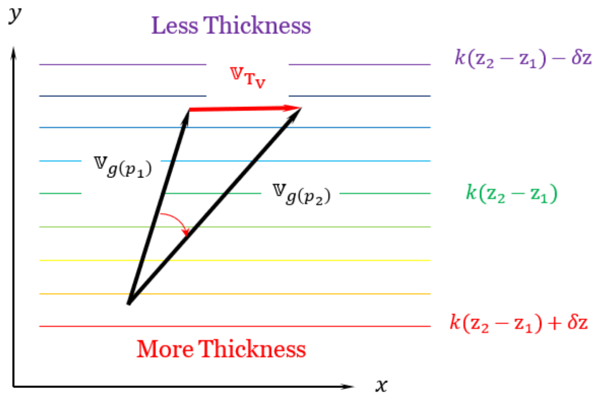

Figure 11. Relationship between clockwise turning of the geostrophic wind with respect to height (veering) and more thickness advection. In the case; proportion coefficient k is: $k=\frac{g}{f}$

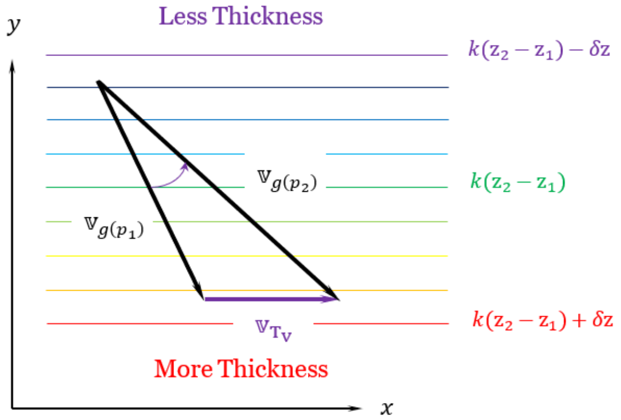

Figure 12. Relationship between counterclockwise turning of the geostrophic wind with respect to height (backing) and less thickness advection. In the case; proportion coefficient k is: $k=\frac{g}{f}$

As it is shown in figure 11; a geostrophic wind that turns clockwise with respect to height (veering) is associated with more thickness advection. Conversely, as shown in figure 12; counterclockwise turning (backing) of the geostrophic wind with respect to height, implies less thickness advection by the geostrophic wind in the layer.

Other specifications of fourth particular type of thermal wind are true for fifth particular type of thermal wind.

2.2. Second special case of dense wind: Moist wind

Another feature of dense wind that we introduce it as second special case of it, is moist wind.

If we assume that temperature in horizontal direction doesn't change;[9] – as it is true in most regions at tropics – i.e.

$$\frac{\partial T}{\partial x}=0 \text{ and } \frac{\partial T}{\partial y}=0 \tag{42}$$

In conditions No. (42); the variation of density in the horizontal direction is merely related to variation of humidity in horizontal direction causing baroclinity of the atmosphere. In these circumstances; we define the vectorial difference of geostrophic wind vector at upper level and geostrophic wind vector at lower level of the atmospheric layer as, *moist wind*, i.e.:

$$\mathbb{V}_{\mathrm{M}}\equiv\mathbb{V}_{g(p_2)}-\mathbb{V}_{g(p_1)} \tag{1-M}$$

where in Equation (1-M) $\mathbb{V}_{\mathrm{M}}$ stands for moist wind vector, $\mathbb{V}_g$ is geostrophic wind and subscripts p_1 and p_2 refer to pressure levels in the manner that level p_2 has more height than level p_1, i.e., $p_2<p_1$.

According to definition (1-M); eastward and northward components of Moist wind can be shown as following:

$$u_{\mathrm{M}}=u_{g(p_2)}-u_{g(p_1)} \tag{2-M-a}$$

and

$$v_{\mathrm{M}}=v_{g(p_2)}-v_{g(p_1)} \tag{2-M-b}$$

where in equations (2-M-a) and (2-M-b) u_{M} is eastward component of moist wind, v_{M} is northward component of moist wind, u_g is eastward component of geostrophic wind, v_g is northward component of geostrophic wind and subscripts p_1 and p_2 refer to pressure levels in the manner that level p_2 has more height than level p_1, i.e., $p_2<p_1$.

Also, approaching to derive moist wind equations has two branches. 1 – Temperature branch and 2 – Geopotential branch.

2.2.1 Moist wind; Approach by Temperature

For the second version of dense wind; dense wind equation was:

$$\frac{\partial\mathbb{V}_g}{\partial\ln p}=-\frac{R_d}{f}\left(\mathbb{k}_p\times\nabla_pT_v\right) \tag{3-D-II}$$

If we decompose equation (3-D-II) into its components, we get: [1]

$$\frac{\partial u_g}{\partial\ln p}=\frac{R_d}{f}\frac{\partial T_{\mathrm{v}}}{\partial y} \tag{43-a}$$

and

$$\frac{\partial v_g}{\partial\ln p}=-\frac{R_d}{f}\frac{\partial T_{\mathrm{v}}}{\partial x} \tag{43-b}$$

Substituting equivalent of T_v from equation (6) into equation (43-a) yields:

$$\frac{\partial u_g}{\partial\ln p}=\frac{R_d}{f}\frac{\partial(1+0.608q)T}{\partial y} \tag{44}$$

and applying derivative on right side of equation (44) yields:

---

[9] But can change in vertical direction i.e., $\frac{\partial T}{\partial p}\neq0$

$$\frac{\partial u_g}{\partial \ln p} = \frac{R_d}{f}\left[\frac{\partial(1+0.608q)}{\partial y}T + (1+0.608q)\frac{\partial T}{\partial y}\right] \qquad (45)$$

According to conditions (42) $\frac{\partial T}{\partial y} = 0$ and second term on the right hand of (45) vanishes. Now we have:

$$\frac{\partial u_g}{\partial \ln p} = (0.608)\frac{R_d T}{f}\left(\frac{\partial q}{\partial y}\right) \qquad (19\text{-M-I-a})$$

By same mathematical manipulation on equation (43-b), we have:

$$\frac{\partial v_g}{\partial \ln p} = -(0.608)\frac{R_d T}{f}\left(\frac{\partial q}{\partial x}\right) \qquad (19\text{-M-I-b})$$

Combining equations (19-M-I-a) and (19-M-I-b) yields:

$$\frac{\partial \mathbb{v}_g}{\partial \ln p} = -(0.608)\frac{R_d T}{f}\left(\mathbb{k}_p \times \nabla_p q\right) \qquad (3\text{-M-I})$$

Equation (3-M-I) is "*First prominent type of moist wind equation*"

By integrating of equation (3-M-I) from lower pressure level p_1 to upper pressure level p_2, $(p_2 < p_1)$ of the atmospheric layer (see figure 2); one can derive "*First prominent type of moist wind vector*" that is:

$$\mathbb{v}_{g(p_2)} - \mathbb{v}_{g(p_1)} \equiv$$
$$\mathbb{v}_{\mathrm{M_I}} = -(0.608)\frac{R_d}{f}\int_{p_1}^{p_2} T\left(\mathbb{k}_p \times \nabla_p q\right) d\ln p \qquad (4\text{-M-I})$$

where in equations (19-M-I-a), (19-M-I-b), (3-M-I) and (4-M-I): u_g is eastward component of geostrophic wind, v_g is northward component of geostrophic wind, $\mathbb{v}_g$ is geostrophic wind, $\mathbb{v}_{\mathrm{M_I}}$ stands for first prominent type of moist wind, R_d is gas constant for dry air, p_1 is lower pressure of the atmospheric layer, p_2 is upper pressure of the atmospheric layer, T is temperature, $\mathbb{k}_p$ is vertical unit vector in pressure coordinates system, q is specific humidity and p is pressure as vertical coordinate of pressure coordinates system.

Eastward and northward components of first prominent type of moist wind can derive from equation (4-M-I) easily. Those are in following lines:

$$u_{\mathrm{M_I}} = (0.608)\frac{R_d}{f}\int_{p_1}^{p_2} T\frac{\partial q}{\partial y}d\ln p \qquad (5\text{-M-I-a})$$

and:

$$v_{\mathrm{M_I}} = -(0.608)\frac{R_d}{f}\int_{p_1}^{p_2} T\frac{\partial q}{\partial x}d\ln p \qquad (5\text{-M-I-b})$$

where in equation (5-M-I-a), $u_{\mathrm{M_I}}$ is eastward component of first prominent type of the moist wind and in equation (5-M-I-b), $v_{\mathrm{M_I}}$ stands for northward component of first prominent type of the moist wind and other parameters were defined after equation (4-M-I).

From first prominent type of moist wind vector or its components; one can find out that:

A: If we go from pole to equator, moist wind becomes stronger (with pay attention to footnote No. 7);

B: Increasing temperature causes to produce power-up of moist wind;

C: If the horizontal gradient of specific humidity would be greater, moist wind becomes stronger, because moist wind is proportional to the horizontal gradient of specific humidity and finally;

D: If the pressure difference will be higher in the atmospheric layer, moist wind becomes more powerful.

In this manner; representative of first prominent type of moist wind vector, i.e., equation (4-M-I) with consideration of conditions (42) shows that: "*moist wind blows parallel to isopleths of specific humidity, so that, air with more specific humidity is located at the right side of downwind and air with less specific humidity is located at the left side of downwind.*" (In the northern hemisphere) This fact is illustrated in figures 13 and 14.

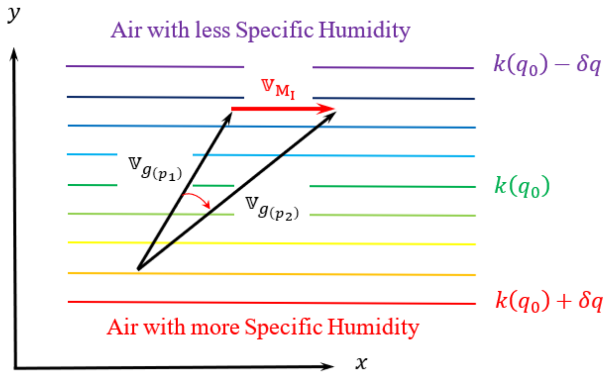

Figure 13. Relationship between clockwise turning of the geostrophic wind with respect to height (veering) and more specific humidity advection. Conditions: q_0 is mean specific humidity of the atmospheric layer and in the case; proportion coefficient k is: $k = -(0.608)\frac{R_d}{f}\langle T\rangle \ln\left(\frac{p_2}{p_1}\right)$

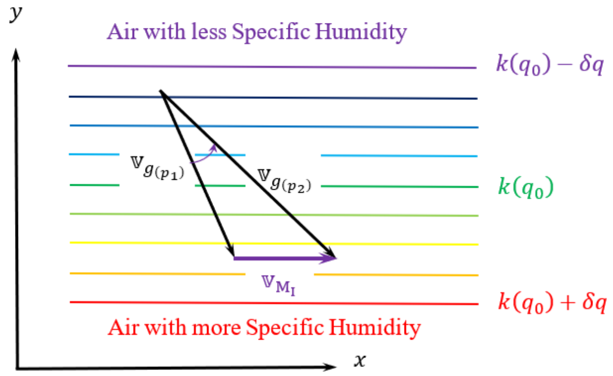

Figure 14. Relationship between counterclockwise turning of the geostrophic wind with respect to height (backing) and less specific humidity advection. Conditions: q_0 is mean specific humidity of the atmospheric layer and in the case; proportion coefficient k is: $k = -(0.608)\frac{R_d}{f}\langle T\rangle \ln\left(\frac{p_2}{p_1}\right)$

As it is shown in figure 13; in the humid atmosphere with consideration condition (42) – in the isothermal atmosphere in which, the horizontal gradient of temperature would be zero –; a geostrophic wind that turns clockwise with respect to height (veering) is associated with more specific humidity advection. Conversely, as shown in figure 14; in the above-mentioned air, counterclockwise turning (backing) of the geostrophic wind with respect to height, implies less specific humidity advection by the geostrophic wind in the layer.

It is therefore possible to obtain a reasonable estimate of the mean specific humidity advection of the atmospheric layer between two near upper air stations from data on the vertical profile of the wind given by soundings at those upper air stations. Alternatively, the mean geostrophic wind at two points of one level of the atmospheric layer between two near upper air stations can be estimated from the mean field of specific humidity advection of that layer provided that the mean geostrophic wind velocity is known at other level. Thus, for example, if the mean geostrophic wind velocity at 850 hPa is known from two near upper air stations and the mean specific humidity advection in the layer 850 – 500 hPa between two near upper air stations is also known; the first prominent type of the moist wind equation can be applied to obtain the mean geostrophic wind velocity in the layer at 500 hPa.

First prominent type of moist wind vector, i.e., equation (4-M-I) has a simple form by integration with respect to vertical axis, as following:

$$\mathbb{v}_{\mathrm{M_I}} = -(0.608)\frac{R_d}{f}\langle T\rangle\left(\mathbb{k}_p \times \nabla_p\langle q\rangle\right)\ln\left(\frac{p_2}{p_1}\right) \tag{21-M-I}$$

where in equation (21-M-I), $\langle \dots \rangle$ is vertical averaging of phrase or parameter.

Analogous to simplification of equation (4-M-I); we can obtain simple form of equations (5-M-I-a) and (5-M-I-b) those show simple forms for components of first prominent type of moist wind vector for humid air with conditions (42); those are:

$$u_{\mathrm{M_I}} = (0.608)\frac{R_d}{f}\langle T\rangle\frac{\partial\langle q\rangle}{\partial y}\ln\left(\frac{p_2}{p_1}\right) \tag{22-M-I-a}$$

and:

$$v_{\mathrm{M_I}} = -(0.608)\frac{R_d}{f}\langle T\rangle\frac{\partial\langle q\rangle}{\partial x}\ln\left(\frac{p_2}{p_1}\right) \tag{22-M-I-b}$$

Again, in equations (22-M-I-a) and (22-M-I-b), $\langle \dots \rangle$ is vertical averaging of phrase or parameter and furthermore, in equation (22-M-I-a) $u_{\mathrm{M_I}}$ is eastward component of moist wind by first prominent type and in equation (22-M-I-b) $v_{\mathrm{M_I}}$ is northward component of moist wind in first prominent type.

2.2.2. Moist wind; Approach by Geopotential

Conditions (42) is opposite to conditions (10), (11) and (12).

By considering conditions (12); if we apply the same process to derive equation (4-T-IV) here plus bearing in mind conditions (42); we get the other form of moist wind vector named second prominent type of moist wind, as we got in the case of dense wind i.e.:

$$\mathbb{v}_{\mathrm{M_{II}}} = \frac{1}{f}\mathbb{k}_p \times \nabla_p(\Phi_2 - \Phi_1) \tag{4-M-II}$$

where in equation (4-M-II); $\mathbb{v}_{\mathrm{M_{II}}}$ stands for *second prominent type of moist wind vector*, f is Coriolis parameter, $\mathbb{k}_p$ is vertical unit vector in pressure coordinates system, ∇_p stands for gradient operator in pressure coordinates system, Φ_2 is geopotential at upper level of the atmospheric layer and Φ_1 is geopotential at lower level of the atmospheric layer.

Equation (4-M-II) is another version of the moist wind and states that: *second prominent type of moist wind is proportional to horizontal gradient of the thickness of the layer* and this subject is true if the variation of the thickness of the layer would produce only with the horizontal gradient of specific humidity.

From equation (4-M-II) we can derive eastward and northward components of second prominent type of moist wind easily:

$$u_{\mathrm{M_{II}}} = -\frac{1}{f}\frac{\partial}{\partial y}(\Phi_2 - \Phi_1) \tag{5-M-II-a}$$

$$v_{\mathrm{M_{II}}} = \frac{1}{f}\frac{\partial}{\partial x}(\Phi_2 - \Phi_1) \tag{5-M-II-b}$$

where in equation (5-M-II-a), $u_{\mathrm{M_{II}}}$ is eastward component of second prominent type of the moist wind and $v_{\mathrm{M_{II}}}$ is northward component of second prominent type of moist wind.

From second prominent type of moist wind vector or its components; one can find out that:

A: If we go from pole to equator, second prominent type of moist wind becomes stronger (with pay attention to footnote No. 7);

B: If the horizontal gradient of thickness of the layer would be greater, second prominent type of moist wind becomes stronger, because the moist wind is proportional to the horizontal gradient of thickness of the atmospheric layer and:

C: If the geopotential difference between lower level and upper level of the atmospheric layer will be higher, moist wind becomes more powerful.

In this manner; representative of second prominent type of moist wind vector, i.e., equation (4-M-II) with consideration of condition (42) shows that: "*second prominent type of moist wind blows parallel to isopleth of thickness, so that, more thickness of the atmospheric layer is located at the right side of downwind and less thickness of the atmospheric layer is located at the left side of downwind.*" (In the northern hemisphere) This fact is illustrated in figures 15 and 16.

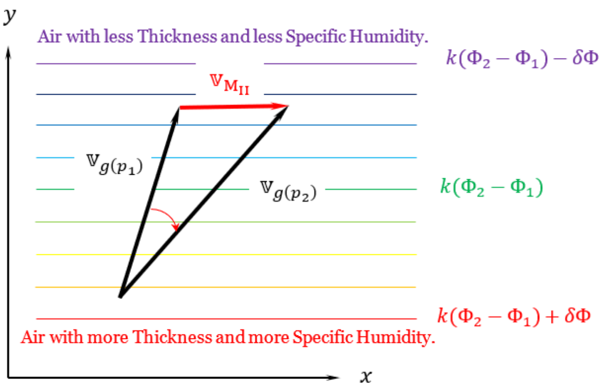

Figure 15. Relationship between clockwise turning of the geostrophic wind with respect to height (veering) and more thickness and more specific humidity advection. In the case; proportion coefficient k is: $k = \frac{1}{f}$

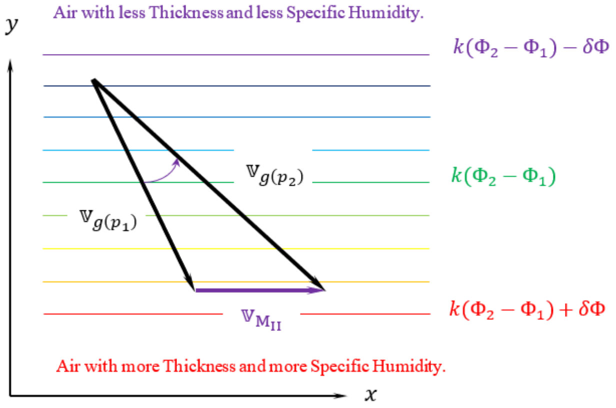

Figure 16. Relationship between counterclockwise turning of the geostrophic wind with respect to height (backing) and less thickness and less specific humidity advection. In the case; proportion coefficient k is: $k = \frac{1}{f}$

As it is shown in figure 15; a geostrophic wind that turns clockwise with respect to height (veering) is associated with more thickness and more specific humidity advection. Conversely, as shown in figure 16; counterclockwise turning (backing) of the geostrophic wind with respect to height, implies less thickness and less specific humidity advection by the geostrophic wind in the layer.

It is therefore possible to obtain a reasonable estimate of the mean thickness and specific humidity change of the atmospheric layer between two near upper air stations from data on the vertical profile of the wind given by soundings at those upper air stations. Alternatively, the mean geostrophic wind at two points of one level of the atmospheric layer between two near upper air stations can be estimated from the mean thickness and specific humidity field advection of that layer provided that the mean geostrophic wind velocity is known at other level. Thus, for example, if the mean geostrophic wind velocity at 850 hPa is known from two near upper air stations and the mean gradient of the thickness and changes of specific humidity in the layer 850 – 500 hPa between two near upper air stations are also known; the second prominent type of moist wind equation can be applied to obtain the mean geostrophic wind velocity in the layer at 500 hPa.

Therefore; the moist wind equation is an extremely useful diagnostic tool, which can use to check analyses of the observed wind and specific humidity fields for consistency; in the regions – same tropics – that environment is extremely isothermal[10].

3. Attention for similarities

There are some similarities in this work.

You realize that formulae (4-D-III), (4-T-IV) and (4-M-II) are alike.

Although, figure 9 – related to formula (4-T-IV) –, figure 15 – related to formula (4-M-II) – and figure related to formula (4-D-III) – that introduced in part I of this research – are alike.

Furthermore, figure 10 – related to formula (4-T-IV) – figure 16 – related to formula (4-M-II) – and figure related to formula (4-D-III) – that introduced in part I of this research – are alike.

Despite of above-mentioned similarities; there are basic discrepancies between them that will be explain in following paragraphs.

Formula (4-D-III) and related figures about it – those were presented in part I of this research –, were arisen from baroclinic weather that baroclinity of it, is related to both horizontal gradient of temperature and horizontal gradient of humidity.

Formula (4-T-IV), figure 9 and figure 10 were arisen from baroclinic weather that baroclinity of it, is related to horizontal gradient of temperature solely.

And formula (4-M-II) and figures 15 and 16 were arisen from baroclinic weather that baroclinity of it, were arisen from horizontal gradient of specific humidity solely.

Therefore; although – in above-mentioned formulae and figures –, there are similarities apparently; but in interior of them, there are striking differences between them.

4. Results and Discussion

All versions of dense wind equations, thermal wind equations and moist wind equations; are an extremely useful diagnostic tools, which is often used to check analyses of the observed wind field for consistency.

The proposition of dense wind, thermal wind and moist wind, those are propounded for the first time with these kind configurations; can help to better understanding of atmosphere dynamics. Furthermore, knowing the

---

[10] Note that here; we focus on isothermal environment; otherwise, the geostrophic wind has no physical meaning at equator or the regions near it. Although, the proposition of moist wind is valid there, and that is vectorial difference between wind in the vertical direction with some difference.

advection of the warm air, cold air, moist air, dry air or thickness of the atmospheric layer with exclusive specifications; can help to improve weather forecasting. Although, we referred to the variation of the geostrophic wind with respect to height here; but this proposition is valid for the variation of real wind in vertical direction with some modifications that needs separate discussion.

Thermal wind, moist wind or – as exist in the nature of the whole atmosphere – except somewhere that thermal or moist wind is true – dense wind; is struggle of the atmosphere to return thermodynamic equilibrium and complete the dynamic cycle of atmosphere.

As we noticed in part I of the research; this movement begins from the fact that solar radiation disturbs the thermodynamic equilibrium, resulting production of horizontal gradient of density. Horizontal gradient of density produces horizontal gradient of potential energy and in turn, this condition forces atmosphere to generate horizontal gradient of pressure gradian force and finally, it causes blow wind, for returning thermodynamic equilibrium of the atmosphere.

Due to various incoming solar radiation and non-uniform transfer of heat flux and humidity flux and diffusion of them from below of different layers of the atmosphere; atmosphere will be baroclinic and horizontal gradients of density are not same in the layers and wind velocities can’t be the same at all atmospheric layers i.e., vertical shear of the wind. Therefore, this phenomenon produces dense wind that is effort of atmosphere to return into its thermodynamic equilibrium and reducing dense wind speed. By continuous reduction of dense wind speed, thermodynamic disequilibrium of atmosphere weakens and weakens, until reaching of thermodynamic equilibrium of the atmosphere. If we assume there will be no more solar radiation, finally the wind will be disappeared in presence of friction.

So, dense wind is the key of understanding for dense or light air, virtual temperature or thickness of the atmospheric layer advections and is one of the mechanisms of returning thermodynamic equilibrium of atmosphere.

And the same conditions are true for thermal wind and moist wind under their own situations.

5. Conclusions

This point is important that scale analysis can determine at which region the moist wind governs rather than thermal wind and vise-versa and where we can’t apply any of them and we ought to use dense wind. Perhaps, this is the best result from the point that: *Looking at the variation of the geostrophic wind with respect to height – in general –, shouldn’t limit to dry atmosphere and we expect only one form of thermal wind from this process, because atmosphere has humidity; as well as we shouldn’t conclude moist wind from it, because – in general – atmosphere is not isothermal; because in general the air is not dry, as well as it is not isothermal in horizontal direction therefore, the variation of the geostrophic wind with respect to height should be describe with better tool, namely dense wind.*

Also, we have noticed in part I of this research; “It is necessary to note two basic points. First; until God wills and sun radiates; atmospheric and oceanic mediums are baroclinic. And the theory of barotropic medium – same as geostrophic wind – is acceptable for simplification of meteorological and oceanic analyses. Second point is with regard to more affection of temperature in variation of air density; although in many places far from oceanic medium, the dense wind gains energy more from horizontal gradient of temperature rather than the horizontal gradient of humidity, but it is not sufficient reason to call the vectorial difference of the geostrophic wind at upper and lower level of the atmospheric layer as thermal wind, because we can’t deny presence of humidity anywhere.”

6. References

[1] Zamanian, M. T., 2022: A New Look at the Vertical Shear of the Geostrophic Wind. Part I: Dense Wind. *International Journal of Coastal & Offshore Engineering*. Vol. **7**(**3**), 10-19 pp.

[2] Kim S. W., S. U. Park and C. H. Moeng, 2003: Entrainment processes in the convective boundary layer with varying wind shear. Boundary-layer meteorology, **108**, 221-245 pp.

[3] Charnock, H., Francis, J. R. D. and Sheppard, P. A., (1956), *An Investigation of Wind Structure in the Trades: Anegada 1953*. Philosophical Transactions of the Royal Society of London, Ser. A, **249**, 179-234.

[4] Carlstead, M., (1959), Forecasting Middle Cloudiness and Precipitation Areas by Numerical Methods. *Mon. Wea. Rev.*, **87**, 375-381.

[5] Estoque, M. A., (1971), The Planetary Boundary Layer Wind over Christmas Island. *Mon. Wea. Rev.*, **99**, 193-201.

[6] Foster, R. C. and Levy, G., (1998), *The Contribution of Organized Roll Vortices to the Surface Wind Vector in Baroclinic Conditions*, Journal of the Atmospheric Science, **55** (8), p.1466-1472.

[7] Hess, S. L., (1959), *Introduction to Theoretical Meteorology,* Malabar, Krieger Publishing, xiv + 364 pp.

[8] Gill, A. E., (1982), *Atmosphere-Ocean Dynamics,* San Diego, Academic press, xv + 662 pp.

[9] Dutton, J. A., (1995), *Dynamics of Atmospheric Motion,* New York, Dover Publications, Inc., xx + 617 pp.

[10] Holton, J. R. and, G. J. Hakim, (2013), *An Introduction to Dynamic Meteorology,* Amsterdam, 5th edition, Elsevier, xvi + 532 pp.

[11] Glickman, T. S. (managing editor), (2000), *Glossary of Meteorology*, Boston, 2nd edition, American Meteorological Society, xii + 855 pp.

[12] Curry J. A. and P. J. Webster, (1999), *Thermodynamics of Atmosphere and Oceans.* San Diego, Academic Press, xvii + 471pp.

[13] Iribarne, J. V. and W. L. Godson, (1981), *Atmospheric Thermodynamics.* Dordrecht, D. Reidel Publishing Co., xv + 259 pp.

[14] Haltiner, G. J. and R. T. Williams, (1980), *Numerical Prediction and Dynamic Meteorology*. New York, John Wiley & Sons, xvii + 477 pp.

INTERNATIONAL JOURNAL OF
COASTAL, OFFSHORE & ENVIRONMENTAL ENGINEERING
IJCOE Vol.8/No. 2/Spring 2023 (40-47)

Available online at: www. Ijcoe.org

Study of surface fluxes over the Northern Indian Ocean Seas

Rozana Ghandy[1], AbbasAli Aliakbari Bidokhti[2*], Parviz Irannejad[3], Mojtaba Ezam[4]

[1] *Faculty of Natural Resources and Environment, Science and Research Branch, Islamic Azad University, Tehran, Iran*
[2*] *Prof. of Environmental Fluid Mechanics Institute of Geophysics University of Tehran, Tehran, Iran; bidokhti@ut.ac.ir*
[3] *Institute of Geophysics University of Tehran, Tehran, Iran*
[4] *Faculty of Natural Resources and Environment, Science and Research Branch, Islamic Azad University, Tehran, Iran*

ARTICLE INFO

Article History:
Received: 07 Aug. 2021
Accepted: 23 May. 2023

Keywords:
Latent heat flux
Sensible heat flux
Persian Gulf
Gulf of Oman
Northern Indian Ocean

ABSTRACT

The open waters of the north Indian Ocean (NIO), which itself includes the Persian Gulf (PG), the Gulf of Oman (GO), and the Arabian Sea (AS), are subject to different meteorological forcing that can affect surface fluxes of these environments. In this study, latent heat flux (Q_{LH}), sensible heat flux (Q_{SH}), and surface wind stress (τ) between these regions are investigated. The reanalysis data from the data sets of the National Centers for Environmental Prediction (NCEP) and the European Center for Medium-Range Weather Forecasts (ECMWF) for these three regions for 14 years (2013-2000) are used. The results are compared with the measured data in the GO that show ECMWF reanalysis data are more consistent with the measured data in this period. We compare the average monthly, seasonal and annual values of Q_{LH}, Q_{SH} and τ of the PG, GO, and AS. The annual averages of Q_{LH} for the PG, the GO, and the AS are -128.63, -118.76, and -118.03 (Wm^{-2}) and the annual averages of Q_{SH} are -1.28, -3.88, and -5.67 (Wm^{-2}) respectively. The annual averages of τ are 0.074, 0.075, 0.036 (Pa) for these areas respectively. Also the annual average SST is 27, 26.56, and 27.14 (°C) respectively for these areas. Based on the results, different regimes of the PG wind and its dust storms, on the one hand, and the limited and semi-closed space of the PG with its shallow depth, on the other hand, leads to different behaviors of Q_{LH} and Q_{SH} in PG area, in comparison with the other two environments (namely GO and AS).

1. Introduction

Study of the distribution of heat fluxes (Q_s) between air and sea has an influential role in understanding changes in weather systems, climate conditions, and changes in water surface temperature and transfer of gases across the air-sea interface [1].

The heat storage capacity of the oceans large and is mainly provided at interface [2]. Wind stress and heat exchange at the interface between air and sea can cause turbulent mixing of the water mass and determine the ocean mixed layer [3]. The warming process in the Indian Ocean is a major contributor to the overall average sea surface temperature (SST) trend that can have a global atmospheric effect especially in the tropical Indian Ocean. The Arabian Sea (AS) in the face of seasonal atmospheric forcing undergoes many changes, which are mainly annual changes and some interannual intermediate [4].

The net heat transfer in the earth system is mainly mediated by solar radiation (Q_{SW}), longwave radiation (Q_{LW}), sensible heat flux (Q_{SH}), convection (Q_V) and latent heat flux (Q_{LH}) [5]; according to the following formula:

$$Q=Q_{SW}+Q_{LW}+Q_{LH}+Q_{SH}+Q_V \qquad (1)$$

Due to the importance of ocean Q distribution, many studies have been performed to identify each of the parameters in different oceans and seas [6]. Each of the parameters can be calculated directly (by direct measurement) or indirectly (using empirical formulas).

Because direct measurements are costly and limited in time and domain [5], the use of empirical formulas as aerodynamic bulk formula are commonly used to calculate Q_{SH} and Q_{LH}, which are as follows:

$$Q_{SH}=\rho\, C_p\, C_S\, U_{10}\,(t_s- t_a) \qquad (2)$$

$$Q_{LH}=\rho\, L_e\, C_L\, U_{10}\,(q_s- q_a) \qquad (3)$$

where ρ air is density, L_e is the latent heat of vaporization, C_p is the specific heat capacity of air at constant pressure, C_L and C_S are latent and perceptible heat transfer coefficients, U_{10} is the wind speed at 10 m above sea level, t_s and t_a are respectively air temperature near the sea level and temperature at 10 meters above sea level, q_s and q_a are the specific humidity of the air just above sea level and the specific humidity of the air at 10 meters above sea level, respectively. Equations 2 and 3 have been often used in previous studies with more appropriate estimates of transfer coefficients [7, 8, 9, 10, 11, 12].

Due to the availability of essential information for calculating two important parameters Q_{SH} and Q_{LH}, analyzing these two parameters and comparing them between several oceans (or seas) are key findings in determining changes in weather and climatic conditions. These two parameters also play essential roles in atmospheric and sea coupling models, which can effectively determine climate change [1, 5, 13]. It should be noted that Q_{LH} values over the ocean are significantly higher than Q_{SH} values [5].

One of the critical areas for studying heat flux distribution is the northern Indian Ocean (NIO), which is affected by climate change and is widely included in the Arabian Sea (AS), Gulf of Oman (GO), and Persian Gulf (PG). Any change of these environments can change the climate of the surrounding areas.

The study area and its coordinate are shown in Figure.1 and Table 1 respectively. Study of surface fluxes distributions are important in the NIO because of the special and unique conditions of this region. Due to the fact that this area is located in a hot and dry region and is mainly enclosed between lands. Some previous study has shown a heat loss by Q_{LH} up to about 671 (Wm^{-2}) due to the occurrence of dry winds that could also cause a significant amount of dust in the atmosphere [14, 15]. The 35 years of wind rose showed in several locations of the NIO for 35 years are shown in Figure. 1 (references of this data are ECMWF-ERA5)[1].

The Shamal wind is the most energetic wind in the Persian Gulf region. It is a strong northerly to the northwesterly wind that blows along the axis of the Persian Gulf in both winter and summer. The winter Shamal winds occur mainly from November through March, while the summer Shamal winds with much less important in terms of wind strength, accompanying weather conditions and that are generally persistent from May to early July. Moreover, south to southeasterly Kaus winds often blows which are considered local winds [15,16]. Also, the prevailing wind direction of the GO and the AS is (following Figure. 1) from the west and southwest which is significant different from the wind regime in the PG. In addition, the mean rate of evaporation in these areas is reported up to be about 5 meters per year [17, 18].

Table 1. Coordinates of the study area

	Long(°)	Lat(°)
NIO	48-74	10-31
PG	48-56	24-31
GO	56-60	22-27
AS	51-74	10-22

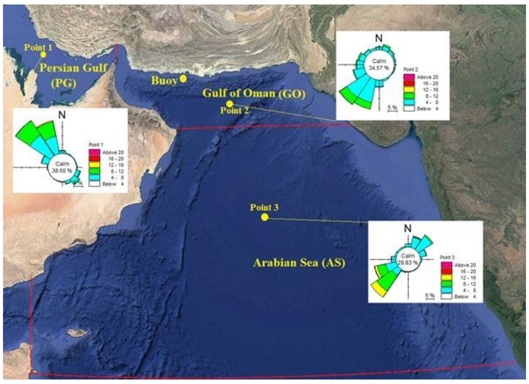

Figure 1. Some windroses in the study area (ECMWF- ERA5) and location of meteorological measurement data in PG.

The wind speed and direction affect climate conditions directly and indirectly. The results showed that the wind direction slightly affects evaporation, but the wind speed can significantly change the rate of evaporation in the PG [19] as the environment is dry. Climate change affects the wind field and the wind mostly produces sea waves [20]. Hence evaluating the wind field is important for calculating surface heat fluxes.

---

[1] ECMWF Reanalysis 5th Generation

As seen in Eq. 2 and 3, Q_{SH} and Q_{LH} depend on U_{10} directly and indirectly, as the wind can significantly affect the temperature and humidity values, and consequently, they influence the Q_{SH} and Q_{LH} indirectly. Therefore, the relationship between the wind and Q distribution is one of the most important issues in climate impact determination [13, 21, 22]. The effect of wind, which is studied as the effective parameter for surface wind stress (τ), is calculated as follows:

$$\tau = \rho\, C_D\, (U_{10})^2 \qquad (4)$$

where C_D is the drag coefficient which is somehow depends on wind speed. In this paper, using meteorological data and bulk experimental formula, the values of Q_{SH} and Q_{LH}, and τ for the three parts of the AS, GO, and PG, which have not been discussed separately before (As far as the authors know), have been calculated and compared for the three reigns. For this purpose, ECMWF[2] and NCEP[3] meteorological reanalysis data are used in this study. First, these data are validated by measurement data in a GO location which is shown in Figure 1, and then more appropriate data set has been selected for further analysis.

2. Datasets and Method

The more appropriate estimation of heat flux leads to more accurate results in the climate study. Therefore, the quality of ECMWF and NCEP meteorological data should be evaluated. In this study, a meteorological measurement station in the GO (Figure. 1) is applied to estimate the Q values. This data is used to evaluate the ECMWF and NCEP reanalysis data in NIO. The average monthly values of Q_{SH}, Q_{LH}, and τ are calculated based on measurement and reanalysis of meteorological data at the buoy location (point 2, for 2013). Figure. 2 (a) and (b) show respectively the comparison of monthly mean values of Q_{LH} and Q_{SH} calculated by Buoy, ECMWF, and NCEP meteorological data. It should be noted that the positive values in this paper represent heat transfer from air to water and the negative values indicate heat transfer from water to air. According to this graph, Q_{LH} values from ECMWF reanalysis and buoy data are significantly higher than Q_{SH} values. As seen from the buoy values, the maximum value of Q_{LH} is about -450 (Wm^{-2}), which occurs in July. In the same month, the amount of Q_{SH} is about +30 (Wm^{-2}). In fact, positive buoy Q_{SH} is associated with the exchange of heat from the air to water.

Figure. 2 (c) shows the comparison of monthly mean values of τ calculated by Buoy, ECMWF, and NCEP meteorological data. The value of τ was the highest in July (about 0.04 Pa), and the average values of τ are about 0.02 Pa. Table 2 also shows the average annual values of Q_{SH}, Q_{LH}, and τ. As seen in this table, the annual average of Q_{LH}, Q_{SH}, and τ are about 276 (Wm^{-2}), 19.8 (Wm^{-2}), and 0.03 (Pa), respectively. In this study, the monthly mean values of Q_{SH}, Q_{LH}, and τ are also calculated based on the ECMWF and NCEP meteorological data at the buoy location for 2013, and their variation are plotted in Figure.2. According to the results, it is clear that the ECMWF reanalysis data is more consistent with the Buoy data and its evident for all three parameters Q_{SH}, Q_{LH}, and τ. The error index of ECMWF reanalysis data for calculating Q_{SH}, Q_{LH}, and τ are about 30, 2, and 60%, respectively. However, the error-index of acquired NCEP reanalysis data is about 99, 9, and 120%, respectively. Based on the error-index, it is clear that the ECMWF reanalysis data in the buoy location is more accurate than the NCEP acquired reanalysis data. Therefore, ECMWF reanalysis data (with a resolution of 0.25 degrees) is used to calculate Q_{SH}, Q_{LH}, and τ in the whole study area.

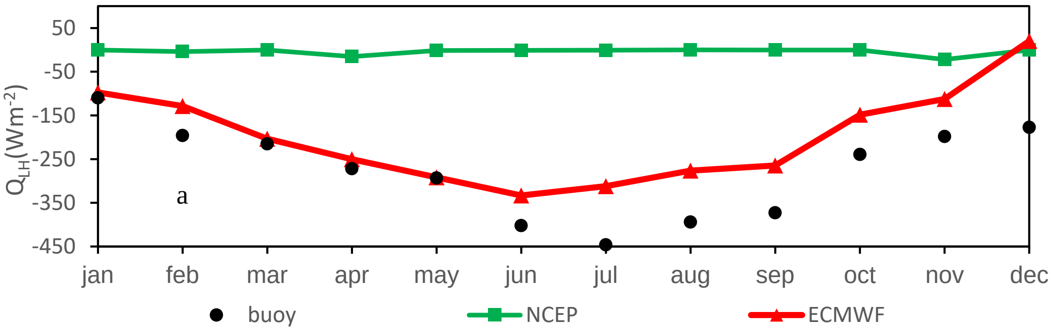

---

[2] European Center Medium-Range Weather Forecasts

[3] National Center for Environmental Prediction Final

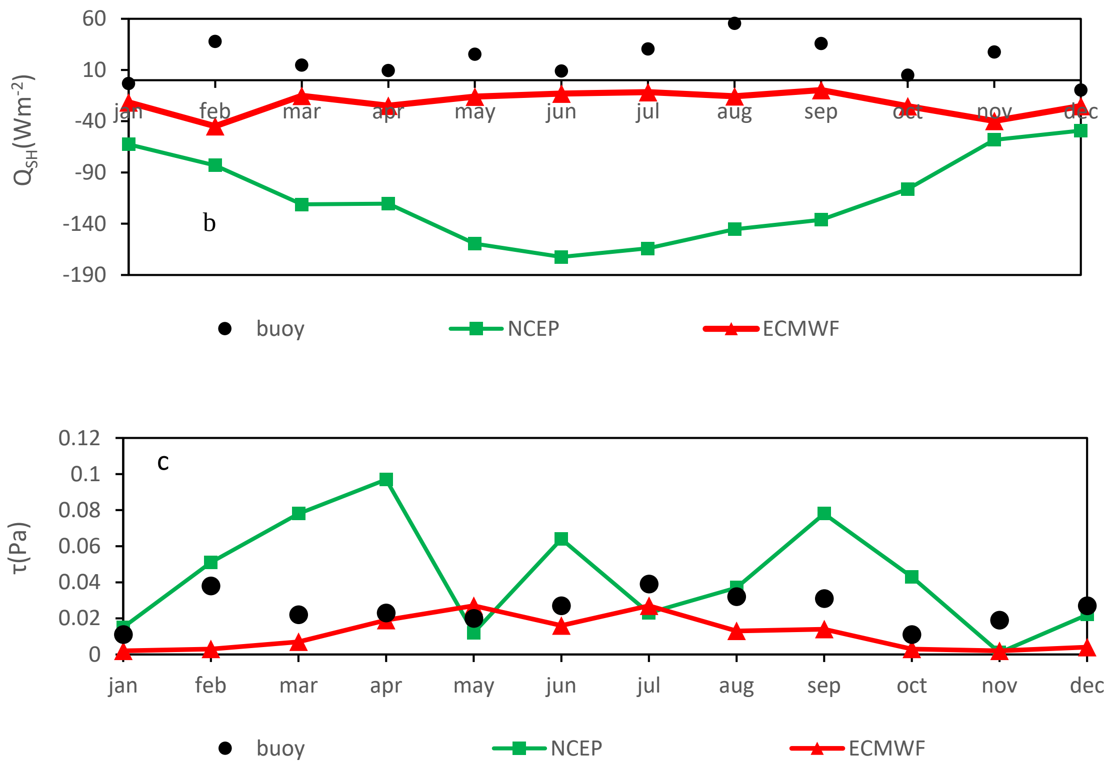

Figure 2. Monthly mean of Q_{LH} (a), Q_{SH} (b), and τ (c) at buoy location in 2013

Table 2. Monthly mean of Q_{LH}, Q_{SH} (in Wm^{-2}), and τ (in Pa) at the measurement location for 2013

	ECMWF			NCEP			Measurement		
	Q_{LH}	Q_{SH}	τ	Q_{LH}	Q_{SH}	τ	Q_{LH}	Q_{SH}	τ
Mean	-199.8	-21.9	0.01	-42.18	-77.7	0.04	-276.4	19.8	0.03

3. Results and Discussion

In this study, 14-year ECMWF reanalysis data were used to calculate the values of Q_{LH} and Q_{SH}, and τ for the NIO and separately for the AS, GO, and PG regions. The values were calculated and compared monthly (average per month over 14 years), seasonal average (average per season over 14 years), and the annual average for AS, GO, and the PG regions.

3.1. Monthly Variability

Figure. 3 shows the monthly mean values of Q_{LH} over the study period for AS, GO, and the PG regions. As shown in this Figure, the minimum, maximum, and average Q_{LH} parameter changes for each month are shown as Box and Whisker diagrams during the study period. The values of Q_{LH} show heat exchange from the sea to the atmosphere. The highest amount of Q_{LH} was recorded in December and January when it was about 200 (Wm^{-2}) in the PG. Also, the minimum value of this parameter is about 60 (Wm^{-2}), which occurs in August and September in the GO. The trend of Q_{LH} variation is the same for the three regions of the AS, GO, and the PG; the amount of Q_{LH} decreases from December to April and then increases from April to June. Then, the amount of Q_{LH} decreases until September, and finally, Q_{LH} increases until December. These changes are the same for the three regions. It is observed that Q_{LH} in the PG is higher than those of the GO, and the GO values are higher than those of the AS from January to June. This pattern has been observed irregularly for other months, with Q_{LH} in the GO being lower than those of the PG and the AS in July, August, and September.

Figure. 4 shows monthly mean values of Q_{SH} over the study period. The results show that heat transfer is from the sea to the atmosphere in the AS. For the PG and GO, Q_{SH} transfers from the atmosphere to the sea in

June, July, August, and September; in other months, heat transfer via Q_{SH} is from the sea to the atmosphere. In other words, the transfer of Q_{SH} between the sea and the atmosphere for the AS in the four months of June, July, August, and September is different from the PG and GO. The range of Q_{SH} with a range of -20 to +20 for the NIO is much lower than those of the Q_{LH} values. It is also observed that the slope of Q_{SH} changes from December to July, which is increasing, that is different from the slope of Q_{SH} changes from July to December, which is decreasing.

Figure 5 shows the monthly mean values of τ over the study period. The trend of τ variation is the same as Q_{SH} at NIO, and it seems that there is a strong correlation between these two parameters. Moreover, the changes of τ in the AS are different from those of the PG and the GO in the four months of June, July, August, and September. In other words, τ in the AS is less than those of the PG and the GO in these four months.

In this section, the monthly average of Q_{LH} and Q_{SH}, and τ in three AS, GO, and PG regions have been studied. Examination of the results shows that the trend of monthly changes in Q_{SH}, τ is quite similar. A strong correlation has been observed between the studied parameters in the NIO. As the τ increases, the amount of Q_{LH} decreases; this means that heat transfer from sea to air through Q_{LH} is reduced in summer compared to winter. The heat exchange from the sea to the atmosphere changes through the Q_{SH} in summer with the increase in τ; in this way, Q_{SH} is transferred from the atmosphere to the sea in summer and is from the sea to the atmosphere in winter.

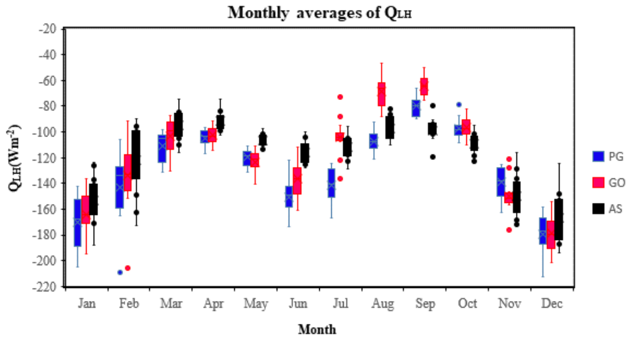

Figure 3. Monthly mean of Q_{LH} in the study period of the AS, GO, and PG

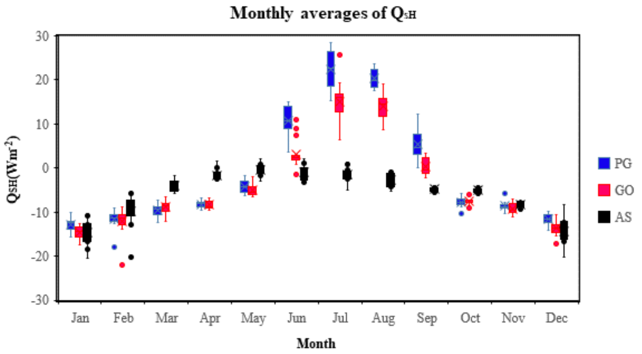

Figure 4. Monthly mean of Q_{SH} in the study period of the AS, GO, and PG

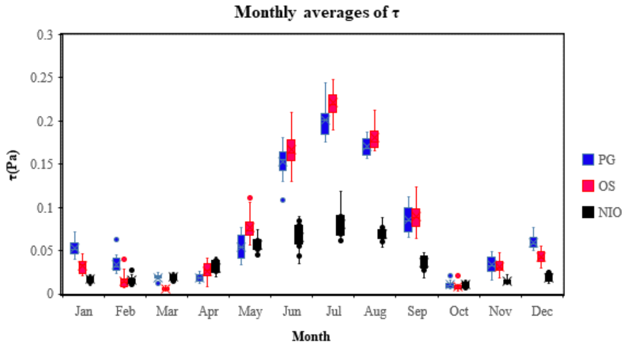

Figure 5. Monthly mean of τ in the study period of the AS, GO, and PG

3.2. Seasonal Variability

Figure 6 shows the seasonal mean Q_{LH} values over the study period. As shown in this Figure, the minimum, maximum, and mean values of the Q_{LH} changes for each season. The seasonal study of Q_{LH} shows that the average Q_{LH} varies in different seasons and the heat transfer is from the sea to the atmosphere by this means. The highest amount of Q_{LH} was recorded in the fall, which was about 150 (Wm^{-2}). Also, the minimum value of this parameter is about 80 (Wm^{-2}), which occurs in winter in the GO. According to Figure. 6, heat transfer from the sea to the atmosphere in the form of Q_{LH} is in winter and spring in the PG has been more than those of the GO and the GO, which is still more than that of the AS. In summer, heat transfer from the sea to the atmosphere via Q_{LH} is observed in the PG more than the AS, and in the AS it is more than that of the GO. Also, the amount of Q_{LH} in autumn is almost the same for the three studied areas.

Figure. 7 shows the seasonal mean values of Q_{SH} during the study period. The seasonal review of Q_{SH} shows that the mean Q_{SH} varies seasonally, similar to what is discussed in the monthly changes. Heat transfer through the Q_{SH} in the AS has always been from the sea to the atmosphere. On the other hand, for the PG and the GO, heat transfer through the Q_{SH} has been from the atmosphere to the sea in the summer.

Figure. 8 shows the seasonal mean values of τ over the study period. In general, τ values in the PG and the GO are higher than that in the AS. In summer, stronger winds are observed in both the PG and the GO. This could be the reason for Q_{SH} summer heat transfer which is from the atmosphere to the sea. For the other three seasons, the heat transfer is Q_{SH} from the sea to the atmosphere. Increase in wind stress also affects the intensity of Q_{LH}. In fact, with increasing wind stress in summer, the value of Q_{LH} also decreases, may be to the waves breaking sheltering effect that can reduce the surface evaporation coefficient at stronger winds.

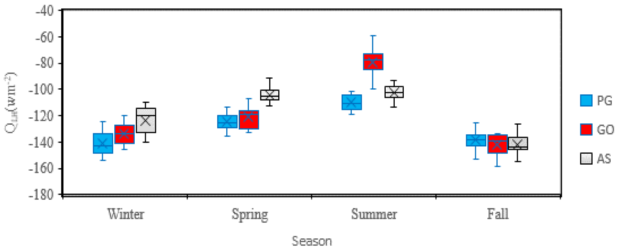

Figure 6. Seasonal mean Q_{LH} in the study period of the AS, GO, and PG

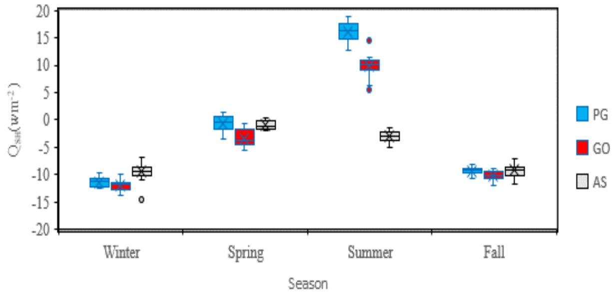

Figure 7. Seasonal mean Q_{SH} in the study period of the AS, GO, and PG

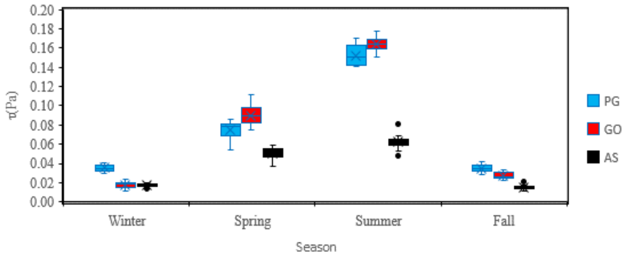

Figure 8. Seasonal mean τ in the study period of the AS, GO, and PG

3.3. Annual Variability

Figure. 9 shows the annual mean Q_{LH} values over the study period. As shown in Figure. 9, the annual average Q_{LH} in the PG is higher than the GO and the AS. The Q_{LH} transfer from the sea to the atmosphere in the PG is more than those of the two basins of the GO and the AS, which can be due to the almost being semi-closed environment of the PG with shallow depth, compared to the GO and the AS, which provides more heat transfer to the atmosphere in the shallow PG area. Of course, higher wind speeds in PG relative to those of the GO and the AS are also influential. Since the PG air is desert and dry [1], the wind brings dry air to the PG and reduces humidity. Decreased humidity leads to more evaporative heat transfer from the sea to the atmosphere.

Figure. 10 shows the average annual Q_{SH} values over the study period. As shown in Figure. 10, in all years, the annual average Q_{SH} in the PG is lower than that of the GO, and in the GO it is still lower than that of the AS, which can be due to strong winds in the PG and to s0ome extent, in the GO.

Figure. 11 shows the annual mean values of τ over the study period. In general, τ values in the PG and the GO are higher than that in the AS. The mean value of τ recorded in the PG and the GO are almost twice that of the AS. Furthermore, τ combined with specific PG conditions (shallow depths and semi-closed space) has created unique climate conditions in the NIO area.

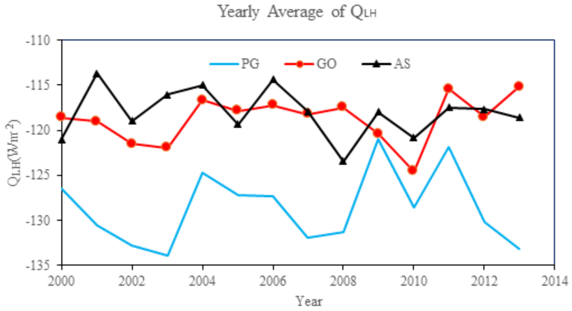

Figure 9. Annual mean Q_{LH} in the study period of the AS, GO, and PG

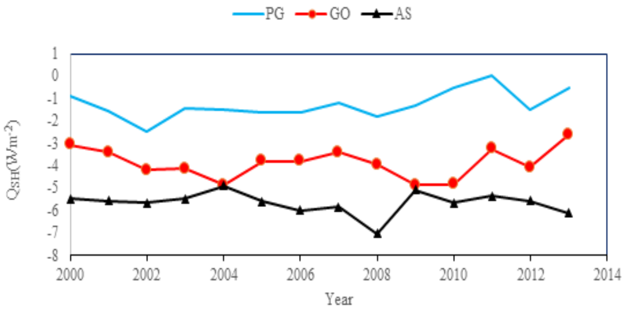

Figure 10. Annual mean Q_{SH} in the study period of the AS, GO, and PG

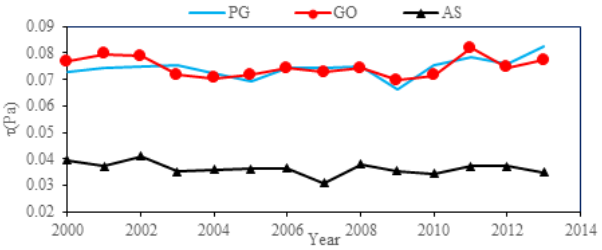

Figure 11. Annual mean τ in the study period of the AS, GO, and PG

4. Conclusions

This paper investigates the value of two crucial heat transfer parameters between the sea surface and the atmosphere, namely Q_{LH}, and Q_{SH}, in the NIO area. For a more detailed study, this region has been divided into three sub-regions: the PG, GO and AS. The values of Q_{LH} and Q_{SH} have been calculated and compared with the help bulk transfer formula on a monthly, seasonal and annual averages in these three regions. In order to calculate the mentioned fluxes, meteorological parameters such as wind speed, air humidity difference between climate levels, and temperature difference between climate levels are used. Observational measurements were used along with NCEP reanalysis data, leading to the following concluding points:

- Surface mean annual wind stress in the PG and the GO are usually higher than that in the AS.
- Considering that the τ in the PG and to some extent, in the GO are higher than that of the AS, and on the other hand, since the PG air is usually desert and dry, the wind brings the dry air to the PG and reduces the humidity. Hence, decreased humidity leads to more Q_{LH} transfer in PG from the sea to the atmosphere is larger than those in the AS and the GO.
- In winter, heat transfer from the sea to the atmosphere via Q_{LH} in the PG has been more than that of the GO and the GO values are more than that of the AS. In spring, heat transfer is mainly via Q_{LH} from the sea to the atmosphere in the PG and in the GO, and are almost "similar" and more than that of the AS. In summer, heat transfer from the sea to the atmosphere via Q_{LH} in the PG is also more than that of the AS, and that of the AS and is more than that of the GO.
- The Q_{SH} in the AS has always been from the sea to the atmosphere, but the PG and the GO in summer it has been from the atmosphere to the sea. Strong winds could be the reason for Q_{SH} summer heat transfer from the atmosphere to the sea. For the other three seasons, the heat transfer by Q_{SH} is from the sea to the atmosphere. Increased wind stress also affects the value of Q_{LH}. In fact, with increasing τ in summer, the intensity of Q_{LH} also decreases that may be due to sheltering effects of wind waves at stronger winds.
- Although it is difficult to fully understand the relationship between the parameters studied in this study, however, monsoonal and seasonal circulations in the area seem to determine the observed fluxes in the study area.

Acknowledgments

We acknowledge ECMW and NCEP for making available the data used in this study.

8. References

[1] Al Senafi, F., Anis, A. and Menezes, V. (2019). *Surface heat fluxes over the Northern Persian Gulf and the Northern Red Sea: evaluation of ECMWF-ERA5 and NASA-MERRA2 reanalyses*. Atmosphere,. 10(9): p. 504.

[2] Vissa, N.K., Satyanarayana, A.N.V. and Prasad Kumar, B. (2013). *Comparison of mixed layer depth and barrier layer thickness for the Indian Ocean using two different climatologies.* International J. of Climatology, 33(13), pp.2855-2870.

[3] Kara, A.B., Rochford, P.A. and Hurlburt, H.E., (2003). *Mixed layer depth variability over the global ocean.* Journal of Geophysical Research: Oceans, 108(C3).

[4] Mullah Esmailpour, S., Mehdizadeh, M., Hassanzadeh, E., Khalilabadi, M. (2018). *Determination of the depth of the mixed layer and investigation of the barrier layer during the summer and winter monsoon in the North Indian Ocean*. Hydrophysics, 3(2), pp.41-55

[5] Stewart, R. H. (2008) *Introduction to physical oceanography*, Robert H. Stewart.

[6] Cayan, D. R. (1992). *Latent and sensible heat flux anomalies over the northern oceans: Driving the sea surface temperature*. Journal of Physical Oceanography, 22(8), pp.859-881.

[7] Singh, R., Kishtawal, C.M., Pal, P.K. and Joshi, P.C. (2006). *Surface heat fluxes over global oceans exclusively from satellite observations.* Monthly weather review, 134, (3), pp.965-980.

[8] Banks, R.F., Bourassa, M .A., Hughes, P., O'Brien, J.J. and Smith, S.R. (2006). *January. Variability of surface turbulent fluxes over the Indian Ocean*. In 14th Conference on Interactions of the Sea and Atmosphere.

[9] Yu, L. and Weller, R.A. (2007). *Objectively analyzed air–sea heat fluxes for the global ice-free oceans (1981–2005).* Bulletin of the American Meteorological Society, 88(4), pp.527-540.

[10] Yu, L., Weller, R.A. and Sun, B. (2004). *Improving latent and sensible heat flux estimates for the Atlantic Ocean (1988–99) by a synthesis approach.* Journal of Climate, 17(2), pp.373-393.

[11] Yu, L., Jin, X. and Weller, R.A. (2007). *Annual, seasonal, and interannual variability of air–sea heat fluxes in the Indian Ocean*. Journal of climate, 20(13), pp.3190-3209.

[12] Khademi, I., Akbarinasab, M., Bidokhti, A.A. and Khalilabadi, M.R. (2017). *Numerical calculation of Prandtl number in water column stratification in the Strait of Hormuz.* Journal of Marine Science and Technology, 16(3), pp.14-26.

[13] Ghose, S.K., Swain, D., Mathew, S. and Venkatesan, R. (2021). *Seasonal variability of air-sea fluxes in two contrasting basins of the North Indian Ocean*. Dynamics of Atmospheres and Oceans, 93, p.101183.

[14] Zolina, O., Dufour, A., Gulev, S.K. and Stenchikov, G. (2017). *Regional hydrological cycle over the Red Sea in ERA-Interim.* Journal of Hydrometeorology, 18(1), pp.65-83.

[15] Al Senafi, F. and Anis, A. (2015). *Shamals and climate variability in the Northern Persian Gulf from 1973 to 2012.* International Journal of climatology, 35(15): p. 4509-4528.

[16] Rao, P.G., Hatwar, H.R., Al-Sulaiti, M.H. and Al-Mulla, A.H. (2003). *Summer shamals over the Persian Gulf*. Weather, 58(12), pp.471-478.

[17] Thoppil, P.G. and Hogan, P.J. (2010). *Persian Gulf response to a wintertime shamal wind event. Deep Sea Research Part I*: Oceanographic Research Papers, 57(8): p. 946-955.

[18] Rezaei-Latifi, A. and Hosseinibalam, F. (2015). *An estimate of the surface heat fluxes transfer of the Persian Gulf with the overlying atmosphere.* Journal of Radiation Research and Applied Sciences, 8(3), pp.354-361.

[19] Mahpeykar, O. and Khalilabadi, M.R. (2021). *Numerical modelling the effect of wind on Water Level and Evaporation Rate in the Persian Gulf.* International Journal of coastal and offshore engineering, 6(1), pp.47-53.

[20] Pourali, M. and Kavianpour, M.R. (2023). Variation of monthly exploitable wave energy in the Gulf of Chabahar under a high-resolution CMIP6. International Journal Of Coastal, Offshore And Environmental Engineering, 8(1), pp.16-25.

[21] Tomita, H. and Kubota, M. (2004). Variability of surface heat flux over the Indian Ocean. Atmosphere-ocean, 42(3): p. 183-199.

[22] Shinoda, T., Hendon, H.H. and Glick, J. (1999). Intraseasonal surface fluxes in the tropical western Pacific and Indian Oceans from NCEP reanalysis. Monthly weather review, 127(5), pp.678-693.

INTERNATIONAL JOURNAL OF
COASTAL, OFFSHORE & ENVIRONMENTAL ENGINEERING
IJCOE Vol.8/No. 2/Spring 2023 (48-55)

Available online at: www. Ijcoe.org

Caspian rapid Sea level fluctuation and intensity of shorelines displacement in the Gomishan Lagoon

Homayoun Khoshravan[1], Parisa Poursafari Yekrang[2*],Payam Alemi Safaval[3]

[1] *Associated professor of the water research institute, Caspian Sea national research & study center; Tehran, Iran,*
[2*] *Lab Expert , Water Engineering Department, Guilan University & Ph.D Candidate in Environmental Engineering -Water and Wastewater,Tehran University; Parisa.Poursafari@ut.ac.ir*
[3]*MSc Remote Sensing and GIS, Geological Survey & Mineral Exploration of Iran*

ARTICLE INFO

Article History:
Received: 16 Feb. 2023
Accepted: 23 May. 2023

Keywords:
Sea level changing
GIS and RS
Shoreline displacement
Wetland
Regression

ABSTRACT

Coastal displacement due to hydrodynamic factors and changes in sea level has serious impacts on adjacent ecosystems, economic infrastructure, and human communities. Rapid fluctuations in the Caspian Sea level have created unstable conditions for coastal environments since the twentieth century. This study aims to evaluate the amount of shoreline displacement and Morpho- logical changes in the shoreline at the location of the Gomishan wetland between 1995 and 2019 and its impact on this international wetland. To this end, by processing Landsat satellite Images in the mentioned years using the Normalized Difference Water Index (NDWI), the water body was separated from non-water to extract the shoreline. The results show a significant displacement of the shoreline ranging from -136 to -1072 meters downstream of the Gorganrud River estuary in the southern region and a forward displacement of the shoreline inside the sea from 135 to 7781 meters, with most of the displacement occurring in the northern section. The studied area was classified into three groups based on the shoreline displacement (high, medium, and low). The results show that the northern part of the Gomishan wetland experienced the highest amount of shoreline displacement, and the amount of shoreline displacement gradually decreased in the central and southern regions. Additionally, the results show a significant relation with the period of decreasing the Caspian Sea level during the study period.

1. Introduction

The investigation of the impact of sea level fluctuations on coastal regions holds significant importance [1]. The Caspian Sea, which spans an area of 436,000 square kilometers, is recognized for its rapid water level changes [2]. Coastal Wetlands situated along the southern shores of this lake are considered to be one of the most crucial ecosystems in the region. During the late Holocene period, the growth of the sandy spit along the coastline of the Caspian Sea has created suitable conditions for the creation of Gomishan Lagoon [3].The Gomishan International Wetland, formerly encompassing an area of 177 square kilometers in 1995, played a vital role in the environmental landscape of the southeastern coast of the Caspian Sea. The stability and water depth of this lagoon were closely linked to fluctuations in the Caspian Sea's water level, according to Jeihouni et al. (2019). This site was once a completely natural coastal wetland along the Caspian Sea and provided vital support to numerous vulnerable bird species, with bird populations sometimes exceeding 150,000, as highlighted by [4].Gomishan Lagoon and Gorgan Bay have progressed to complete drought many times during the geological period, but the increasing oscillating phases of the Caspian Sea water level have created conditions for its regeneration and reconstruction [5,2].One of the most important distinctions between the Caspian Sea and other open seas lies in their varying sea level patterns. Specifically, While the Caspian Sea has experienced a decreasing and increasing trend, according to the obtained data, the water level of the open seas is continuously increasing [6].The Caspian experienced a notable ascent of 2.4 meters. Subsequently, from 1995 to 2019, its level declined by 1.5 meters (Figure 1).

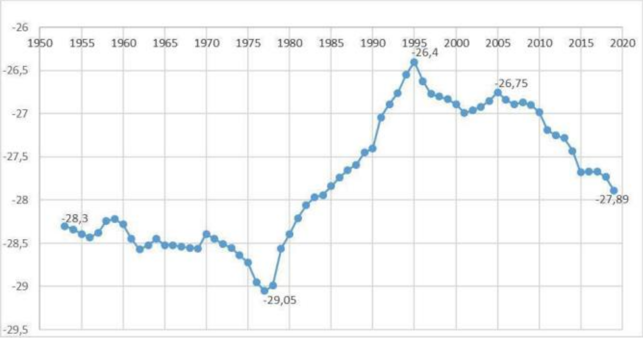

Figure 1. Caspian Sea levels with respect to the high sea level [7]

Coastal displacement has a direct impact on various economic infrastructures, including commercial ports, fishing docks, thermal power plants, and coastal tourism facilities [8,9], and with time, heavy damages are caused by the hydrodynamic erosion factors of the sea (coastal currents and waves) and sea level fluctuations have affected them [10]. The Caspian Sea coast is no exception to this rule and has undergone serious changes and extensive environmental challenges due to fluctuations in sea level, which is sometimes more than a hundred times faster and sometimes in the opposite direction of the oceans[11,12,13].Since the twentieth-century Fluctuations in the water level of the Caspian Sea have caused the deformation of coastal processes and the joint impact of the fluctuating phases of the Caspian Sea and human factors, conditions of sedimentation regime change, shoreline displacement, and the development of erosion phenomena on the coast [14,12,15].The economic consequences 250 cm increase in the Caspian Sea water level during the period 1978-1995 are estimated at more than $ 17 billion [16].The rapid decline of the Caspian Sea water level during the periods 1930-1978 and 1995-2019 has led to major deformation of natural habitats, extinction of coastal Lagoons, and the impact of centralized economic capacity in coastal areas [17,12]. As the largest reservoir on the eastern shore of the Caspian Sea and with a very high ecological value, Gara Baghaz Bay completely dried up during the eighties of the twentieth century, due to the increasing decline in the water level of the Caspian Sea and losing its lagoon ecosystem services. As a result, many economic and social damages were inflicted on the former Soviet government [16]. At present, about 30% of the area of Gorgan Bay and a large part of Miankaleh Lagoon has dried up due to the decrease in water level in the Caspian Sea, and its important coastal habitats have been destroyed [16].The shoreline is the physical boundary between land and water and due to its dynamic nature, it changes continuously over time [18,19,20].As a result, maps illustrating changes in shoreline and coastal areas are critical in coastal hazard assessment [21].The main purpose of this research is to calculate the intensity of variability of shorelines in different regions of Gomishan coastal Lagoon with specific emphasis on the effects exerted by a reduction in water levels within the Caspian Sea between 1995 and 2019. In this research, to achieve this goal, the processing of Landsat satellite Images in 1995 and 2019 was used to calculate the amount of movement and change of the beach morphology by extracting the shorelines in these years. The coastal habitats of Gomishan Lagoon, Gorgan Bay, and Miankala Lagoon possess a significant conservation value [15]. Furthermore, it is worth noting that Gomishan International Lagoon has been recognized as a biosphere reserve and Life Sanctuary by the Ramsar Convention ,and having been registered in 1975 [22]. The expansion of coastal plants along the coast of the Caspian Sea and the coast of Gorgan Bay and Gomishan Lagoon with high diversity and species richness has led to the creation of important habitats including salt marshes, salt marshes and freshwater along with sandy grasslands and forests. Pomegranate and Gaz shrubs are highly sensitive and physically vulnerable to changes in the water level of the Caspian Sea [15,13]. In addition, the importance of the eastern and southeastern parts of Gorgan Bay, such as Bandar Turkmen and Bandar Gaz, is very high in tourism and fishing activities, and the safe connection of Gorgan Bay and the Caspian Sea is considered an important strategic criterion for the protection of economic, social and environmental infrastructure [11,23].The water level of the Caspian Sea increased by 250 cm during the years 1978-1995 and caused the destruction of a large area of habitats belonging to the terrestrial ecosystems of the Caspian Sea (Gomishan Lagoon and Gorgan Bay) and instead, the Miankala coastal Lagoon and Gorgan Bay added [13]. The decrease in the water level of the Caspian Sea by 150 cm since 1995 caused the drying of a large part of the western end of the Gorgan Bay and the northeastern part of the Miankala Lagoon, and as a result, the coastal Lagoons of Miankala and Gomishan dried up and more than 30% decreased from the area of Gorgan Bay [20].Satellite data and remote sensing techniques make it possible to identify and monitor various features of the Earth's surface. Therefore, they identify a wide range of ecological and environmental components [24,25,26,27].As a result, numerous studies have been undertaken using remote sensing and geographic information systems to investigate the transformations in shorelines and their influence on coastal wetland ecosystems.Domazetović et al., 2021 used NDWI to extract the shoreline [28]. Alcaras et al., (2020), also evaluated the function of NDWI as favorable for this purpose [29], and Saeed and Fatima, 2016 extracted the beaches of Dubai by using NDWI. Qureshi et al.,(2020),evaluated the ecological changes in Gomishan wetland by using remote sensing. They reported the most important factor that naturally affects the surface ecological characteristics of Gomishan Lagoon is the fluctuation of the Caspian Sea water level, which leads to the decrease and increase of the water level of the Lagoon [30]. The result of Jeihouni et al., (2019), also emphasizes the direct impact of the Caspian Sea water level on Gomishan Lagoon [2]. Khoshravan et al., (2022), using remote sensing and GIS, investigated the intensity of changes in the shorelines of the Caspian Sea coast in the area of the coast of Sefidroud Delta and Gorgan Bay [31].Ghaderi and Rahbani, (2020), analyzed the changes in Bandar Abbas shoreline using remote sensing and GIS [32].

2. Research method

2.1 Study area

Gomishan Wetland is located in the extreme southern part of the eastern coast of the Caspian Sea, along the western border of the Turkmen Steppe plains. It covers a vast area of 17,700 hectares and is situated at a depth of 27 meters below the level of the open sea. The wetland's coordinates are 37° 09´ to 37° 20´ N and 53° 54´ to 53° 58´E f. It takes on the form of a relatively narrow strip running along the southeastern shores of the Caspian Sea in a north-south direction as shown in Figure 2.

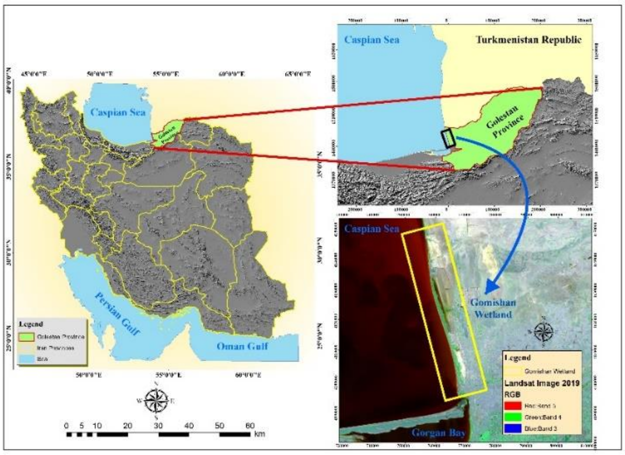

Figure 2. Study area

2.2. Methodology

In the present study, geometric correction, radiometric and atmospheric corrections were initially performed to determine the shoreline changes using Landsat, colour composite of 5,4,3 bands for the Image of 1995 and 6,5,4 bands for the Image of 2019 was created. Furthermore, NDWI (Normalized Difference Water Index) was used to separate the water body from non-water.NDWI is used for monitoring changes related to water content in water bodies. Since water bodies strongly absorb light in the visible to near-infrared range of the electromagnetic spectrum, NDWI uses bands in the green and near-infrared range to highlight water bodies. NDWI can effectively increase information related to water in most cases. It is sensitive to natural surfaces and leads to an overestimation of water. Water bodies with low reflectance are only reflected in the visible part of the electromagnetic spectrum In their liquid state, water bodies usually have high reflectance in the blue spectrum (0.4-0.5 micrometers) compared to the green (0.5-0.6 micrometers) and red (0.6-0.7 micrometers) spectra. Values greater than 0.5 are usually associated with water. Vegetation cover usually has much smaller values and man-made areas have values between zero and 0.2. NDWI was developed by McFeeters in 1996 to enhance water-related features of developed landscapes. This index uses near-infrared (NIR) and shortwave infrared (SWIR) bands [34,35,36].NDWI could be calculated by using Eq.(1):

$$NDWI=\frac{Green\text{-}NIR}{Green+NIR} \qquad (1)$$

where in Eq.(1) $Green$ and NIR represent the respective reflectance values of green light and near-infrared light. Following the extraction of shorelines from satellite Imagery for the purpose of calculating shoreline displacement, the shoreline in 1995 was selected as the baseline, and 92 transects were drawn from it to the shoreline in 2019. The Digital Shoreline Analysis System (DSAS) was used to perform computations for shoreline rates of change. DSAS is one of the reliable tools for quantifying the rate of shoreline changes during a particular period, which was developed by USGS and has been used in many similar projects during the last two decades [33]. This methodology facilitated the determination of both the displacement and morphological changes of the shoreline. Moreover, in order to estimate the extent of erosion and sedimentation within the Gorganrud River estuary, the shorelines from the various studied years were connected. Subsequently, by analyzing the eroded and sedimented areas, their respective surface areas were calculated (Figure3).

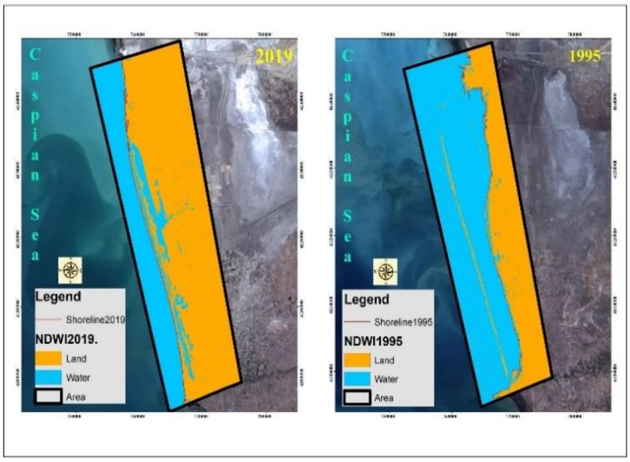

Figure 3. Shoreline extraction based on applications of NDWI, 1995&2019

3. Results

The results of satellite image processing using NDWI indicate a significant displacement and morphological changes of the southeastern shoreline of the Caspian Sea in the Gomishan Wetland area, which has led to the degradation of this valuable ecosystem. The analysis of shoreline extraction in 1995 and 2019 shows that the rate of shoreline changes in the study area is not uniform, and the displacement of the shoreline increases from south to north between the Turkmen port and Gomishan, with the exception of the Gorgan River estuary area, where shoreline regression of (-136 to -1072) meters is observed in the Khajeh Nafas region. The maximum shoreline displacement of 7.8 kilometers occurred in the northern part of the Gomishan Wetland, with a length of 7781 meters. According to the leveling data (Figure 1). The decrease in the water level of the Caspian Sea has been the main factor in recent years, leading to the drying out of the water body and shoreline of this coastal wetland. (Figure 4) depicts the amount of shoreline displacement in the study period, and (Figure 5) represents the number of changes based on the south-to-north transects drawn in the study area. The results of the field observations show that the Gomishan Lagoon has completely dried up, and its aquatic environment has turned into muddy areas (Figure 6). Over time, the growth of Salicornia Europa species on these muddy sediments has transformed the environment into a salt marsh (Figure 7). The change from a lagoon sedimentary environment to mudflats and salt marshes has led to the deposition of different sedimentary facies over the coastal landforms.

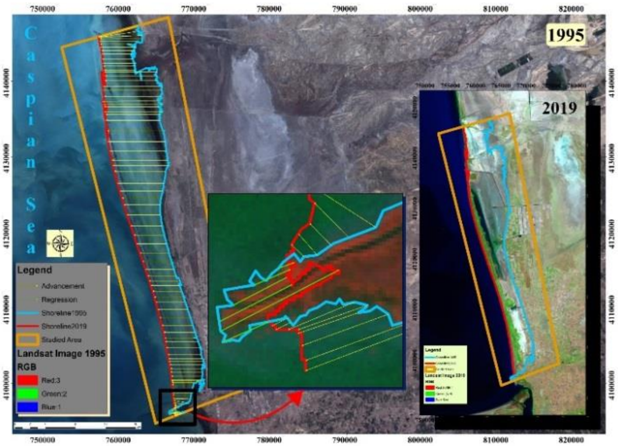

Figure4. The displacement of the shoreline of Gomishan Wetland , 1995 & 2019

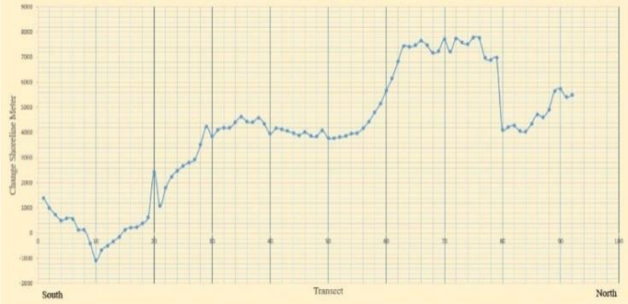

Figure5. The displacement of the shoreline of Gomishan Wetland from 1995 to 2019

landforms. The drying up of the lagoon has resulted in the development of mud cracks in the silt-clay sediments of the past sedimentary environment. These mud cracks provide a substrate for the growth of Salicornia plants, which are adapted to dry and salty environments (Figure 7). The transition from aquatic ecosystems to land, coupled with the growth of coastal vegetation, has paved the way for domestic animals to graze. As a result, the fishing practices that were once common in this area have given way to animal husbandry (as shown in Figure 7). Field observations indicate that the sedimentary environment changes from mudflats to sandbanks when moving from east to west along the edge of the Caspian Sea (Figure 8). Additionally, (Figure 9) shows the surveyed data points.

4. Discussion

As stated in the results of this study, a significant difference in the rate of coastline retreat and advance is observed along the studied area, resulting in imbalanced morphological changes in different sections of the coast. As evident from the satellite image processing maps for 1995 and 2019, the coastline displacement shows an increasing trend from south to north, which may be due to a decrease in the slope of the northern coast in the studied area [37]. In addition, two influential factors have increased the rate of coastline advance: the Gorganrud River mouth carrying annual sediment and the sandy barrier of Bay Gorgan acting as a dam that reduces the force of coastal currents, has increased the rate of coastline advance in the southern section within the sea. The average rate of decline of the Caspian Sea water level during 1995-2019 was about 6 cm, and the water level of the Caspian Sea has decreased by 150 cm in the last 24 years [16]. The quantitative and qualitative impact of wetland and sand environments around Gorgan Bay during the mentioned time are very different, and with the process of wetland drying, terrestrial ecosystems have quickly replaced aquatic ecosystems [16]. The behavioral response of coastlines to sea level fluctuations depends on important natural criteria such as average shore slope, embankment width, type and texture of coastal sediments, rate of change in sea level, coastal landforms, the intensity of tidal currents, and the energy of the waves [38]. The rate of shoreline displacement in Gorgan Bay is also a function of the topography of the wetland bed and the dry coastal area, where the highest intensity of shoreline shifts occurred in the western and northeastern regions of Gorgan Bay [16, 8]. Gorgan

Bay and Gomishan Lagoon are suitable dynamic systems for analyzing the impact of Caspian Sea water level fluctuations on the environment of coastal areas [16]. In the past, Gomishan Lagoon was completely dried up due to the decrease in the water level of the Caspian Sea between the 1930s-1978, and now, similar hydro morphological conditions have occurred for Gorgan Bay [16, 8]. The forecast shows that under the scenario of decreasing Caspian Sea fluctuations, Gorgan Bay will move towards complete drought by 2023 due to the closure of its connection [39]. Studies by Khoshrovan et al. in 2019 have shown that changes in the water level of the Caspian Sea affect the extent of variation in the coastal habitats of Gorgan Bay.The sandy beaches of the southeastern margin of the Caspian Sea along the northeastern part of the Miankala Lagoon and the shallow marshes at the western end of Gorgan Bay have experienced the greatest changes between 1995-2019 [13]. During this time, the most important ecological events in Gorgan Bay and Miankala Lagoon were the conversion of coastal lagoons to salt marshes and the change of aquatic ecosystems to dry land [13].The fluctuations in the water level of the Caspian Sea also affect the extent of Gomishan Lagoon. Over the last three decades, a large area of Gomishan Lagoon has dried up, leaving only narrow marshes and salt marshes in some places. In 1994, Gomishan Lagoon was about 171 square kilometers in size, but by 2014, its area had decreased to 58 square kilometers, and it completely dried up in 2015 [2]. Previous studies have shown that seasonal changes in the water level of the Caspian Sea directly affect the hydrological regime of Gomishan Lagoon. For example, from January to July 2000, the area of Gomishan Lagoon increased from 130 to 165 square kilometers, equivalent to 35 square kilometers [2].The rapid changes in the sea level of the Caspian Sea have significant impacts on the coastal lagoons located in the southeastern part of the sea [30]. This research confirms that the amount of coastline variability in the studied area is very different, and the physical vulnerability of Gomishan coastal Lagoon depends on the geometric structure of its beach. The northern region of Gomishan has experienced high levels of drought and coastline displacement, while the central and southern parts have been less sensitive to changes in water level.The rapid displacement of coastlines in the northern part of Gomishan has caused the disappearance of suitable conditions for the entry of Caspian Sea water into the Lagoon, resulting in its complete drying since 1995. Field observations show that the decrease in the water level of the Caspian Sea has caused the formation of clay flats (Figure 6) and

Figure 6. Landform formation of mud flats on the dry bed of Gomishan lagoon and the development of mud cracks on them

Figure 7. Landform change of mud flats to salt marsh with the growth of Salicornia plant on the mud bed left over from Gomishan Lagoon

Figure 8. Change of the sedimentary environment of mud flats to sand tongue on the edge of the Caspian Sea coastline in the western part of Gomishan Lagoon

Figure 9. Illustrate the plotted points, salt flats, and dried-up environments.

salt marsh landforms (Figure 7). The Salicornia plants gradually cover the bed of the mud flats, leading to a change in the landform from mud flats to salt marsh. With the extensive growth of plants adapted to the dry and salty environment, the area has become suitable for livestock grazing, which the natives of the region use effectively. Coastal sediments along the east-to-west direction change from very fine-grained facies of clayey silt belonging to mud flats to coastal sands, and the border between them is clearly defined (Figure 7). The rapid rate of shoreline displacement in the northern part of Gomishan Lagoon leads to a significant reduction in water column depth in communication channels, preventing the proper exchange of water between the Caspian Sea and Gomishan Lagoon. This causes many environmental problems in the southeastern region of the Caspian Sea.Based on a comparison of shoreline displacement between 1995 and 2019, the study area can be classified into three groups. The first group is characterized by the highest degree of shoreline displacement and encompasses the coastal region in the northern portion of the Gomishan Lagoon, within the timeframe of the research conducted (1995-2019), alterations to the shoreline in this area ranged from 4051.9 to 7781 meters. The second classification pertains to the coastal area situated in the central portion of Gomishan, where the degree of shoreline displacement from 1995 to 2019 was observed to be between 3782 and 6160.5 meters. Finally, the third group includes the shoreline in the southern portion of Gomishan up to Bandar Turkman with a shoreline change equivalent to that of 2205 meters during the study period.However, it should be noted that the only exception observed in the studied area pertains to the displacement of the Gorgan River mouth coastline, which shows a retreat of (-1072) meters towards the coast during the timeframe of the study (Figure 10). Furthermore, at the estuary of Gorganrud River, we observe erosion and sedimentation resulting from the collision of river flow with sea currents. Figure 10 and Table 1 illustrate the amounts of coastal erosion and sedimentation at the mouth of Gorganrud River.

Table 1. The area of erosion and sedimentation in the estuary of Gorganrood River between 1995 and 2019

Characteristic	Value
Sedimentation	37.4 [*ha*]
Erosion	25.1 [*ha*]

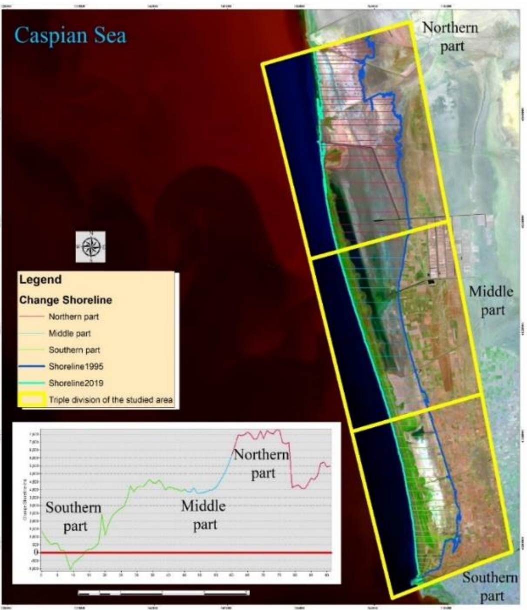

Figure 10. shoreline displacement measurement in the southern, central, and northern regions.

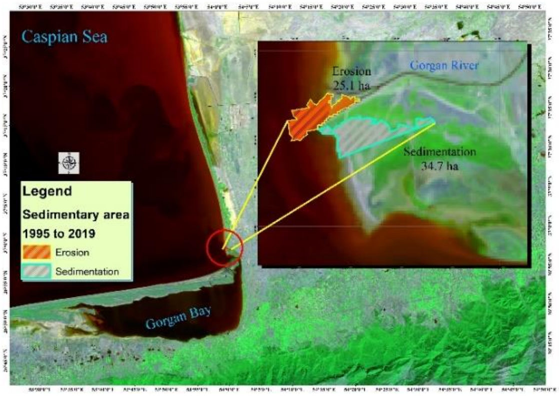

Figure 11. Spatial location of erosion and sedimentation at the mouth of Gorganrud River from 1995 to 2019

5. Conclusions

The study of the displacement of coastlines is conducted to determine the physical vulnerability of sea coasts and their catchments. The different responses of coastlines to sea level fluctuations are good natural indicators for evaluating the variability of habitats and the shape of physical parameters of coastal areas. The high level of sedimentation in the communication channel between Gorgan Bay and the Caspian Sea has provided the conditions for changing the topography of the bed and the drying process [23]. The results of this research indicate that the different coastal areas of Gomishan Lagoon have shown different morphological behaviors under the influence of the Caspian Sea water level decrease, and the intensity of the variability of the coastlines was a function of the geometric structure of the beach and the rate of Caspian Sea water level decrease. The drying up of Gomishan Lagoon caused the formation of coastal landforms such as mud flats and salt marshes in a large area of the region. The northern part of the Gomishan Lagoon experienced the highest degree of shoreline displacement during the period of 1995-2019. As a result, the Lagoon and coastal marshes have completely dried up, resulting in a shift from aquatic to dry ecosystems. The results of this research are used for comprehensive conservation management programs aimed at restoring and improving the ecological conditions of Gomishan Lagoon. For the comprehensive management of the studied area's coastlines, it is necessary to focus on areas with severe physical vulnerability resulting from the decrease in the water level of the Caspian Sea. Continuous control of the rate of quantitative and qualitative changes in the coastal habitats affected by the fluctuations of the water level of the Caspian Sea can reduce environmental challenges in existing coastal Lagoons. The effectiveness of remote sensing techniques, such as the NDWI index, for coastal studies has been confirmed, particularly regarding the extraction of coastlines for studying morphological changes. These techniques have proven to be highly effective in analyzing and monitoring coastal regions, providing valuable insights into the changes that occur over time.

6. References

[1] Ataei ,H.S., Khakpour, A. M., Adjami, M. and Neshaei, S. A., (2018), *Investigation of Caspian Sea Level Fluctuations Based on ECMWF Satellite Imaging Models and Rivers Discharge*, International Journal Of Coastal, Offshore And Environmental Engineering, 3(2), 21-30.

[2] Jeihouni, M., Kakroodi, A. A., and Hamzeh, S., (2019). *Monitoring shallow coastal environment using Landsat/altimetry data under rapid sea-level change*, Estuarine, Coastal and Shelf Science, 224, 260-271.

[3] Khoshravan, H., Naqinezhad, A., Alinejad-Tabrizi, T. and Yanina, T., (2019), *Gorgan Bay environmental consequences due to the Caspian Sea rapid water level change, Caspian J. Environ*. Sci. Vol.17, No. 3, pp. 213~226.Doi: 10.22124/CJES.2019.3664.

[4] Bagherzadeh Karimi, M., Mammedov, R. and Fathi Saghezchi, F. (2011). *Stakeholder Role Analysis for Integrated Management in Protected Areas* (Case Study: Urmia Lake, Iran). Ecopersia, (2), 101-110.

[5] Kakroodi,A.A.,Kroonenberg, S.B., Hoogendoorn, R. M.,Mohammd Khani, H., Yamani, M., Ghassemi, M. R. and Lahijani, H. A. K., (2012), *Rapid Holocene sea level changes along the Iranian Caspian coast*. Quaternary International, 263: 93-103, https://doi.org/10.1016/j.quaint.2011.12.021

[6] Ports and Maritime Organization report, (2016), *Caspian Sea Level Changes, Ministry of Roads &Urban development of I.R.* Iran.http://www.pmo.ir/en/home.

[7] Caspian Sea National Research Center. (2020).

[8] Shayan, S., Yamani, M., Kakroudi, A., Amunia, H., (1399), *Estimation of shoreline changes in the Caspian delta basin using digital coastline analysis system* (deltas: Haraz, Babolrood and Talar), Quantitative Geomorphological Research, Year 8, No. 4, pp. 34-46.

[9] Hapke, C. J., Kratzmann, M. G., and Himmelstoss, E. A., (2013*). Geomorphic and humaninfluence on large-scale coastal change*, Geomorphology, 199, 160–170.

[10] Saunders, M., Leon, J., Phinn, S. R., Callaghan, D., O'Brien, K. R., Roelfsema, C. M., Lovelock, C. E., Lyons, M. and Mumby, P. J., (2013), *Coastal retreat and improved water quality mitigate losses of seagrass from sea level rise*, Global Change Biology, 19, 2569–2583.

[11] Khoshravan, H., Naqinezhad, A., Alinejad-Tabrizi, T., and Yanina, T.,(2020), *Effects of the Caspian Sea water level change on Boujagh National Park, southwest the Caspian Sea*, Caspian J. Environ. Sci,Article in press, Doi: 10.22124/CJES.2020.4313.

[12] Misra, A. and Balaji, R., (2015) , *A study on the shoreline changes and Land-use/ land-cover along* the South Gujarat coastline , Procedia Engineering, Vol. 116, Pages 381-389, Doi:10.1016/j.proeng.2015.08.311

[13] Khoshravan, H. and Naqinejad, A.,(2018), *Understanding the Problems of Inland Waters: Case Study for the Caspian Basin (UPCB)* , International conference of Environmental consequence of Caspian rapid sea level changing in Gorgan Bay, 12-14 May ,Baku, Azerbaijan,pp: 314- 317

[14] Khoshravan, H. and Vafai, B.,(2016), *Caspian Sea level fluctuations (past, recent and future).* Proceeding of 18th International Marine Industries Conference, Kish Island, Persian Gulf, Iran, pp: 71-79 (In Persian).

[15] Bashari, L.,(2014), *Hydro geochemical study on Gorgan Bay.* Journal of Oceanograph*y*, 20: 31-42 (In Persian).

[16] Lahijani, H., Haeri Ardakani, O., Sharifi, A.and Naderi Beni, A.,(2010), *Sedimentological and geochemical characteristics of Gorgan Bay sediments,* Journal of Oceanography, 1: 45- 55 (In Persian).

[17] Konlechner, T., Kennedy, D. and M'Grady, J., (2020), *Mapping spatial variability in shoreline change hotspots from satellite data*; *a case study in southeast Australia*, Estuarine, Coastal and Shelf Science, Volume 246, 107018.

[18] Khoshravan, H.,(2022) , The evaluating coastal zone Physical vulnerability, Sefidrood River Delta, The Journal of Oceanography, Vol.13 (51) ,91-106. 10.52547/joc.13.51.9

[19] Boak, E. H., and Turner, I. L. (2005). *Shoreline definition and detection: A review*. Journal of coastal research, 21(4), 688-703.

[20] Mills, J. P., Buckley, S. J., Mitchell, H. L., Clarke, P. J., and Edwards, S. J. (2005). *A geomatics data integration technique for coastal change monitoring. Earth Surface Processes and Landforms:* The Journal of the British Geomorphological Research Group, 30(6), 651-664.

[21] Marfai, M. A., Almohammad, H., Dey, S., Susanto, B., and King, L. (2008). *Coastal dynamic and shoreline mapping: multi-sources spatial data analysis in Semarang Indonesia.* Environmental monitoring and assessment, 142, 297-308.

[22] *Convention on Lagoons of international importance especially as waterfowl habitat*, 1975, Ramsar, Iran. 6 p.

[23] Gharibreza, M., Nasrollahi, A., Afshar, A.and Amini, A, 2018, *Evolutionary trend of the Gorgan Bay (southeastern Caspian Sea) during and post the last Caspian Sea level rise, CATENA* , Volume 166, July 2018, Pages 339-348

[24] Wu, J., Wang, X., Zhong, B., Yang, A., Jue, K., Wu, J., ... and Liu, Q. (2020), *Ecological environment assessment for Greater Mekong Subregion based on Pressure-State-Response framework by remote sensing.* Ecological Indicators, 117, 106521. https://doi.org/10.1016/j.ecolind.2020.106521

[25] de Araujo Barbosa, C. C., Atkinson, P. M., and Dearing, J. A., (2015), *Remote sensing of ecosystem services: A systematic review.* Ecological Indicators, 52, 430-443.

[26] Kennedy, R. E., Andréfouët, S., Cohen, W. B., Gómez, C., Griffiths, P., Hais, M., ... and Zhu, Z., (2014), *Bringing an ecological view of change to Landsat‐based remote sensing.* Frontiers in Ecology and the Environment, 12(6), 339-346.

[27] Reza, M. I. H., and Abdullah, S. A., (2011), *Regional Index of Ecological Integrity: A need for sustainable management of natural resources.* Ecological indicators, 11(2), 220-229.

[28] Domazetovic, F., Siljeg, A., Maric, I., Faricic, J., Vassilakis, E. and Panda, L., (2021), *Automated coastline extraction using the very high resolution worldview (WV) satellite Imagery and developed coastline extraction tool (CET).* Applied Sciences, 11(20), 9482.

[29] Alcaras, E., Errico, A., Falchi, U., Parente, C. and Vallario, A., (2020, *Coastline extraction from optical satellite Imagery and accuracy evaluation. In R3 in Geomatics: Research, Results and Review*: First International Workshop in memory of Prof. Raffaele Santamaria on R3 in Geomatics: Research, Results and Review, R3GEO 2019, Naples, Italy, October 10–11, 2019, Revised Selected Papers 1 (pp. 336-349). Springer International Publishing.

[30] Qureshi, S., Alavipanah, S. K., Konyushkova, M., Mijani, N., Fathololomi, S., Firozjaei, M. K., ... and Kakroodi, A. A., (2020), *A remotely sensed assessment of surface ecological change over the Gomishan Wetland*, Iran. Remote Sensing, 12(18), 2989.

[31] Khoshravan, H., Karimi, P., Alemi Safaval, P., & Poursafari Yekrang, P., (2022), *Comparison of the intensity of coastline changes and erosion of the main ports on the Caspian Sea coast.* Iranian Journal of Remote Sensing & GIS, doi: 10.52547/gisj.2022.222252.1031

[32] Ghaderi, D. and Rahbani, M, (2020), *Shoreline change analysis along the coast of Bandar Abbas city, Iran using remote sensing Images.* International Journal of Coastal and Offshore Engineering, 4(2), 51-64.

[33]Mahmoodi,K., Saybani,M.and Moradi ,A.,(2015),*Provide a New Computational Module for Digital Shoreline Analysis System to Detect Uncertain Data in the Shoreline Change Data,* Journal Of Marine Engineering, V. 11 , issue 21

[34] Kshetri, T., (2018), Ndvi, ndbi & ndwi calculation using Landsat 7, 8. GeoWorld, 2, 32-34.

[35] Xu, H., (2007), *Extraction of urban built-up land features from Landsat Imagery using a thematic oriented index combination technique*. Photogrammetric Engineering & Remote Sensing, 73(12), 1381-1391.

[36] McFeeters, S. K., (1996), *The use of the Normalized Difference Water Index (NDWI) in the delineation of open water features*. International journal of remote sensing, 17(7), 1425-1432.

[37] Farahani,H., Ahmadi,H.and Bahrami,F., (2022), *Investigating,the coastline changes of the southern Caspian Sea using satellite Images processing and GIS techniques,*Journal of African Earth Sciences,Volume190, DOI:https://doi.org/10.1016/j.jafrearsci.2021.104402

[38] Kroonenberg, SB., Badyukova, EN., Storms, JEA., Ignatov, EI. and Kasimov, NS.,(2000), *A full sea level cycle in 65 years: barrier dynamics along Caspian shores*. Sedimentary Geology, 134: 257-274.

[39] Sharbati, S. and Ghanghermeh, A.,(2015), *The forecasting of impacts of the Caspian Sea level decreasing on Gorgan Bay*, The Journal of Science and Technology of Environment, 4: 33-45 (In Persian).

INTERNATIONAL JOURNAL OF
COASTAL, OFFSHORE & ENVIRONMENTAL ENGINEERING
IJCOE Vol.8/No. 2/Spring 2023 (56-64)

Available online at: www. Ijcoe.org

Investigation on the seasonal transformation of Tiab estuary's shoreline using RS and GIS techniques

Maryam Rahbani [1,2], Danial Ghaderi [1,2*], Rahimeh Shamsaie [1], Zarafshan Salari [1], Ali Permas [3]

[1] Faculty of Marine Science and Technology, University of Hormozgan, Bandar Abbas, Iran
[2] Center Providing Consultation and Simulation Services for Coastal And Marine Environments, Bandar Abbas, Iran
[3]Hormozgan Province Ports & Maritime Authority, Shahid Rajaee Port Complex, Bandar Abbas, Iran
Corresponding Author: danialghaderi1@gmail.com

ARTICLE INFO

Article History:
Received: 04 May. 2023
Accepted: 28 May. 2023

Keywords:
Tiab Estuary
Strait of Hormuz
Shoreline Transformation
Sentinel-2
DSAS

ABSTRACT

Estuaries are transition zones between the sea and land, and are constantly affected by tides. These areas are biologically important and sensitive. Tiab estuary, 7 km from away from the coast of Strait of Hormuz, is covered with mangroves and is also used for navigation by small commercial boats. This estuary is facing sedimentation issues nowadays which troubled navigation of vessels. Since the local wind conditions of the area is different seasonally, the influence of this difference on the transformation of the shoreline is considered for the years 2019 and 2020. The wind direction in the area is mainly SSW during summer, while is totally diverse during winter. Sentinel-2 satellite images have been used with similar water-level conditions. Normalized Difference Water Index and K-means algorithm are used for shoreline detection. The results show that the area of the estuary is more than 10 hectares smaller in summertime than in wintertime. The correlation coefficient of the seasonal transformation of the shoreline in 2019 and 2020 is 0.84, which shows that the seasonal transformation was similar in the two years. Shoreline transformation was at most along the curvatures of the river, whether in upstream or downstream. It was however varied between 45 and 200 m. Some dissimilarity in shoreline transformation was detected between the two years of study, specifically in upstream of the river, which is suggested to be due to human activities. It is believed that those parts of the estuary with high transformation are subject to permanent transformation in long term.

1. Introduction

Estuaries are the transitional zones between the sea and the rivers, which are mostly protected from wave affects, but still are constantly affected by the tide. These areas are biologically important and sensitive. Besides, anthropogenic factors can cause a wide range of changes in them (French, 2002). Various factors can change the processes of erosion and accretion in estuaries among them turbulence, variation of tidal cycles, the inflow of catchment area, local and swell waves, and climate change, (Schoellhamer, 2002). Erosion and accretion are constantly in progress in these areas own to the active hydrodynamic processes. Thus, minimal human (or natural) intervention, creates significant change in estuary zone (Ghaderi and Rahbani, 2021). Tiab estuary, located in Minab city, south of Iran, is one of the few navigable estuaries in this country. Tiab estuary faces sedimentation issue recently, in a way that emergency running aground of small fishing boats reportedly occurred. In this study, an attempt has been made to evaluate the short-term transformation of Tiab estuary's shoreline using RS and GIS techniques. To achieve this goal, the transform of the river shoreline in this estuary has been investigated during two consecutive years. The investigation is carried out for hot (summer) and cold (winter) seasons, to identify possible seasonal affect in shoreline transformation. Ghaderi and Rahbani, (2021), using field measurement, ANN and RS, investigated the amount of suspended sediments along the Tiab estuary. They claimed that the highest amount of suspended sediment can be found in the meanders of the estuary. Ghaderi and Rahbani, (2020a), using Landsat and Sentinel-2 satellite images, examined the shoreline of Bandar Abbas city. They used Normalized Difference Water Index (NDWI) band ratio to identify water and land features, and Digital Shoreline Analysis System (DSAS) tool to calculate the amount of changes. They claimed the average shoreline change rate of the Bandar Abbas urban area is +2.35 m/year, and about 53% of the shoreline faces low accretion (0.5 to 10.5 m/year), with only 4% of high accretion (20.5 to 31.5 m/year). Dereli and Tercan, (2020), estimated the shoreline change of Salda Lake, Turkey, using DSAS tool and Modified Normalized Difference Water Index (MNDWI). They indicated that historical satellite images along with statistical parameters can be used to analyze shoreline change. Muskananfola et al., (2020), conducted a study to analyze shoreline change in Sayung Beach on the northern coast of Indonesia, for a period of 24 years (from 1994 to 2018), using Landsat 5, 7 and Sentinel-2. The statistical analysis of their study was done by DSAS tool. Considering literature reviews and the condition of our study area, we decided to employ Sentinel-2 satellite images, NDWI band ratio, and DSAS tool to calculate the seasonal river of Tiab Estuary's shoreline transformation.

Study area

Tiab estuary is located 30 km south of Minab city and 7 km away from the coast of Strait of Hormuz, between latitudes 27.083693° to 27.116510° N and longitudes 56.816082° to 56.874818° E (Fig. 1) (Ghaderi and Rahbani, 2021). This estuary area is considered one of the most important estuaries in Iran which is covered with mangrove forest and is one of the few navigable estuaries in this country (Farahani et al., 2006; GHANBARI and MALEK, 2007). The main river of the estuary started from the northeast of Tiab village and enters the Persian Gulf with several branches (Fig. 1C). According to Mao et al., (2004) tidal activity is the main cause of disturbance and turbulence in estuary. The tide in the area is a mixed semidiurnal and is categorized as microtidal with a level of 1 to 2 m tidal range (Ershadi et al., 2013; Fayyaz et al., 2019; Ghaderi and Rahbani, 2021). This estuary has been recently faced numerous sedimentation problems, which has influenced the navigation in the inlet of the estuary and some branches significantly (Ghaderi and Rahbani, 2021). According to Ghaderi and Rahbani (2021) Tiab estuary is mainly influenced by tidal flood, as a result of which suspended sediments enter the estuary with the food tidal current and does not return to the sea due to the decrease in the ebb flow. According to them this issue is the main reason for the high volume of sedimentation in this estuary.

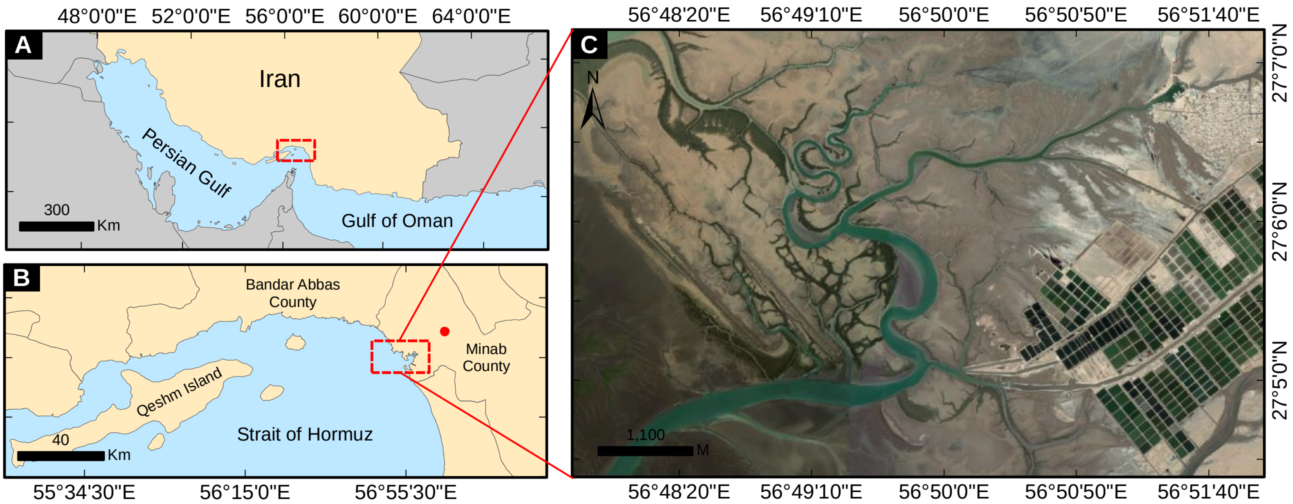

Figure 1. The study area, A and B) location of the study area. C) Aerial image of Tiab estuary (The red dot is the meteorological station of Minab county)

In addition to the tide, we suspected that the local wind conditions might influence the Tiab estuary. Even if estuary areas are mainly protected from waves and wave energy (Cowart et al., 2011), seasonal variation in wind pattern might be responsible for rare wave pattern in the area. The data from the synoptic station of Minab city (Iran Meteorological Organization) has been used to study the wind situation in the region (red point in Fig. 1 B). The statistical information of wind speed and direction for the years 2019 and 2020 is shown in Figure 2 for two seasons of summer and winter. According to the figure considerable deviation exists between the wind speed distribution of winter and summer. Such a deviation has been also stated in other studies (Kamranzad, 2018). The median wind speed of 2019 and 2020 is 1.0 and 1.6 m/s in winter and 2.0 and 2.7 m/s in summer, respectively. We therefore, decided to investigate the possible effect of this seasonal deviation for short-term transformation of the river's shoreline. We referred to Bolbasova et al., (2019) and Wu and Shi, (2022) statements that the median index provides a more accurate view of the speed difference. The kurtosis of the wind speed histogram curve is higher in the summer than in the winter, and the curve is slightly tilted towards the fourth quarter. In addition to the wind speed condition, the wind direction is an important issue for wave generation and direction. Figure 2 shows that the wind direction in summer is mainly SSW, while during the winter, the distribution of wind direction is totally diverse. The histogram curve in the summer season is close to the standard normal distribution form, but in the winter season, it is quite wide and the wind direction is slightly closer to the north. The median wind direction of the years 2019 and 2020 are 140 and 118.9 degrees for the winter and 200 and 203.2 degrees for the summer respectively.

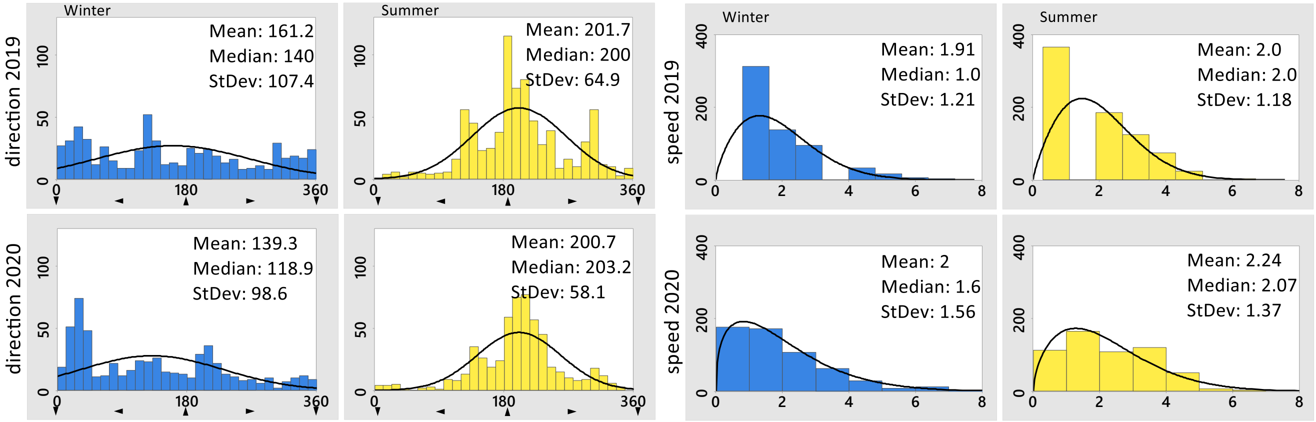

Figure 2. Histogram of wind speed and direction during 2019 and 2020 in the Tiab region for summer (yellow), and winter (blue)

2. Materials and methods

Data collection

In order to investigate the short-term transformation of shoreline of the river, the RS technique has been used, employing Sentinel-2 satellite data with temporal resolution of once every five days, and spatial resolution of 10 m. Fine spatial resolution of 10 m of the Sentinel-2 satellite is a fair reason for scientists to employ them for studying small-scale phenomena and environments (such as the Tiab estuary) (Warnasuriya et al., 2020). It has been the object in so many studies among them Ghaderi and Rahbani, (2022, 2020b, 2020a); Mitri et al., (2020); Spinosa et al., (2021); and Drusch et al., (2012). The required satellite images are obtained from the Copernicus Open Access Hub of the ESA base (ESA, 2020). Taking into account restrictions for image selection due to the cloud coverage and dissimilarity in water level, we could derive out just four images of 2019/09/01, 2020/04/12, and 2019/13/06, 2020/02/06, for winter and summer seasons respectively. It should be emphasized that the Similarity in tidal water level is very important for studying shoreline transformation, especially for small-scale study areas (Boak and Turner, 2005; Ghaderi and Rahbani, 2020a). The water level in the selected images of Tiab estuary is between 0.5 and 0.6 m (Table 1). Besides, we selected those images when the amount of atmospheric precipitation was zero.

L1C satellite images of the Sentinel-2 are geometrically and radiometrically corrected (Barsi et al., 2018), but it is necessary to make atmospheric corrections to the images. Case 2 Regional Coast Color is an efficient algorithm for atmospheric correction of coastal-sea environments (Brockmann et al., 2016); therefore, this algorithm has been used in this study following previous literatures such as Ghaderi and Rahbani, (2020a), Pereira-Sandoval et al., (2019), and Ghaderi and Rahbani, (2022).

Table 1. Information of satellite images used in the study

Date	Season	Satellite Imagery Products	Water Level (m)	Precipitation
2019/09/01	Winter	S2B_MSIL1C	0.6	0
2019/13/06	Summer	S2A_MSIL1C	0.5	0
2020/04/12	Winter	S2A_MSIL1C	0.6	0
2020/02/06	Summer	S2B_MSIL1C	0.6	0

Shoreline extraction

Considering the spectral behavior of satellite bands, the two features of water and land can be separated from each other, since each of them responds differently to different wavelengths. Body of water reflects low radiation and mainly absorbs visible to infrared wavelengths (Patel et al., 2021), but Land mainly reflects infrared wavelengths. Thus, by using two bands of Green and near-infrared in NDWI index (eq. 1), it is possible to produce the best distinction between water and land features (McFEETERS, 1996). The green (B_{GREEN}) and near-infrared bands (B_{NIR}) of the MSI sensor of the Sentinel-2 satellite are known as bands 3 and 8, respectively, and their average wavelength is 0.560 and 0.842 µm, respectively (Ghaderi and Rahbani, 2022; Patel et al., 2021).

$$NDWI = \frac{B_{GREEN} - B_{NIR}}{B_{GREEN} + B_{NIR}} \qquad (1)$$

Applying the NDWI index results to the corrected images, a raster file (Fig. 3A) can be extracted, from which a bimodal distribution (Fig. 3B) of the area can be achieved. According to the raster file, the values of -1 represent the pixels with the feature of water, and the values of +1 represent the feature of land. In order to create a border between the body of water and the land (shoreline), it is sufficient to determine an optimal numerical value separating the two environments based on the histogram diagram. Supervised and unsupervised classification methods are available for separating these two features, in which we used two algorithms of the unsupervised classification method; K-means and Expectation-Maximization (EM) for this research. Unsupervised K-means classification has the ability to distinguish both features with optimal accuracy (Ahmed and Akter, 2017; Al-doski et al., 2013; Li and Wu, 2012). The basis of the k-means clustering algorithm is to minimize the cluster performance index according to the error square and the error criterion (eq. 2) (Li and Wu, 2012; Oliver et al., 2006).

$$e^2(K) = \sum_{k=1}^{K} \sum_{i \in C_k} (x_i - c_k)^2 \qquad (2)$$

where c_k is the center of cluster C_k and K is the number of clusters (representative of prediction). The output result of the K-means algorithm is shown in Figure 3C. The result of the EM clustering algorithm is developed on the basis of artificial neural networks (Moser, 2002; Pôssa et al., 2018) (Figure 3D). One of the desirable features of the EM algorithm is its optimal performance in images with limited pixels (ESA, 2021; Ghaderi and Rahbani, 2022).

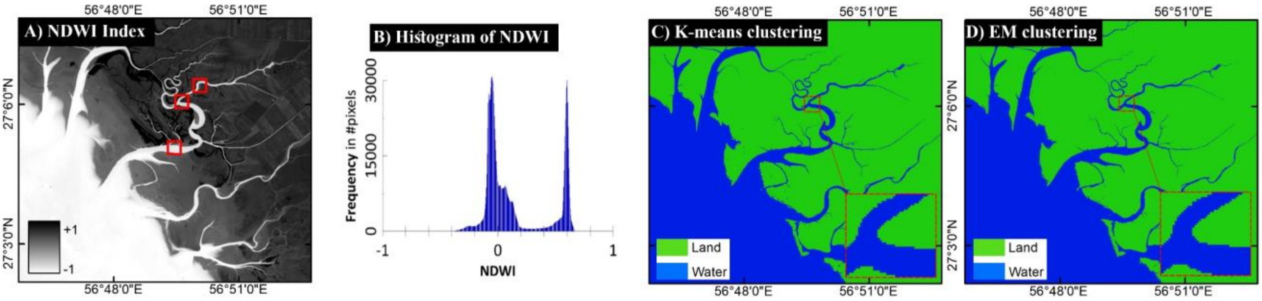

Figure 3. A) Raster file of NDWI index, B) bimodal distribution of NDWI, C and D) K-means and EM clustering of NDWI raster file, respectively (red boxes in A are used to compare the accuracy of the two algorithms)

Detecting shoreline transformation

The raster files of all four images resulting from the classification are converted into lines using ArcMap program, for statistical comparison of shorelines. The DSAS extension, developed by the United States Geological Survey, has the ability to assess the state of shoreline transformation using various statistical indicators (Thieler et al., 2009). The SCE index calculates the greatest distance between shorelines irrelevant to time, and always provides a positive number (Equation 3). This method for shoreline transformation detection has previously employed and confirmed by scientists such as Ghaderi and Rahbani, (2020b), (2020a); Muskananfola et al., (2020); Nassar et al., (2019); and Nath et al., (2022).

$$SCE = L_1 - L_2 \qquad (3)$$

where L_1 and L_2 are shorelines with the largest distance from each other. Since we employed and compared the shorelines of the two years, the obtained results only express the amount of transformation. (Himmelstoss et al., 2018; Thieler et al., 2009).

Accuracy assessment

The efficiency of unsupervised classification always depends on the accuracy level of each algorithm (Islam et al., 2021). Accuracy assessment of K-means and EM clustering algorithms has been done according to two statistical parameters Cohen's kappa coefficient (Rosenfield and Fitzpatrick-Lins, 1986) and confusion matrix. Overall accuracy is calculated using equation 5 (Congalton and Green, 2019), And Cohen’s kappa coefficient is calculated using equation 6. For the sake of accuracy estimation the accuracy of the clustering algorithm is compared with User accuracy (Rosenfield and Fitzpatrick-Lins, 1986).

$$Overall\ accuracy = \frac{\sum_{i=1}^{r} n_{ii}}{n} \qquad (5)$$

$$K_c = n \sum_{i=0}^{r} n_{ii} - \sum_{i=0}^{r} \frac{n_{icol} n_{irow}}{n^2} - \sum_{i=0}^{r} n_{icol} n_{irow} \qquad (6)$$

n_{ii} is the number of correctly classified pixels in each class; n is the total number of pixels in the confusion matrix, r is the number of rows, and n_{icol} and n_{irow} are the total column (reference data) and row (predicted classes), respectively (Congalton and Green, 2019; Liu et al., 2007). To check the total accuracy, three boxes of 500 m × 500 m were considered in three areas of Tiab estuary (Figure 3A) . Comparing User accuracy with K-means and EM algorithms, Cohen's kappa coefficient and Overall accuracy were calculated. The results of the EM algorithm show that the kappa coefficient is 0.77 and the K-means algorithm is 0.94, and the overall accuracy is 88.7% and 96.8%, respectively. Therefore, K-means classification results were considered for clustering.

3. Result

Seasonal shoreline transformation

Since we deal with the shoreline transformation of a river in an estuary in this research, hereafter we refer to the two sides of river as left side and right side facing toward the Persian Gulf. Figure 4 shows the transformation of the river shoreline between the two seasons of summer and winter with 10 m long transects. The river shoreline consists of 1500 transects, transects L-TID 1 to L-TID 718 correspond to the left side, and transects R-TID 1 to R-TID 728 correspond to the right side. The rate of seasonal shoreline transformation for the year 2019 (red graph) and 2020 (blue graph) are presented in this figure according to the SCE indexes. Based on SCE index the left side shore of the river averagely transformed 15.18 and 17.19 m during the years 2019 and 2020 respectively, with the standard deviation of 29.77 and 30.85 (minimum value for both is zero and The maximum is 206.15 and 221.99 m respectively). The results clearly indicates that seasonal shoreline transformation of the left side follows similar pattern during 2019 and 2020. The correlation coefficient (CC SCEL) of transformation in these two years is 0.90. The averaged shoreline transformations of the right side according to SCE index are 16.94 and 11.93 m in 2019 and 2020, respectively, and their standard deviations are 15.11 and 16.93 (the minimum for both is zero and the maximum is 134.85, and 138.54 m, respectively). The correlation coefficient (CC SCER) of shoreline transformation in these two years is 0.68. The results show that the averaged seasonal transformation of the left side is more than that of right side of the river. The overall correlation coefficient (CC SCE) for the shoreline transformation of the river in 2019 and 2020 is equal to 0.84.

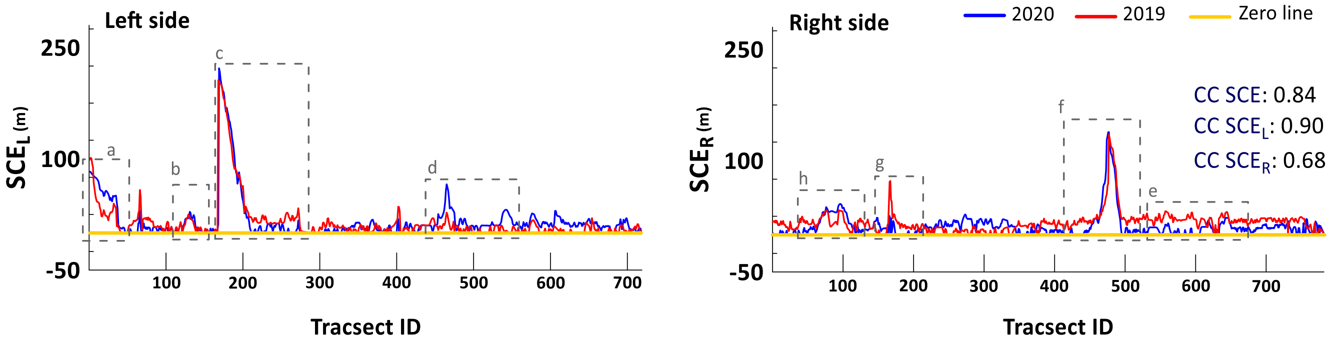

Figure 4. Rate of seasonal shoreline transformation of Tiab estuary based on SCE and NSM indexes for the year 2019 (red) and 2020 (blue).

Shoreline transformation in upstream and downstream

We used SCE index to trace the shoreline transformation of the river in upstream (farther from the Persian Gulf) (Fig. 5) and downstream (entrance of the Persian Gulf) (Fig. 6) for the two years of 2019 and 2020. Calculations revealed that coveraged area of Tiab estuary in winter time is 112.43 and 116.78 hectares, and in summer time is 93.19 and 96.53 hectares for the years 2019 and 2020, respectively. These values indicate that the area of the estuary is more than 10 hectares smaller in summer time than in winter time. As an instant we refer to sections f19 and f20 of upstream river (Fig. 5) and sections a19, a20, c19, and c20 of downstream river (Fig. 6).

At the upstream of the river f19 and f20 of Fig. 5 shoreline transformation is significant between 45 to 200 m in both years of 2019 and 2020. This area faces high erosion and accretion due to the curves of the estuary. The only deviation between the two years of this study are the small area of d20 (Fig 5), where the transformation of about 45 to 60 m is detected only for the year 2020, and e19 (Fig 5), where the transformation of approximately 20 to 45 m is detected only for the year 2019. Since this area are located upstream of the river their transformation are more likely to be influenced by human activities in these areas and are to be more studied. Most part of the river faces transformation of less than 20 m. Shoreline transformation at the inlet of the estuary (a19 and a20 in Fig. 6) is between 45 and 120 m for both the years of 2019 and 2020 (erosion type). This is the area located at a curvature and also covered by mangrove forests, which slows down the hydrodynamic conditions thus cuses sedimentation which varies seasonally. At the left side, opposite side of the river, (h19 and h20 of Fig. 6) shoreline transformation is between 20 and 45 m (erosion type). This area is located on the other side of the curvature. Thus it is expected the variation of shoreline in this part influenced by the other side of the river (a19 and a 20). This claim can be exactly applied to the areas b and g of Fig. 6, at second curvature of the downstream estuary. Area c in downstream river (Fig 6) faces the highest transformation for both 2019 and 2020, with the transformation between 45 and 200 m, which causes a large area of the estuary to be exposed in summer time. According to Ghaderi and Rahbani, (2021), current speed reduces significantly at this area and causes the accretion of suspended sediments, thus the concentration of Total Suspended Solids (TSS) in this curve is relatively high, which causes high deposition at the area.

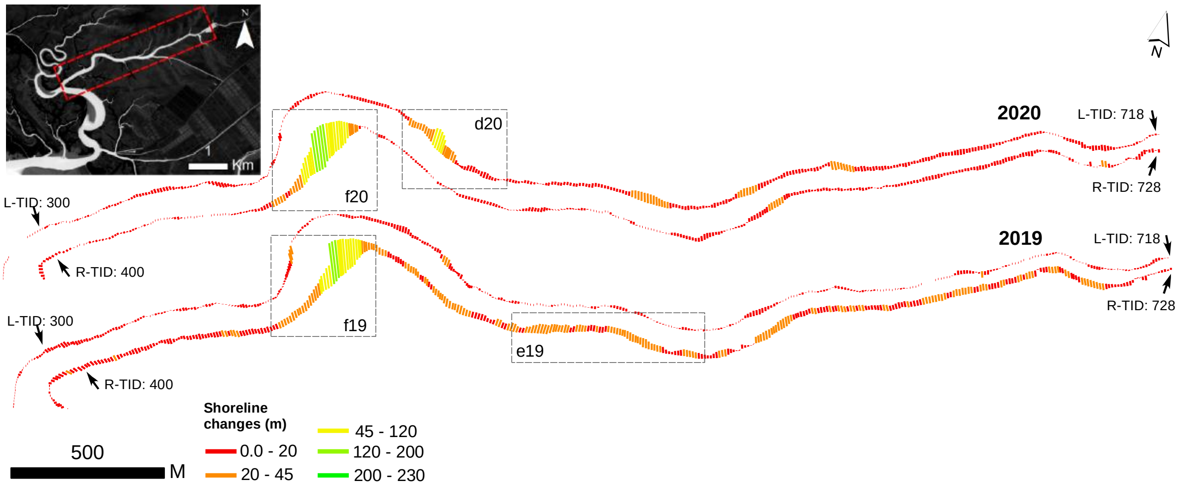

Figure 5. Seasonal shoreline transformation of the downstream river at upstream of Tiab estuary based on the SCE index for the years of 2019 and 2020

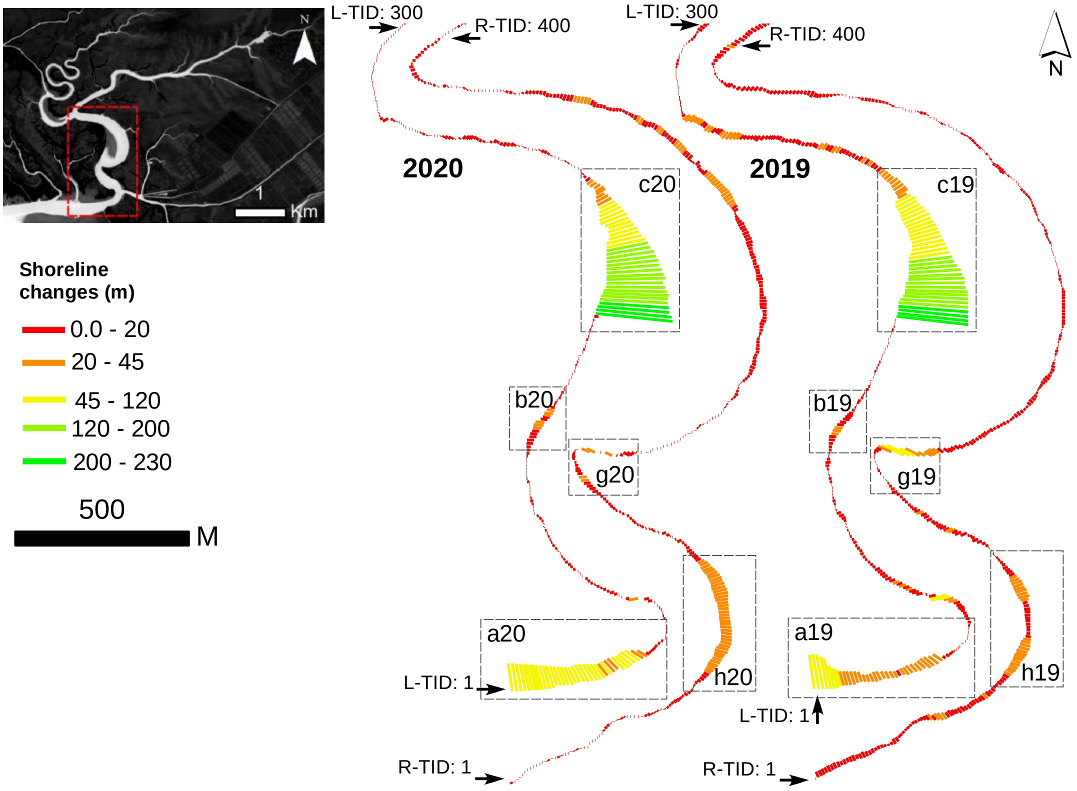

Figure 6. Seasonal shoreline transformation of the downstream river at Tiab estuary based on the SCE index for the years 2019 and 2020

4. Conclusions

The shoreline transformation of river in Tiab estuary shoreline, influenced by wind characteristics, is studied seasonally for the two years of 2019 and 2020. Considering the altering of the wind direction during summer and winter we focused on the shoreline transformation influenced by this factor. We detected similar behavior of shoreline transformation including erosion and accretion and the rate of transformation for both years. We also detected severe transformation in certain areas of the river especially downstream of the river, where the curvature exists in the channel and where the mangrove forests grow. However, the most part of the shoreline faces low transformation between

0 and 20 m. The upstream river faces the smallest transformation and some solely transformation is detected which was suspected to be due to the human activities. The highest rate of transformation in both up and downstream was detected at the curvature of the river, where the current slows down. It is expected that those part of the river with high rate of transformation, face significant changes in the long term. According to field visits, the first curvature in the downstream river (region h in this study) is eroded significantly, thus the width of the river will be increased in future. Also, in the second curvature in the downstream river (region c in this study), faces accretion in long term which makes the river relatively narrow, and this is reason for the restriction of navigation during most hours of a day which has been reported recently.

5. References

[1] Ahmed, K. R., & Akter, S. (2017). *Analysis of landcover change in southwest Bengal delta due to floods by NDVI, NDWI and K-means cluster with Landsat multi-spectral surface reflectance satellite data*. Remote Sensing Applications: Society and Environment, 8, 168–181.

[2] Al-doski, J., Mansor, S. B., Zulhaidi, H., & Shafri, M. (2013). *Image Classification in Remote Sensing* (Vol. 3, Issue 10, pp. 141–148).

[3] Barsi, J. A., Alhammoud, B., Czapla-Myers, J., Gascon, F., Haque, M. O., Kaewmanee, M., Leigh, L., & Markham, B. L. (2018). *Sentinel-2A MSI and Landsat-8 OLI radiometric cross comparison over desert sites*. In Eur. J. Remote Sens. (Vol. 51, Issue 1, pp. 822–837). https://doi.org/10.1080/22797254.2018.1507613

[4] Boak, E. H., & Turner, I. L. (2005). *Shoreline Definition and Detection: A Review*. Journal of Coastal Research, 214(4 (214)), 688–703. https://doi.org/10.2112/03-0071.1

[5] Bolbasova, L. A., Shikhovtsev, A. Y., Kopylov, E. A., Selin, A. A., Lukin, V. P., & Kovadlo, P. G. (2019). *Daytime optical turbulence and wind speed distributions at the Baikal Astrophysical Observatory*. Monthly Notices of the Royal Astronomical Society, 482(2), 2619–2626. https://doi.org/10.1093/mnras/sty2706

[6] Brockmann, C., Doerffer, R., Peters, M., Kerstin, S., Embacher, S., & Ruescas, A. (2016). *Evolution of the C2RCC neural network for Sentinel 2 and 3 for the retrieval of ocean colour products in normal and extreme optically complex waters*. ESASP, 740, 54.

[7] Congalton, R. G., & Green, K. (2019). *Assessing the Accuracy of Remotely Sensed Data*. CRC Press. https://doi.org/10.1201/9780429052729

[8] Cowart, L., Corbett, D. R., & Walsh, J. P. (2011). *Shoreline Change along Sheltered Coastlines: Insights from the Neuse River Estuary, NC, USA*. Remote Sensing, 3(7), 1516–1534. https://doi.org/10.3390/rs3071516

[9] Dereli, M. A., & Tercan, E. (2020). *Assessment of Shoreline Changes using Historical Satellite Images and Geospatial Analysis along the Lake Salda in Turkey*. Earth Sci. Inf., 13(3), 709–718. https://doi.org/10.1007/s12145-020-00460-x

[10] Drusch, M., Del Bello, U., Carlier, S., Colin, O., Fernandez, V., Gascon, F., Hoersch, B., Isola, C., Laberinti, P., Martimort, P., Meygret, A., Spoto, F., Sy, O., Marchese, F., & Bargellini, P. (2012). *Sentinel-2: ESA's Optical High-Resolution Mission for GMES Operational Services*. Remote Sensing of Environment, 120, 25–36. https://doi.org/10.1016/j.rse.2011.11.026

[11] Ershadi, S., Arasteh, M., & Tajziehchi, M. (2013). *Numerical Modeling of Flow Pattern Changes in Tidal Inlet of TIYAB Port*. Journal of Environmental and Earth Sciences, 11, 691–702.

[12] ESA. (2020). Copernicus Open Access Hub of the ESA. https://scihub.copernicus.eu/

[13] ESA. (2021). Expectation maximization (em) cluster analysis. ESA. https://www.brockmann-consult.de/beam/doc/help/clusteranalysis/EM.html

[14] Farahani, F., Farmohammadi, S. A., Golkhoo, S., & others. (2006). *Isolation of new isolate of micro algae Chlorella sp. Al-25 from Tiab estuary of Iran*.

[15] Fayyaz, M., Shafieefar, M., & Dastgheib, A. (2019). *Evaluation of the effects of sediment characteristics on long-term estuarine morphological modelling driven by waves and tides*. Applied Ocean Research, 92, 101919. https://doi.org/10.1016/j.apor.2019.101919

[16] French, P. (2002). *Coastal and estuarine management*. Routledge.

[17] Ghaderi, D., & Rahbani, M. (2020a). *Detecting shoreline change employing remote sensing images (Case study: Beris Port-east of Chabahar, Iran)*. Int. J. Coastal Offshore Eng., 3, 1–8. https://doi.org/10.29252/ijcoe.3.4.1

[18] Ghaderi, D., & Rahbani, M. (2020b). *Shoreline change analysis along the coast of Bandar Abbas city, Iran using remote sensing images*. Int. J. Coastal Offshore Eng., 4(2), 51–64. http://ijcoe.org/article-1-214-en.html

[19] Ghaderi, D., & Rahbani, M. (2021). *Tracing suspended matter in Tiab estuary applying ANN and Remote sensing*. Regional Studies in Marine Science, 44, 101788. https://doi.org/10.1016/j.rsma.2021.101788

[20] Ghaderi, D., & Rahbani, M. (2022). *Mud volcano as a feature of emergence in Caspian Sea*. Oceanologia. https://doi.org/10.1016/j.oceano.2022.03.006

[21] GHANBARI, F. M., & MALEK, M. (2007). *Permanent intertidal fish from the Persian Gulf and Gulf of Oman, Iran*.

[22] Himmelstoss, E. A., Henderson, R. E., Kratzmann, M. G., & Farris, A. S. (2018). *Digital shoreline analysis system (DSAS) version 5.0 user guide*. https://doi.org/https://doi.org/10.3133/ofr20181179

[23] Islam, M. S., Uddin, M. A., & Hossain, M. A. (2021). *Assessing the dynamics of land cover and shoreline changes of Nijhum Dwip (Island) of Bangladesh using remote sensing and GIS techniques*. Reg. Stud. Mar. Sci., 41, 101578. https://doi.org/10.1016/j.rsma.2020.101578

[24] Kamranzad, B. (2018). *Persian Gulf zone classification based on the wind and wave climate variability*. Ocean Engineering, 169, 604–635. https://doi.org/10.1016/j.oceaneng.2018.09.020

[25] Li, Y., & Wu, H. (2012). *A Clustering Method Based on K-Means Algorithm*. In Physics Procedia (Vol. 25, pp. 1104–1109). https://doi.org/10.1016/j.phpro.2012.03.206

[26] Liu, C., Frazier, P., & Kumar, L. (2007). *Comparative assessment of the measures of thematic classification accuracy*. Remote Sensing of Environment, 107(4), 606–616. https://doi.org/10.1016/j.rse.2006.10.010

[27] Mao, Q., Shi, P., Yin, K., Gan, J., & Qi, Y. (2004). *Tides and tidal currents in the Pearl River Estuary*. Continental Shelf Research, 24(16), 1797–1808. https://doi.org/10.1016/j.csr.2004.06.008

[28] McFEETERS, S. K. (1996). *The use of the Normalized Difference Water Index (NDWI) in the delineation of open water features*. Int. J. Remote Sens., 17(7), 1425–1432. https://doi.org/10.1080/01431169608948714

[29] Mitri, G., Nader, M., Abou Dagher, M., & Gebrael, K. (2020). *Investigating the performance of sentinel-2A and Landsat 8 imagery in mapping shoreline changes*. Journal of Coastal Conservation, 24(3), 1–9.

[30] Moser, G. (2002). *Unsupervised change-detection methods for remote-sensing images*. Opt. Eng., 41(12), 3288. https://doi.org/10.1117/1.1518995

[31] Muskananfola, M. R., Supriharyono, & Febrianto, S. (2020). *Spatio-temporal analysis of shoreline change along the coast of Sayung Demak, Indonesia using Digital Shoreline Analysis System*. Regional Studies in Marine Science, 34, 101060. https://doi.org/10.1016/j.rsma.2020.101060

[32] Nassar, K., Mahmod, W. E., Fath, H., Masria, A., Nadaoka, K., & Negm, A. (2019). *Shoreline change detection using DSAS technique: Case of North Sinai coast, Egypt. Mar*. Georesour. Geotechnol., 37(1), 81–95. https://doi.org/10.1080/1064119X.2018.1448912

[33] Nath, A., Koley, B., Saraswati, S., Choudhury, T., Um, J.-S., & Ray, B. C. (2022). *Geospatial analysis of short term shoreline change behavior between Subarnarekha and Rasulpur estuary, east coast of India using intelligent techniques (DSAS)*. GeoJournal. https://doi.org/10.1007/s10708-022-10683-8

[34] Oliver, A., Muñoz, X., Batlle, J., Pacheco, L., & Freixenet, J. (2006). *Improving clustering algorithms for image segmentation using contour and region information*. In 2006 IEEE International Conference on Automation, Quality and Testing, Robotics, AQTR (Vol. 2). https://doi.org/10.1109/AQTR.2006.254652

[35] Patel, K., Jain, R., Patel, A. N., & Kalubarme, M. H. (2021). *Shoreline change monitoring for coastal zone management using multi-temporal Landsat data in Mahi River estuary, Gujarat State*. Applied Geomatics, 13(3), 333–347. https://doi.org/10.1007/s12518-021-00353-8

[36] Pereira-Sandoval, M., Ruescas, A., Urrego, P., Ruiz-Verdú, A., Delegido, J., Tenjo, C., Soria-Perpinyà, X., Vicente, E., Soria, J., & Moreno, J. (2019). *Evaluation of Atmospheric Correction Algorithms over Spanish Inland Waters for Sentinel-2 Multi Spectral Imagery Data*. Remote Sens., 11(12), 1469. https://doi.org/10.3390/rs11121469

[37] Pôssa, É. M., Maillard, P., Gomes, M. F., Silva, I., & Leão, G. (2018). O*n water surface delineation in rivers using Landsat-8, Sentinel-1 and Sentinel-2 data*. In C. M. Neale & A. Maltese (Eds.), Proc. SPIE Oct. (Vol. 10783, p. 45). SPIE. https://doi.org/10.1117/12.2325725

[38] Rosenfield, G. H., & Fitzpatrick-Lins, K. (1986). *A coefficient of agreement as a measure of thematic classification accuracy. Photogramm. Eng*. Remote Sens., 52(2), 223–227.

[39] Schoellhamer, D. H. (2002). *Variability of suspended-sediment concentration at tidal to annual time scales in San Francisco Bay, USA*. Continental Shelf Research, 22(11–13), 1857–1866. https://doi.org/10.1016/S0278-4343(02)00042-0

[40] Spinosa, A., Ziemba, A., Saponieri, A., Damiani, L., & El Serafy, G. (2021). *Remote Sensing-Based Automatic Detection of Shoreline Position: A Case Study in Apulia Region*. J. Mar. Sci. Eng., 9(6), 575. https://doi.org/10.3390/jmse9060575

[41] Thieler, E. R., Himmelstoss, E. A., Zichichi, J. L., & Ergul, A. (2009). *The Digital Shoreline Analysis System (DSAS) version 4.0-an ArcGIS extension for calculating shoreline change*. https://doi.org/https://doi.org/10.3133/ofr20081278

[42] Warnasuriya, T. W. S., Kumara, M. P., Gunasekara, S. S., Gunaalan, K., & Jayathilaka, R. M. R. M. (2020). *An Improved Method to Detect Shoreline Changes in Small-Scale Beaches Using Google Earth Pro*. Marine Geodesy, 43(6), 541–572. https://doi.org/10.1080/01490419.2020.1822478

[43] Wu, J., & Shi, Y. (2022). *Changes in surface wind speed and its different grades over China during 1961–2020 based on a high-resolution dataset*. International Journal of Climatology, 42(7), 3954–3967. https://doi.org/10.1002/joc.7453